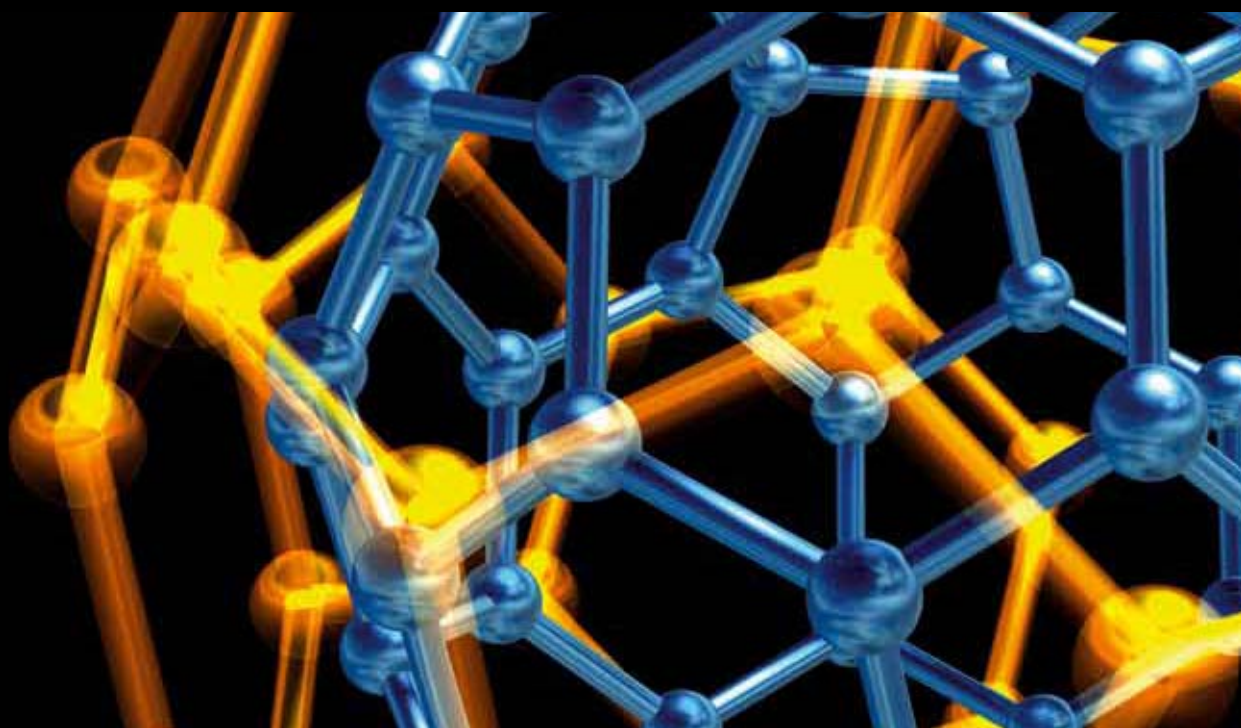


FULLERENE-RELATED NANOCARBONS AND THEIR Applications

GUEST EDITORS: JUNFENG GENG, KUN'ICHI MIYAZAWA, ZHENG HU, ILIA A. SOLOV'YOV,
AND ANGEL BERENQUER-MURCIA





Fullerene-Related Nanocarbons and Their Applications

Fullerene-Related Nanocarbons and Their Applications

Guest Editors: Junfeng Geng, Kun'ichi Miyazawa, Zheng Hu,
Ilia A. Solov'yov, and Angel Berenguer-Murcia



Copyright © 2012 Hindawi Publishing Corporation. All rights reserved.

This is a special issue published in "Journal of Nanotechnology." All articles are open access articles distributed under the Creative Commons Attribution License, which permits unrestricted use, distribution, and reproduction in any medium, provided the original work is properly cited.

Editorial Board

Simon Joseph Antony, UK
Yoshio Bando, Japan
B. Bhushan, USA
Felix A. Buot, USA
Carlos R. Cabrera, Puerto Rico
John A. Capobianco, Canada
Franco Cerrina, USA
Gan Moog Chow, Singapore
Jeffery L. Coffey, USA
Dmitriy A. Dikin, USA
Dimitris Drikakis, UK
H. D. Espinosa, USA
John S. Foord, UK
E. Goldys, Australia
Lambertus Hesselink, USA
Joseph Irudayaraj, USA
Niraj K. Jha, USA

Miguel Jose-Yacamán, USA
Valery Khabashesku, USA
Yoke Khin Yap, USA
Sakhrat Khizroev, USA
Andrei Kolmakov, USA
Charles M. Lieber, USA
Charles M. Lukehart, USA
A. Salam H. Makhlof, Germany
Constantinos Mavroidis, USA
Vincent Meunier, USA
Paolo Milani, Italy
Oded Millo, Israel
Oussama Moutanabbir, Canada
M. Grant Norton, USA
R. Lee Penn, USA
S. N. Piramanayagam, Singapore
A. M. Rao, USA

Paresh Chandra Ray, USA
Benjaram M. Reddy, India
Federico Rosei, Canada
Mehmet Sarikaya, USA
Jorge M. Seminario, USA
V. Shalaev, USA
Mahi R. Singh, Canada
Bobby G. Sumpter, USA
Xiao Wei Sun, Singapore
Weihong Tan, USA
O. K. Tan, Singapore
Thomas Thundat, USA
Boris I. Yakobson, USA
Nan Yao, USA
Chuan Jian Zhong, USA

Contents

Fullerene-Related Nanocarbons and Their Applications, Junfeng Geng, Kun'ichi Miyazawa, Zheng Hu, Iliia A. Solov'yov, and Angel Berenguer-Murcia
Volume 2012, Article ID 610408, 2 pages

PEDOT:PSS/Graphene Nanocomposite Hole-Injection Layer in Polymer Light-Emitting Diodes, Chun-Hsuan Lin, Kun-Tso Chen, Jeng-Rong Ho, J.-W. John Cheng, and Raymond Chien-Chao Tsiang
Volume 2012, Article ID 942629, 7 pages

Raman Laser Polymerization of C₆₀ Nanowhiskers, Ryohei Kato and Kun'ichi Miyazawa
Volume 2012, Article ID 101243, 6 pages

Solvation-Assisted Young's Modulus Control of Single-Crystal Fullerene C₇₀ Nanowhiskers, Tokushi Kizuka, Kun'ichi Miyazawa, and Takayuki Tokumine
Volume 2012, Article ID 583817, 5 pages

Synthesis of Carbon Nanocapsules and Nanotubes Using Fe-Doped Fullerene Nanowhiskers, Tokushi Kizuka, Kun'ichi Miyazawa, and Daisuke Matsuura
Volume 2012, Article ID 613746, 6 pages

Study of Carbon Nanotube-Substrate Interaction, Jaqueline S. Soares and Ado Jorio
Volume 2012, Article ID 512738, 10 pages

Synthesis of Nickel-Encapsulated Carbon Nanocapsules and Cup-Stacked-Type Carbon Nanotubes via Nickel-Doped Fullerene Nanowhiskers, Tokushi Kizuka, Kun'ichi Miyazawa, and Akira Akagawa
Volume 2012, Article ID 376160, 5 pages

Thickness Effect on F8T2/C₆₀ Bilayer Photovoltaic Devices, Natasha A. D. Yamamoto, Andreia G. Macedo, and Lucimara S. Roman
Volume 2012, Article ID 513457, 5 pages

Young's Modulus of Single-Crystal Fullerene C₇₀ Nanotubes, Tokushi Kizuka, Kun'ichi Miyazawa, and Takayuki Tokumine
Volume 2012, Article ID 969357, 5 pages

Editorial

Fullerene-Related Nanocarbons and Their Applications

**Junfeng Geng,^{1,2} Kun'ichi Miyazawa,³ Zheng Hu,⁴
Ilia A. Solov'yov,⁵ and Angel Berenguer-Murcia⁶**

¹*Institute for Materials Research and Innovation, University of Bolton, Bolton BL3 5AB, UK*

²*Department of Chemistry, University of Cambridge, Cambridge CB2 1EW, UK*

³*Fullerene Engineering Group, Materials Processing Unit, National Institute for Materials Science, 1-1 Namiki, Tsukuba, Ibaraki 305-0044, Japan*

⁴*Key Laboratory of Mesoscopic Chemistry, School of Chemistry and Chemical Engineering, Nanjing University, Nanjing 210093, China*

⁵*Beckman Institute for Advanced Science and Technology, University of Illinois at Urbana-Champaign, 405 N. Mathews Avenue, Urbana 61801, USA*

⁶*Materials Institute, University of Alicante, San Vicente del Raspeig, 03080 Alicante, Spain*

Correspondence should be addressed to Junfeng Geng, j.geng@bolton.ac.uk

Received 24 July 2012; Accepted 24 July 2012

Copyright © 2012 Junfeng Geng et al. This is an open access article distributed under the Creative Commons Attribution License, which permits unrestricted use, distribution, and reproduction in any medium, provided the original work is properly cited.

The discovery of fullerene (C₆₀) in 1985 spurred on the subsequent discoveries of a number of fullerene-related novel carbons at the nanometre scale. These nanocarbons are related to one another in structure, providing an interesting spectrum of variants which display an array of unique properties. From the vast amount of research that has been conducted over the last two decades, it is now apparent that these nanomaterials, notably, carbon nanotubes, carbon-based nanoparticles, graphene, fullerene and fullerene derivatives promise very distinct applications and will add great value to industries. It is thus expected that the studies on these nanocarbons and related technologies will have huge impacts on future nanotechnology and will significantly contribute to our economy and society.

The research in the field is at the crossroads between different technologies and disciplines involving materials science, chemistry, physics, engineering, and nanotechnology. Its implementation will greatly benefit new, high-tech industries and also help the transformation of traditional carbon-based industries from a resource-intensive to a knowledge-intensive base. However, major challenges exist in the area, which are mainly associated with providing answers to key questions such as how to control the nanostructures, how to produce them in commercial quantities but at relatively low costs, and how to apply them by specific requirements. In this special issue on fullerene-related nanocarbons and their applications, contributions from a broad field of research

have been received from worldwide scientists. The published works are briefly outlined as follows.

The paper by C. H. Lin et al. is a report on the effects of doping graphene in poly(3,4-ethylenedioxythiophene): poly(styrene sulfonate), PEDOT:PSS, as a PEDOT:PSS/graphene nanocomposite hole injection layer on the performance enhancement of polymer light-emitting diodes. The devices are fabricated with the nanocomposite layer, and the influence of the doping concentration on the device performance is examined by measuring the device output properties. Another paper by N. A. D. Yamamoto et al. addresses a similar topic in the field of photovoltaic devices, where the authors investigate the photovoltaic properties of a FTO(anode)/PEDOT:PSS/FT82/C₆₀/Al (cathode) bilayer device by changing the film thickness of the polymer FT82 at the heterojunction with fullerene C₆₀. Here, FTO and FT82 denote fluorine tin oxide and poly(9,9-dioctylfluorene-*alt*-bithiophene), respectively. The current-voltage characteristics of this bilayer cell follows the Mott-Gurney law of space charge limited current, suggesting that the charge transport property of the bilayer photovoltaic device is of the polymer/C₆₀ interface.

There are five papers in this special issue dealing with a research area of fullerene nanowhiskers, metal-doped fullerene nanowhiskers, and single-crystal fullerene nanotubes. Two of the papers by T. Kizuka et al. investigate, by *in situ* transmission electron microscopy and measurements

of the loading forces with an optical deflection technique, the Young's modulus of single-crystal fullerene nanotubes and nanowhiskers composed of C_{70} molecules. The other two papers by T. Kizuka et al. are on the synthesis and characterisation of Fe or Ni-doped C_{60} nanowhiskers using a liquid-liquid interfacial precipitation method. Interestingly, the nanowhiskers have been observed to be able to transform into metal-encapsulated carbon nanocapsules or carbon nanotubes by heat treatments.

The paper by R. Kato and K. Miyazawa describes a photopolymerization phenomenon of C_{60} nanowhiskers. The authors report that the nanowhiskers can be polymerised by a laser beam, associated with a Raman spectrometer, at an appropriately high laser energy dose. The polymerized material is expected to exhibit a higher mechanical strength and a better thermal stability compared with its pristine state, a topic which deserves further studies in the future. The final paper by J. S. Soares and A. Jorio addresses how carbon nanotube properties can be affected by the surrounding environment from both a theoretical and experimental perspective. The changes in parameters such as the optical transition energy and the resonance frequency of a nanotube as a consequence of its interaction with the substrate are analyzed in this work. In addition, the transitions between metal and semiconducting properties of single-walled carbon nanotubes are explained by the tube-substrate bonding effect.

*Junfeng Geng
Kun'ichi Miyazawa
Zheng Hu
Ilia A. Solov'yov
Angel Berenguer-Murcia*

Research Article

PEDOT:PSS/Graphene Nanocomposite Hole-Injection Layer in Polymer Light-Emitting Diodes

Chun-Hsuan Lin,¹ Kun-Tso Chen,¹ Jeng-Rong Ho,²
J.-W. John Cheng,¹ and Raymond Chien-Chao Tsiang³

¹Department of Mechanical Engineering, National Chung Cheng University, Chiayi 621, Taiwan

²Department of Mechanical Engineering, National Central University, Taoyuan 320, Taiwan

³Department of Chemical Engineering, National Chung Cheng University, Chiayi 621, Taiwan

Correspondence should be addressed to Jeng-Rong Ho, jrho@ncu.edu.tw

Received 15 July 2011; Accepted 4 January 2012

Academic Editor: Junfeng Geng

Copyright © 2012 Chun-Hsuan Lin et al. This is an open access article distributed under the Creative Commons Attribution License, which permits unrestricted use, distribution, and reproduction in any medium, provided the original work is properly cited.

We report on effects of doping graphene in poly(3,4-ethylenedioxythiophene): poly(styrene sulfonate), PEDOT:PSS, as a PEDOT:PSS/graphene nanocomposite hole injection layer on the performance enhancement of polymer light-emitting diodes (PLEDs). Graphene oxides were first synthesized and then mixed in the PEDOT:PSS solution with specifically various amounts. Graphenes were reduced in the PEDOT:PSS matrix through thermal reduction. PLED devices with hole-injection nanocomposite layer containing particular doping concentration were fabricated, and the influence of doping concentration on device performance was examined by systematically characterizations of various device properties. Through the graphene doping, the resistance in the hole-injection layer and the turn-on voltage could be effectively reduced that benefited the injection and transport of holes and resulted in a higher overall efficiency. The conductivity of the hole-injection layer was monotonically increased with the increase of doping concentration, performance indices from various aspects, however, did not show the same dependence because faster injected holes might alter not only the balance of holes and electrons but also their combination locations in the light-emitting layer. Results show that optimal doping concentration was the case with 0.03 wt% of graphene oxide.

1. Introduction

Polymer light emitting diodes (PLEDs), or more generally organic light emitting diodes (OLEDs), have been investigated in both commercial and academic fields because of their unique advantages such as light weight, thin structure, high resolution, and low driving voltage. The fundamental structure of a PLED consists of multiple organic thin films sandwiched between two electrodes. Thus, the device performance can be enhanced through improving characteristics of the thin films. Recently, due to their distinctive properties, the applications of nanomaterials and nanostructures to performance enhancement of PLEDs have been keeping attracting much research attention.

The literature shows, by doping nanoparticles (NPs) of TiO₂ and SiO₂ into the emitting layer MEH-PPV (poly(2-methoxy-5(2'-ethyl)hexoxy-phenylenevinylene)) in PLEDs, that the device characteristics in current density,

and luminance were obviously improved [1, 2]. This was because the doped NPs enhanced the abilities of charge injection and charge transport. In addition to their effectiveness in the light-emitting layer, the effect of TiO₂ NPs in the hole transport layer, PEDOT:PSS (poly(3,4-ethylenedioxythiophene):poly(styrene sulfonate)), was also studied. The TiO₂ NPs were again demonstrated to have ability to enhance injection of holes; consequently the turn-on voltage of the device was reduced. The modification in hole injection can also be accomplished by introducing an additional SWNTs/PVK (single carbon nanotubes/polyvinylcarbazole) nanocomposite layer between the original hole transport layer PEDOT:PSS and light-emitting layer Alq₃ [3].

In addition to playing a positive role in both the light-emitting and hole transport layers, the use of NPs and nanostructures to enhance electron injection was also widely reported. By introducing ZnO NPs between the cathode and

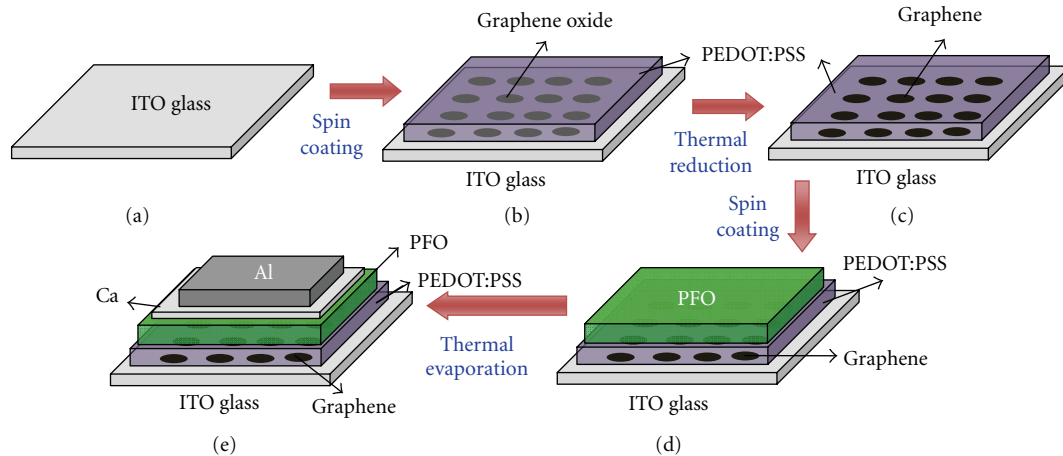


FIGURE 1: Schematics illustrating the fabrication steps of a PLED device.

the emitting layers, the device performance was enhanced because the ZnO NPs helped the injection of electrons and blocked the transport of holes to the cathode [4]. The employment of SWNTs/MEH-PPV nanocomposites as the electron transport layer showed high conductive ability in electrons, thereby enhancing the device efficiency [5]. The addition of SiO₂ NPs and SiO₂/TiO₂ NP blends between the cathode and the emitting layer as an electron injection layer was also studied and proved to be able to advance the electron injection and the internal quantum efficiency [6]. The optoelectronic efficiency of OLEDs can thus be practically improved by the measures of introducing appropriate NPs or nanostructures in and/or between organic thin films.

Indium tin oxide (ITO) is widely used as the anode in OLEDs due to its high electrical conductivity and high transparency. The performance of OLEDs is, of course, affected by the ability of injection of holes from the ITO. Thus, modification of ITO anode, such as introducing an additional hole injection layer, is an important research issue. Different hole injection layers, such as SiO₂ [7], NiO [8], carbon [9], Pt [10], PANI (polyaniline) [11], PEDOT:PSS [12, 13], and so forth, have been inserted between the ITO anode and the hole transport layer in order to decrease the injection barrier. Among them, PEDOT:PSS is widely used because of its high conductivity, high transmittance, and good film-formation properties.

By doping with suitable inorganic nanomaterials, the electrical properties of PEDOT:PSS can be improved and the resulting PEDOT:PSS nanocomposite layer in PLEDs is expected to facilitate the injection of holes. Carbon nanotubes (CNTs) exhibit high work function, high conductivity, and have low absorption coefficient. Therefore, the CNT is a good candidate of dopants for PEDOT:PSS. In the literature [14–16], the PEDOT:PSS/CNT nanocomposite was indeed shown to be an effective hole-injection layer. With the existence of CNTs, the turn-on voltage was reduced and the luminance intensity as well as the device's overall efficiency was enhanced.

Graphene, a two-dimensional structure consisting of sp²-hybridized carbon, has been depicted with excellent electrical, mechanical, thermal, chemical, and optical properties.

Therefore, its application potential in the future electronics and optoelectronics keeps attracting very much research attention. Recently, it has been reported that graphene could be doped with MEH-PPV to act as acceptor in the luminous layer [17] and inserted as a hole injection layer in a PLED [18]. Hole injection improvement through blending new synthesized solution-processable graphene oxides with PEDOT:PSS is also feasible [19, 20]. In this study, we investigate the effect of PEDOT:PSS/graphene nanocomposite hole-injection layer on the performance enhancement of PLEDs. The influence of doping concentration on device performance was systematically studied from various aspects of characteristics. Based on the results obtained, variations of properties with doping concentration were presented, and the mechanisms corresponding to these variations were discussed. The optimal doping concentration was also reported.

2. Experiments

In this study, the effect of graphene, being doped into PEDOT:PSS as a PEDOT:PSS/graphene nanocomposite layer for hole injection, on the performance enhancement of a PLED device is examined. The employed PEDOT:PSS solution was commercially available, Clevis PVP AI4083. The graphene was obtained by thermal reduction from graphene oxide (GO) which was synthesized using the Hummers method [21]. The synthesized GO powder was then dropped into the PEDOT:PSS solution to form the initial PEDOT:PSS/GO solution for the subsequent spin-coating process. According to the amount (weight) of the GO powder mixed in the PEDOT:PSS solution, five resulting PEDOT:PSS/GO solutions with different weight percentages, the weight ratio of GO powder and PEDOT:PSS/GO solution, were prepared to investigate the effect of graphene content on the device's performance. They were 0.005, 0.01, 0.03, 0.05, and 0.1 weight percentages (wt%), respectively.

The steps of fabricating a PLED device are schematically demonstrated in Figure 1. Glass with precoated indium tin oxide (ITO) thin film was used as the substrate, Figure 1(a). The PEDOT:PSS/GO solution with a particular wt% of GO was then spin coated on the ITO substrate at

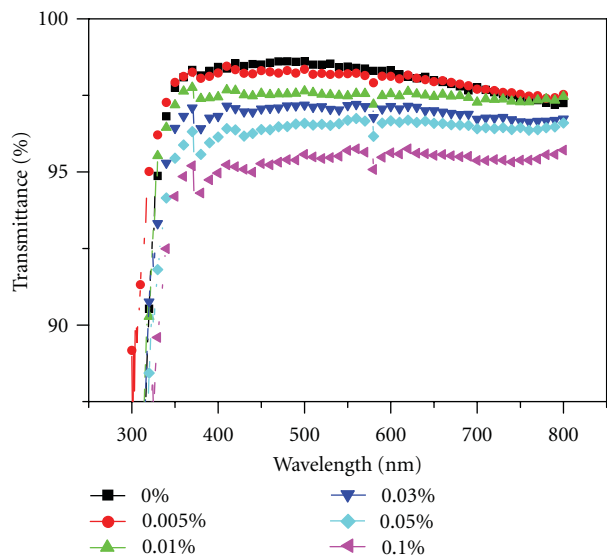


FIGURE 2: Measured curves showing transmittance as a function wavelength for PEDOT:PSS/graphene layers with various graphene concentrations.

7000 rpm for 60 s, Figure 1(b). All samples of the resulting PEDOT:PSS/graphene nanocomposite layer with specific content of graphene were obtained by immediately putting the PEDOT:PSS/GO liquid films, coated on the ITO substrates, in an oven and underwent a thermal treatment at 260°C for 1 hour in order to reduce the graphene oxide into graphene, Figure 1(c). To avoid thermal damage of PEDOT:PSS, here the treatment temperature is not high and GO might not be reduced completely [22]. The emitting layer was polyfluorene (PFO). It was prepared in chloroform with 0.7 wt% in concentration and coated upon the PEDOT:PSS/graphene nanocomposite by spin coating at 3000 rpm for 60 s and followed by baking at 70°C for 5 min on a hot plate to remove any residual solvent, Figure 1(d). Finally, the cathode metals, a bilayered structure of Ca (10 nm) and Al (100 nm), were deposited on the PFO using thermal evaporation at a vacuum pressure of 6×10^{-6} torr, Figure 1(e).

The transmittance measurement was executed using an UV/vis spectrometer (Thermo Helios Omega). The device's J - V curve (current density, ampere per unit square meter, as a function of voltage) and L - V curve (luminescence, candela per square meter, as a function of voltage) were characterized using a source meter (Keithley 2400) and a spot luminance meter (LS-100), respectively. The measurement of ionization potential (HOMO, highest occupied molecular orbital) and the electron affinity (LUMO, lowest unoccupied molecular orbital) of the PEDOT:PSS/graphene composite thin film was executed using a cyclic voltammetry (CV, CH Instruments-611C) [23, 24].

3. Results and Discussion

To understand the effect of the existence of graphene on PLED's light transmission, the transmittance, over the

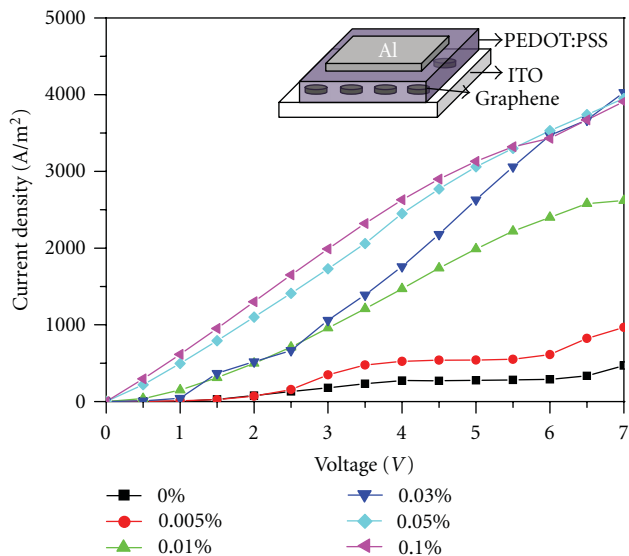


FIGURE 3: The J - V characteristics of hole-only device at various graphene concentrations. The inset shows the device configuration.

spectrum from 300 to 800 nm, of the PEDOT:PSS/graphene nanocomposite thin film was first examined. Figure 2 shows that the transmittances of all the studied nanocomposites were smaller than that of the pure PEDOT:PSS thin film (0%) and were decreased with the increase of the graphene concentration. However, even for the nanocomposite film with the highest graphene concentration (0.1%), the transmittance within the measured spectrum range was still higher than 95%. This indicates that the existence of graphene in the PEDOT:PSS did not significantly affect the luminance output of the PLEDs.

The influence of graphene on the J - V characteristics was solely examined using a hole-only device. The device configuration is schematically shown in the inset of Figure 3 and the fabrication steps for the nanocomposite layer, and the metal electrode layer followed the same procedures as those in the PLED device and were described in Section 2. The J - V characteristics for the hole-only devices with nanocomposite layers having various graphene concentrations are shown in Figure 3. For the case of 0.005%, the J - V curve was close to that for the undoped case. However, the enhancement of current density at all voltages was still observable. With the increase of the doping concentration to 0.01%, the enhancement of current density at all voltages became more obvious. This trend remained as the doping concentration was further enhanced. However, as the concentration was augmented from 0.05 to 0.10%, the degree of enhancement in current density again became less evident. These results indicate that, with the doping of graphene, the conductivity in the PEDOT:PSS thin film could be markedly improved and the more the doped concentration the higher the conductivity. However, when the doping concentration was high enough, the rate of augmentation in current density owing to the succeeding increase of doping concentration became less apparent.

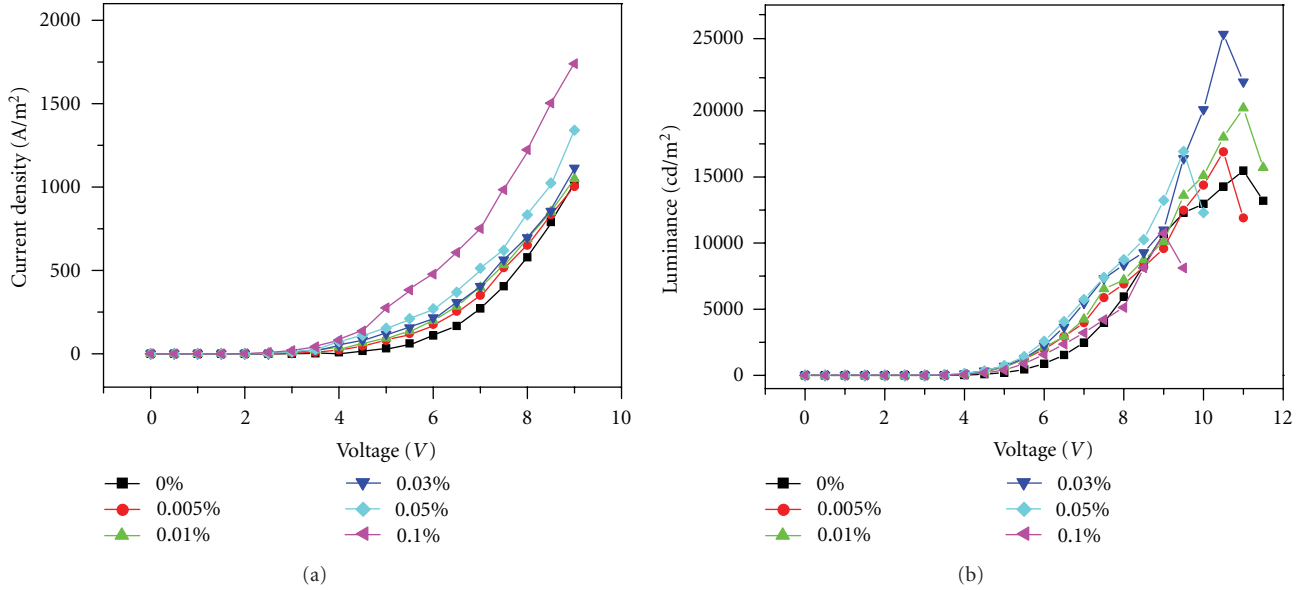


FIGURE 4: The effect of graphene concentration on the J - V curves (a) and L - V curves (b) of PLED using PEDOT:PSS/graphene nanocomposite as the hole-injection layer.

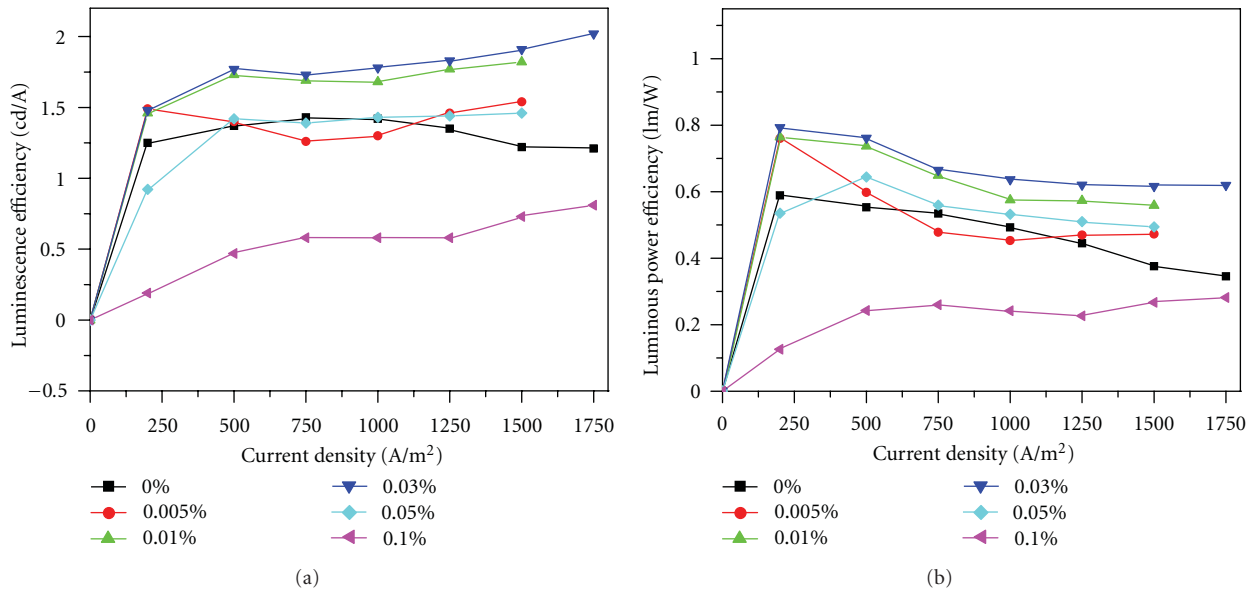


FIGURE 5: The effect of graphene concentration on luminous efficiency (a) and luminous power efficiency (b) of PLEDs using PEDOT:PSS/graphene nanocomposite as the hole-injection layer.

Figures 4(a) and 4(b) show that the characteristics of J - V and L - V of the PLED devices, respectively. In Figure 4(a), the curve for the pure PEDOT:PSS showed the lowest current density and, on the other hand, the device with the highest doping concentration of graphene, 0.1%, had the highest current density. The curves in this figure clearly exhibited the tendency that the current density increased with the increase of doping concentration. With the increase of graphene content, the resistance of the composite films was reduced that resulted in decrease of the device's bulk resistance and led to an increase in current density. Figure 4(b) shows the luminance of a PLED device was enhanced monotonically with the increase of voltage and the device broke down when the voltage was too large. The reachable maximum

luminance for the device using the PEDOT:PSS as the hole-injection layer was about 15480 cd/m² occurring at the voltage of 11 V and that could be increased to 25800 cd/m² at even a little bit lower voltage of 10.5 V for the device with doping concentration of 0.03%.

Because of different doping concentrations and unavoidable uncertainties in sample preparation and device fabrication, the reachable maximum luminance for each device would occur at different voltages. Other often-used indices for evaluating performance of a PLED device include the luminous efficiency and the luminous power efficiency. These two indices for the currently studied devices are presented in Figure 5. Figures 5(a) and 5(b), respectively, show the luminous efficiency (cd/A, candela per unit

TABLE 1: Electrical characteristics of the PLEDs with various concentrations of PEDOT:PSS/graphene composite layers.

Device characteristics	Weight percentage of graphene oxide (wt%)					
	0	0.005	0.01	0.03	0.05	0.1
V_T (V)	3.12	3	2.8	2.75	2.6	2.75
Max. luminance (cd/m^2)	15480	16900	20200	25800	16930	10730
Max. current eff. (cd/A)	1.43	1.56	1.88	2.09	1.48	0.84
Max. power eff. (lm/W)	0.58	0.76	0.76	0.79	0.64	0.24

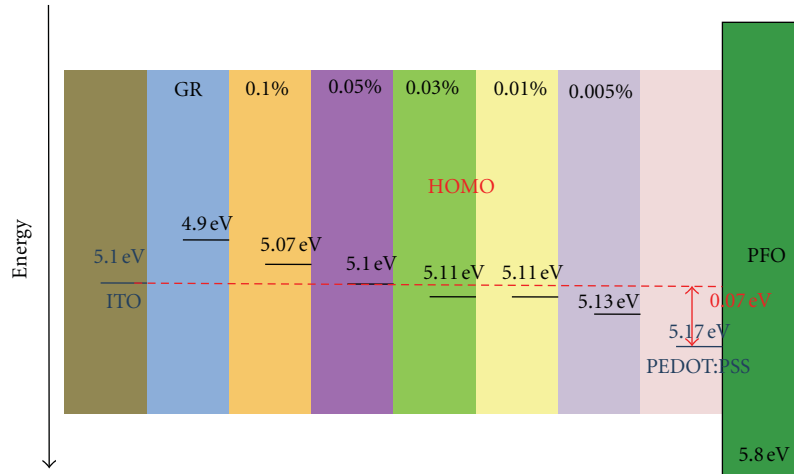


FIGURE 6: Schematic energy level diagram for the PEDOT:PSS/graphene nanocomposites with different graphene concentrations.

current) and luminous power efficiency (lm/W , luminance per unit power) as a function of current density. For the undoped device, the luminous efficiency and luminous power efficiency were 1.43 cd/A and 0.58 lm/W , respectively. With introducing graphene into the PEDOT:PSS film, both efficiencies could be improved. The results show that both efficiencies were augmented with the increase of doping concentration when the doping concentration was low. Their dependent relationship on doping concentration became, however, inverted, if the doping concentration was higher than 0.03%.

The role of the nanocomposite layer in the PLED device was to smooth the hole-injection progress. As demonstrated in the hole-only devices previously, because of the graphene doping, the conductivity of composite layer was apparently enhanced, and, the more the doping concentration, the higher the conductivity enhancement. When the doping concentration was not high, the enhancement of both efficiencies with the increase of doping concentration was attributable to the improvement of hole injection in the composite layer that led to more balanced holes and electrons combination in the emitting layer and thereby gaining higher overall efficiency. If the doping concentration kept increased, the nanocomposite layer's conductivity continued to be enhanced; more holes were injected and moved in a faster speed. The balance of hole-electron combination was altered, and, in addition, the location of carrier combination in the emitting layer was changed, toward to cathode. Thus, the efficiency was reduced. For the present study, the optimal doping concentration was around 0.03% where the luminous efficiency and luminous power efficiency were

increased to 2.09 cd/A and 0.79 lm/W , respectively, which were correspondingly 0.46 and 0.36 times of enhancement compared to the one without doping.

More complete electrical characteristics of the PLED device are listed in Table 1. It can be seen that, in addition to the reachable maximum luminance, current and power efficiencies, the turn-on voltage, and V_T (the driving voltage as the luminance at 1 cd/m^2) could be improved by the graphene doping. The V_T was 3.12 V for the undoped device, and its value was decreased with the increase of graphene concentration. It reached a lowest value of 2.6 V at a concentration of 0.05%. When the doped concentration was higher than 0.05%, the turn-on voltage was increased again. The variation in device's turn-on voltage is usually affected by the work functions of thin films [9, 25].

The work functions of ITO, PEDOT:PSS, and graphene are 5.1, 5.17, and 4.9 eV, respectively. These values and the HOMOs of composite layers are listed in the energy diagram shown in Figure 6. The energy barrier between ITO and PEDOT:PSS was 0.07 eV. The work function of graphene is 4.9 eV which is lower than those of ITO and PEDOT:PSS. Thus, with the introduction of an appropriate amount of graphene in the PEDOT:PSS, the work function of this nanocomposite layer was reduced and the energy barrier was also lowered that facilitated the injection of holes and led to the reduction of the turn-on voltage. When the concentration was over than 0.05%, the work functions of the composite films were lower than that of ITO. A Schottky barrier was formed at the contact which hindered hole injection and led to an increase of the turn-on voltage again.

4. Conclusions

In conclusion, the PEDOT:PSS/graphene nanocomposite thin film, PEDOT:PSS doped with graphenes, was fabricated and its application as a hole-injection layer in PLEDs was studied. Graphene oxides were first synthesized by Hummers' method and then mixed in the PEDOT:PSS solution at several specific amounts. The PEDOT:PSS/graphene nanocomposite with particular graphene doping concentration was obtained by thermally reducing the graphene oxides into graphenes. The effect of doping concentration on the device performance was systematically examined, and the mechanism of characteristic modifications was discussed. The doping of graphene can effectively enhance the conductivity in the hole-injection layer and reduce the turn-on voltage that made the progress of hole injection more smoothly and led to a higher overall device efficiency. Results showed, compared with the case of using undoped hole-injection layer, that the maximum luminance could be enhanced up to 1.66 times while the efficiencies of luminous and luminous power were increased 46% and 36%, respectively. Basically, the hole-injection ability was increased with the increase of doping concentration. However, if the doping concentration was too high, the device performance was reduced with the success increase of doping concentration. The optimal doping concentration was from the case using 0.03 wt% of graphene oxide.

Acknowledgment

Financial support from the National Science Foundation of Taiwan under Grant numbers NSC97-2221-E-194-058-MY3 and NSC99-2627-E-194-001 is greatly appreciated.

References

- [1] S. A. Carter, J. C. Scott, and P. J. Brock, "Enhanced luminance in polymer composite light emitting devices," *Applied Physics Letters*, vol. 71, no. 9, pp. 1145–1147, 1997.
- [2] N. N. Dinh, L. H. Chi, T. T. C. Thuy, T. Q. Trung, and V. V. Truong, "Enhancement of current-voltage characteristics of multilayer organic light emitting diodes by using nanostructured composite films," *Journal of Applied Physics*, vol. 105, no. 9, Article ID 093518, 2009.
- [3] J. Y. Kim, M. Kim, H. Kim, J. Joo, and J. H. Choi, "Electrical and optical studies of organic light emitting devices using SWCNTs-polymer nanocomposites," *Optical Materials*, vol. 21, no. 1–3, pp. 147–151, 2002.
- [4] L. Qian, Y. Zheng, K. R. Choudhury et al., "Electroluminescence from light-emitting polymer/ZnO nanoparticle heterojunctions at sub-bandgap voltages," *Nano Today*, vol. 5, no. 5, pp. 384–389, 2010.
- [5] I. Singh, D. Madhwal, A. Verma et al., "Enhanced luminance of MEH-PPV based PLEDs using single walled carbon nanotube composite as an electron transporting layer," *Journal of Luminescence*, vol. 130, no. 11, pp. 2157–2160, 2010.
- [6] B. Riedel, J. Hauss, M. Aichholz, A. Gall, U. Lemmer, and M. Gerken, "Polymer light emitting diodes containing nanoparticle clusters for improved efficiency," *Organic Electronics*, vol. 11, no. 7, pp. 1172–1175, 2010.
- [7] Z. B. Deng, X. M. Ding, S. T. Lee, and W. A. Gambling, "Enhanced brightness and efficiency in organic electroluminescent devices using SiO₂ buffer layers," *Applied Physics Letters*, vol. 74, no. 15, pp. 2227–2229, 1999.
- [8] I. M. Chan and F. C. Hong, "Improved performance of the single-layer and double-layer organic light emitting diodes by nickel oxide coated indium tin oxide anode," *Thin Solid Films*, vol. 450, no. 2, pp. 304–311, 2004.
- [9] A. Gyoutoku, S. Hara, T. Komatsu, M. Shirinashihama, H. Iwanaga, and K. Sakanoue, "An organic electroluminescent dot-matrix display using carbon underlayer," *Synthetic Metals*, vol. 91, no. 1–3, pp. 73–75, 1997.
- [10] Y. Shen, D. B. Jacobs, G. G. Malliaras, G. Koley, M. G. Spencer, and A. Ioannidis, "Modification of indium tin oxide for improved hole injection in organic light emitting diodes," *Advanced Materials*, vol. 13, no. 16, pp. 1234–1238, 2001.
- [11] Y. Yang and A. J. Heeger, "Polyaniline as a transparent electrode for polymer light-emitting diodes: lower operating voltage and higher efficiency," *Applied Physics Letters*, vol. 64, no. 10, pp. 1245–1247, 1994.
- [12] Y. Cao, G. Yu, C. Zhang, R. Menon, and A. J. Heeger, "Polymer light-emitting diodes with polyethylene dioxythiophene-polystyrene sulfonate as the transparent anode," *Synthetic Metals*, vol. 87, no. 2, pp. 171–174, 1997.
- [13] A. Elschner, F. Bruder, H. W. Heuer et al., "PEDT/PSS for efficient hole-injection in hybrid organic light-emitting diodes," *Synthetic Metals*, vol. 111–112, pp. 139–143, 2000.
- [14] H. S. Woo, R. Czerw, S. Webster, D. L. Carroll, J. W. Park, and J. H. Lee, "Organic light emitting diodes fabricated with single wall carbon nanotubes dispersed in a hole conducting buffer: the role of carbon nanotubes in a hole conducting polymer," *Synthetic Metals*, vol. 116, no. 1–3, pp. 369–372, 2001.
- [15] G. F. Wang, X. M. Tao, and R. X. Wang, "Fabrication and characterization of OLEDs using PEDOT:PSS and MWCNT nanocomposites," *Composites Science and Technology*, vol. 68, no. 14, pp. 2837–2841, 2008.
- [16] M. Shao, M. P. Garrett, X. Xu, I. N. Ivanov, S. S. Wong, and B. Hu, "Effects of single walled carbon nanotubes on the electroluminescent performance of organic light-emitting diodes," *Organic Electronics*, vol. 12, no. 6, pp. 1098–1102, 2011.
- [17] Z. Liu, D. He, Y. Wang, H. Wu, and J. Wang, "Effect of SPFG graphene dopant in MEH-PPV organic light-emitting devices," *Synthetic Metals*, vol. 160, no. 13–14, pp. 1587–1589, 2010.
- [18] J. H. Hwang, K. S. Lee, H. S. Bang et al., "Enhancement of the hole injection current in polymer light-emitting devices fabricated utilizing a graphene layer," *Journal of the Electrochemical Society*, vol. 158, no. 9, pp. J273–J275, 2011.
- [19] H. Chang, G. Wang, A. Yang et al., "A transparent, flexible, low-temperature, and solution-processible graphene composite electrode," *Advanced Functional Materials*, vol. 20, no. 17, pp. 2893–2902, 2010.
- [20] Z. Zhong, Y. Dai, D. Ma, and Z. Y. Wang, "Facile synthesis of organo-soluble surface-grafted all-single-layer graphene oxide as hole-injecting buffer material in organic light-emitting diodes," *Journal of Materials Chemistry*, vol. 21, no. 16, pp. 6040–6045, 2011.
- [21] W. S. Hummers Jr. and R. E. Offeman, "Preparation of graphitic oxide," *Journal of the American Chemical Society*, vol. 80, no. 6, p. 1339, 1958.
- [22] S. H. Huh, "Thermal reduction of graphene oxide," in *Physics and Applications of Graphene—Experiments*, S. Mikhailov, Ed., chapter 5, InTech, 2011.

- [23] R. Cervini, X.-C. Li, G. W. C. Spencer, A. B. Holmes, S. C. Moratti, and R. H. Friend, "Electrochemical and optical studies of PPV derivatives and poly(aromatic oxadiazoles)," *Synthetic Metals*, vol. 84, no. 1-3, pp. 359-360, 1997.
- [24] N. G. Connelly and W. E. Geiger, "Chemical redox agents for organometallic chemistry," *Chemical Reviews*, vol. 96, no. 2, pp. 877-910, 1996.
- [25] C. C. Oey, A. B. Djurixic, C. Y. Kwong et al., "Nanocomposite hole injection layer for organic device applications," *Thin Solid Films*, vol. 492, no. 1-2, pp. 253-258, 2005.

Research Article

Raman Laser Polymerization of C₆₀ Nanowhiskers

Ryoei Kato and Kun'ichi Miyazawa

National Institute for Materials Science, Fullerene Engineering Group, 1-1, Namiki, Ibaraki, Tsukuba 305-0044, Japan

Correspondence should be addressed to Kun'ichi Miyazawa, miyazawa.kunichi@nims.go.jp

Received 14 July 2011; Revised 25 December 2011; Accepted 4 January 2012

Academic Editor: Junfeng Geng

Copyright © 2012 R. Kato and K. Miyazawa. This is an open access article distributed under the Creative Commons Attribution License, which permits unrestricted use, distribution, and reproduction in any medium, provided the original work is properly cited.

Photopolymerization of C₆₀ nanowhiskers (C₆₀NWs) was investigated by using a Raman spectrometer in air at room temperature, since the polymerized C₆₀NWs are expected to exhibit a high mechanical strength and a thermal stability. Short C₆₀NWs with a mean length of 4.4 μm were synthesized by LLIP method (liquid-liquid interfacial precipitation method). The A_g(2) peak of C₆₀NWs shifted to the lower wavenumbers with increasing the laser beam energy dose, and an energy dose more than about 1520 J/mm² was found necessary to obtain the photopolymerized C₆₀NWs. However, excessive energy doses at high-power densities increased the sample temperature and lead to the thermal decomposition of polymerized C₆₀ molecules.

1. Introduction

C₆₀ nanowhiskers (C₆₀NWs) are the single crystal nanofibers composed of C₆₀ molecules [1] and can be synthesized by a facile method called "LLIP method" [2]. C₆₀NWs have a variety of applications and such as field-effect transistors (FETs) [3], solar cells [4], biosensors [5].

C₆₀ molecules can be polymerized by electron beam irradiation [6]. Although as-grown C₆₀NWs are composed of the C₆₀ molecules that are weakly bonded via van der Waals forces [7], the C₆₀NWs irradiated by electron beams showed the stronger thermal stability [8], the higher Young's modulus [9] than pristine van der Waals C₆₀ crystals. Hence, it is of great importance to study the polymerization of C₆₀NWs in order to improve their mechanical and thermal properties.

Laser irradiation is a promising method to obtain the polymerized C₆₀ molecules [7, 10]. We first showed the photopolymerization of C₆₀NWs by using the Raman laser beam irradiation [7]. Rao et al. showed that the peak of A_g(2) pentagonal pinch mode of C₆₀ shifts downward from 1469 cm⁻¹ to 1459 cm⁻¹ upon the photopolymerization [11], showing that the shift of A_g(2) peak is a good indicator for the polymerization of C₆₀.

Alvarez-Zauco et al. studied the polymerization of C₆₀ thin films in air by the ultraviolet (UV) laser irradiation as a function of laser energy dose (= fluence) from 10 to

50 mJ/cm² in order to optimize the photopolymerization of C₆₀ films [12]. Likewise, the laser energy dose for the photopolymerization of C₆₀NWs should be optimized. Hence, the present study aims to reveal how the polymerization of C₆₀NWs proceeds as a function of the laser beam energy dose.

2. Experimental

C₆₀NWs were synthesized by a modified liquid-liquid interfacial precipitation method. Isopropyl alcohol (IPA) was gently poured into a toluene solution saturated with C₆₀ (MTR Ltd. 99.5%) in a glass bottle to make a liquid-liquid interface, and then the solution was subjected to ultrasonication and stored in an incubator at 10°C to grow short C₆₀NWs. The synthesized C₆₀NWs were filtered and dried in vacuum at 100°C for 120 min. to remove the solvents. In the Raman spectrometry analyses, the C₆₀NWs dispersed in ethyl alcohol were mounted on a slide glass and dried in air.

A Raman spectrometer (JASCO, NRS-3100) with a green laser of 532 nm excitation wavelength was used for the polymerization and structural analysis of C₆₀NWs in air. The power of laser light illuminated onto the specimens was measured by using a silicon photodiode (S2281, Hamamatsu Photonics K.K.). The laser beam power density (*D*) and

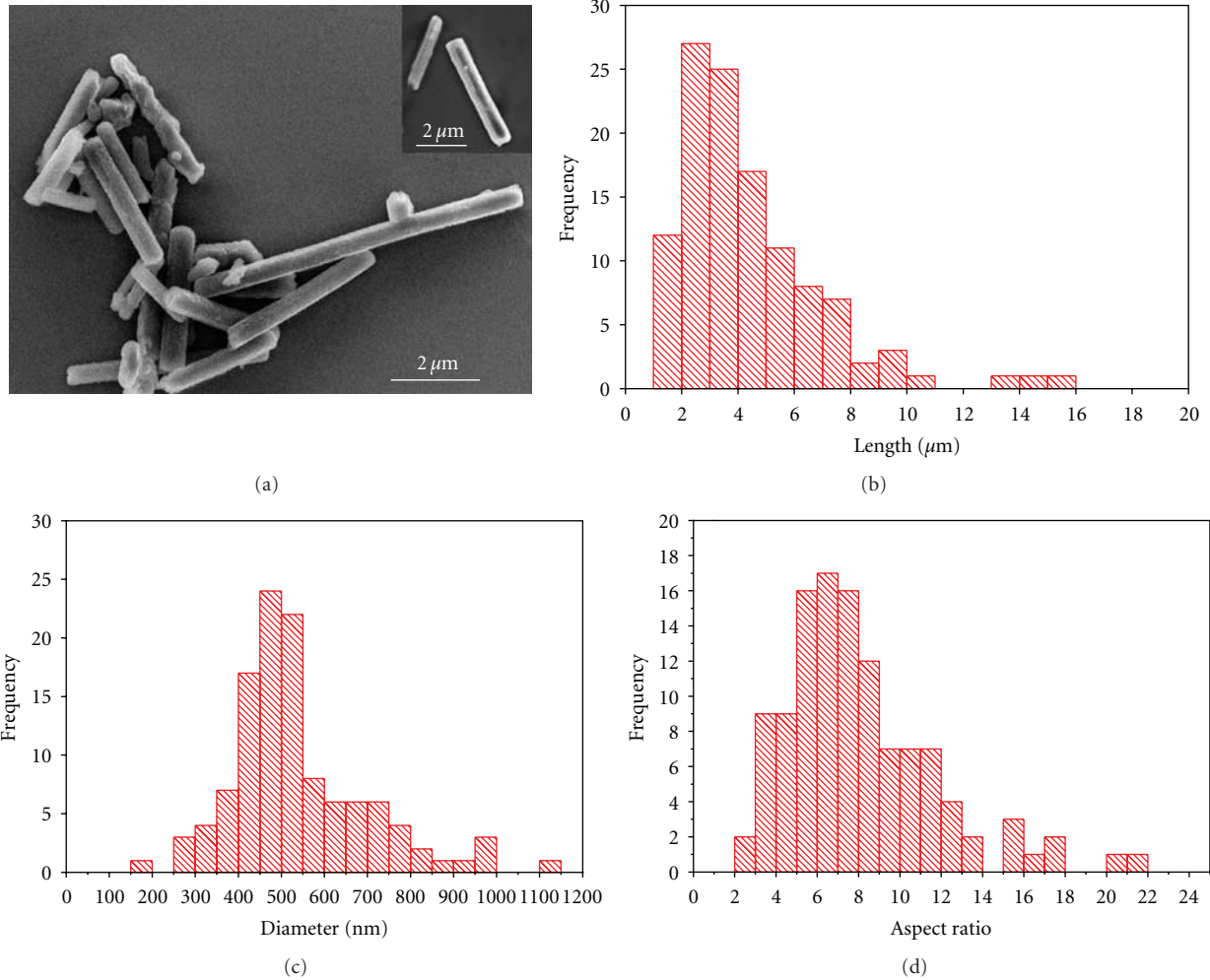


FIGURE 1: (a) SEM images, (b) length, (c) diameter, and (d) aspect ratio (length/diameter) distributions of the synthesized C₆₀NWs.

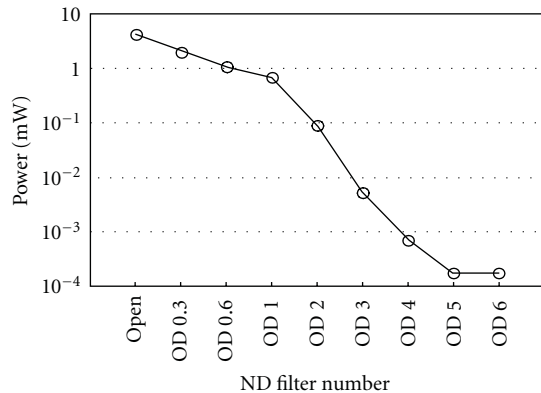


FIGURE 2: Relationship between the neutral density (ND) filter number and the laser beam power.

the energy dose of excitation laser beams in the Raman spectroscopy were controlled by changing ND (Neutral Density) filters, the defocus value of objective lens, and the

exposure time of laser beam. D is defined by the following formula in this paper,

$$D \text{ (mW/mm}^2\text{)} = \frac{\text{The power of laser beam (mW)}}{\text{the area of laser beam exposed on the sample (mm}^2\text{)}} \quad (1)$$

3. Results and Discussion

Figure 1 shows examples of scanning electron microscopy (SEM) images and the size distributions of the synthesized C₆₀NWs with a mean length of $4.4 \pm 2.7 \mu\text{m}$ and a mean diameter of $540 \pm 161 \text{ nm}$. The distribution of aspect ratios (length/diameter) is also shown. Most of the C₆₀NWs were found to possess the aspect ratios less than 15.

The power of excitation laser beam can be changed by selecting ND filters. Figure 2 shows the relationship between the ND filter number and the power of laser beam irradiated on samples. The laser beam power could be widely changed

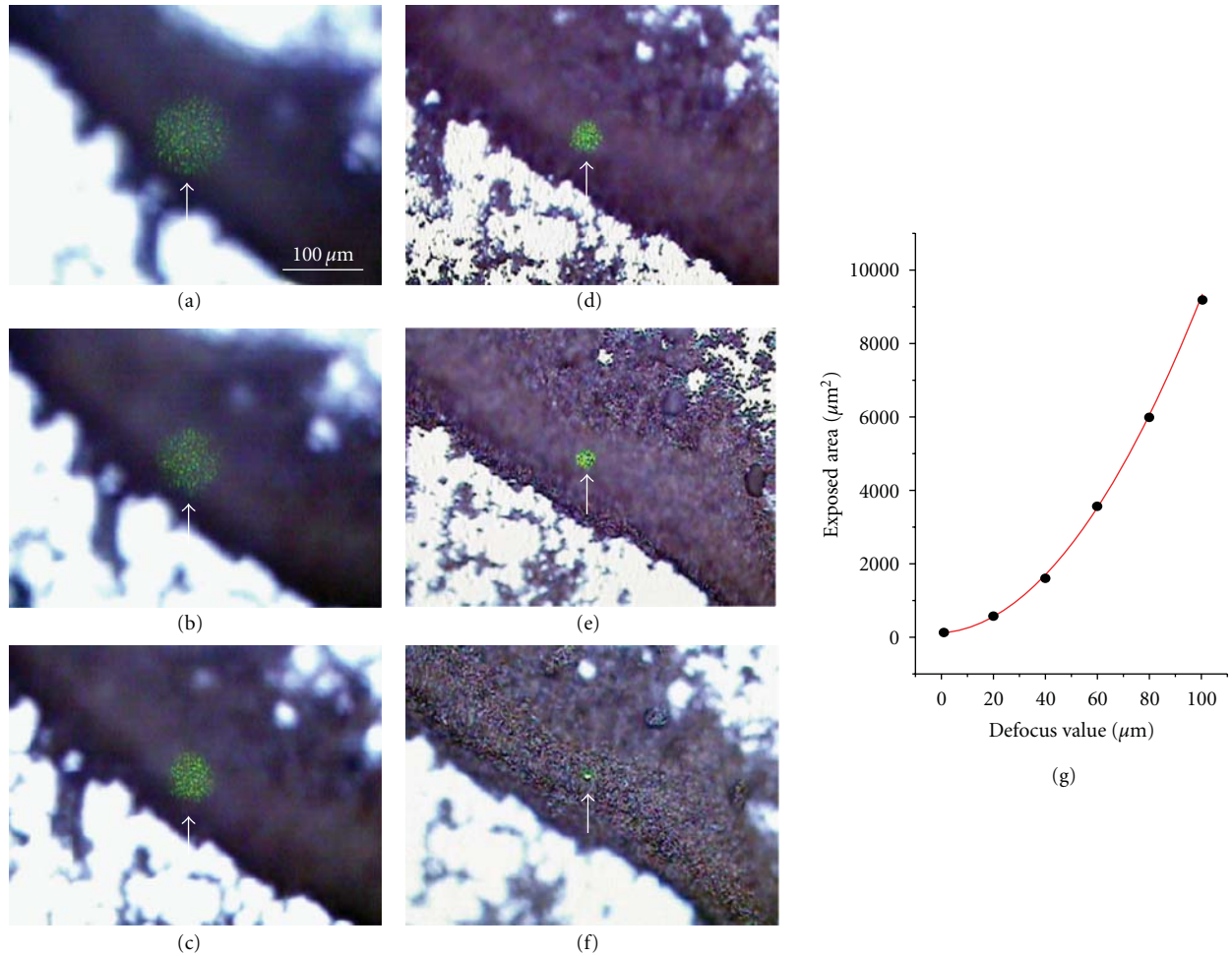


FIGURE 3: Optical microscopy images of the samples of C₆₀NWs irradiated by the excitation laser beams for the defocus values (under focus) of (a) 100, (b) 80, (c) 60, (d) 40, (e) 20, and (f) 0 μm and for the arrowed exposed areas of (a) 9270, (b) 6630, (c) 3480, (d) 1470, (e) 617, and (f) 63.8 μm², respectively. Graph (g) shows the relationship between the defocus value and the exposed area.

between OD1 and OD3. The ND filters OD1 (attenuation rate 0.1), OD2 (0.01), and OD3 (0.001) were used in the experiment, since the other filters gave too strong or too weak laser beam energies. The excitation laser beam power density could be varied from about 0.53 to 11800 mW/mm² using the above ND filters and by controlling the irradiation area of the laser beams and the defocus value from 0 to 100 μm as shown in Figure 3. The defocus value is defined as the distance from actual image plane and was set to be positive as the distance between the objective lens and the sample surface decreased. The places of C₆₀NWs exposed to the excitation laser beams can be recognized as the green circular areas marked in Figures 3(a)–3(f). The area of laser beam on the samples could be changed from 63.8 to 9270 μm² by controlling the defocus value from 0 to 100 μm.

The exposed area (y , μm²) and the defocus value (x , μm) were plotted as shown in Figure 3(g). The plotted points can be approximated by the fitted quadratic curve, $y = 0.88x^2 + 6.8x + 36$. Figure 4 summarizes the relationship among the laser beam power density, ND filter number, and the defocus value.

Figure 5 shows examples of the Raman spectra of C₆₀NWs taken by using the ND filters of OD1, OD2, and OD3 for an exposure time of about 220 s, where the spot size of laser beam on samples was 9 μm in diameter. Each power density of the excitation laser beam was (a) 11800, (b) 1660, and (c) 71.5 mW/mm², respectively. The A_g(2) peak around 1468 cm⁻¹ sifted to the lower wavenumbers with increasing the laser beam power density.

Figure 6 shows the A_g(2) peak positions of the Raman spectra of C₆₀NWs as a function of energy dose of the laser beam for each defocus value from 100 μm to 0 μm (just focus). The power density of laser beam on samples was changed by changing the defocus value and the ND filter number as shown in Figure 4. The energy dose was changed by setting the beam exposure time at 215 ± 6 s, 441 ± 10 s, 665 ± 9 s, and 899 ± 29 s for each power density. Hence, as a whole, 72 data points are plotted in Figure 6. As shown in Figure 5, the Raman shifts are found to generally decrease to the lower values with increasing the energy dose. However, the Raman shifts were observed to increase along

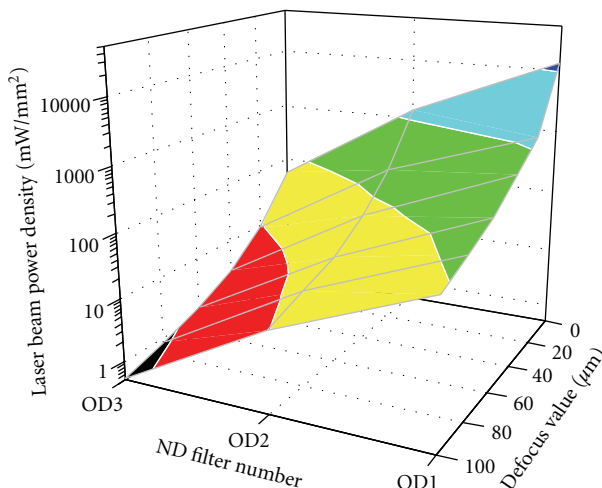


FIGURE 4: Power density of the Raman excitation laser beam measured as a function of ND filter number and the defocus value.

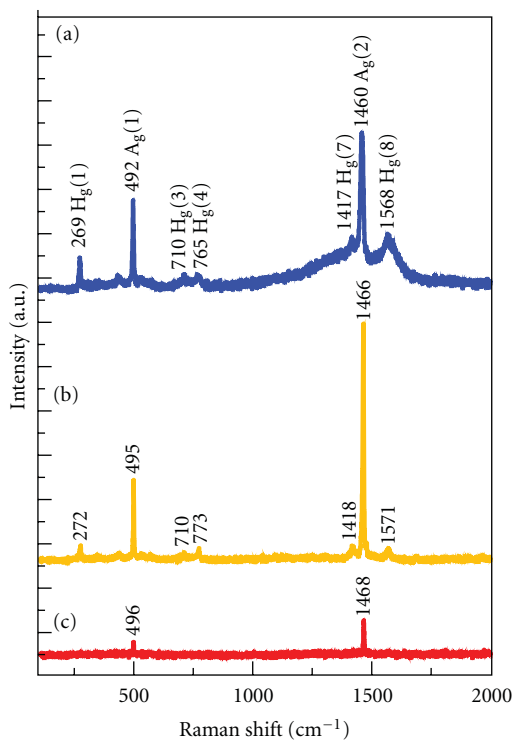


FIGURE 5: Raman spectra of C_{60} NWs. The power density of laser beam (D) is (a) 11800, (b) 1660, and (c) 71.5 mW/mm^2 , respectively.

the red arrows for the high energy doses in Figures 6(c), 6(d), 6(e), and 6(f). These phenomena are supposed to be explained by the temperature rise of the C_{60} NWs exposed to the laser beams, since it is known that the photopolymerized C_{60} molecules decompose into their primary monomers and dimers by heating at temperatures higher than about $100^\circ C$ [13].

The data points obtained using the highest power densities are indicated in each graph of Figure 6 by the black arrows for the exposure time of about 220 s. Figure 7 shows the relationship between the laser beam energy dose

and the $A_g(2)$ peak position for the arrowed data points of Figure 6. The fitted curve of semilog plot is expressed as $y = -2.2x + 1467$, where x represents \log_{10} (laser beam energy dose) and y represents the Raman shift of $A_g(2)$ peak. Using this experimental formula, the energy dose more than about $1520 J/mm^2$ is found to be necessary for the photopolymerization of C_{60} NWs in air, when the laser light with a wavelength of 532 nm is used.

Since it is known that the photopolymerization of C_{60} progresses through the formation of four-membered rings between adjacent C_{60} molecules [11], it is considered that

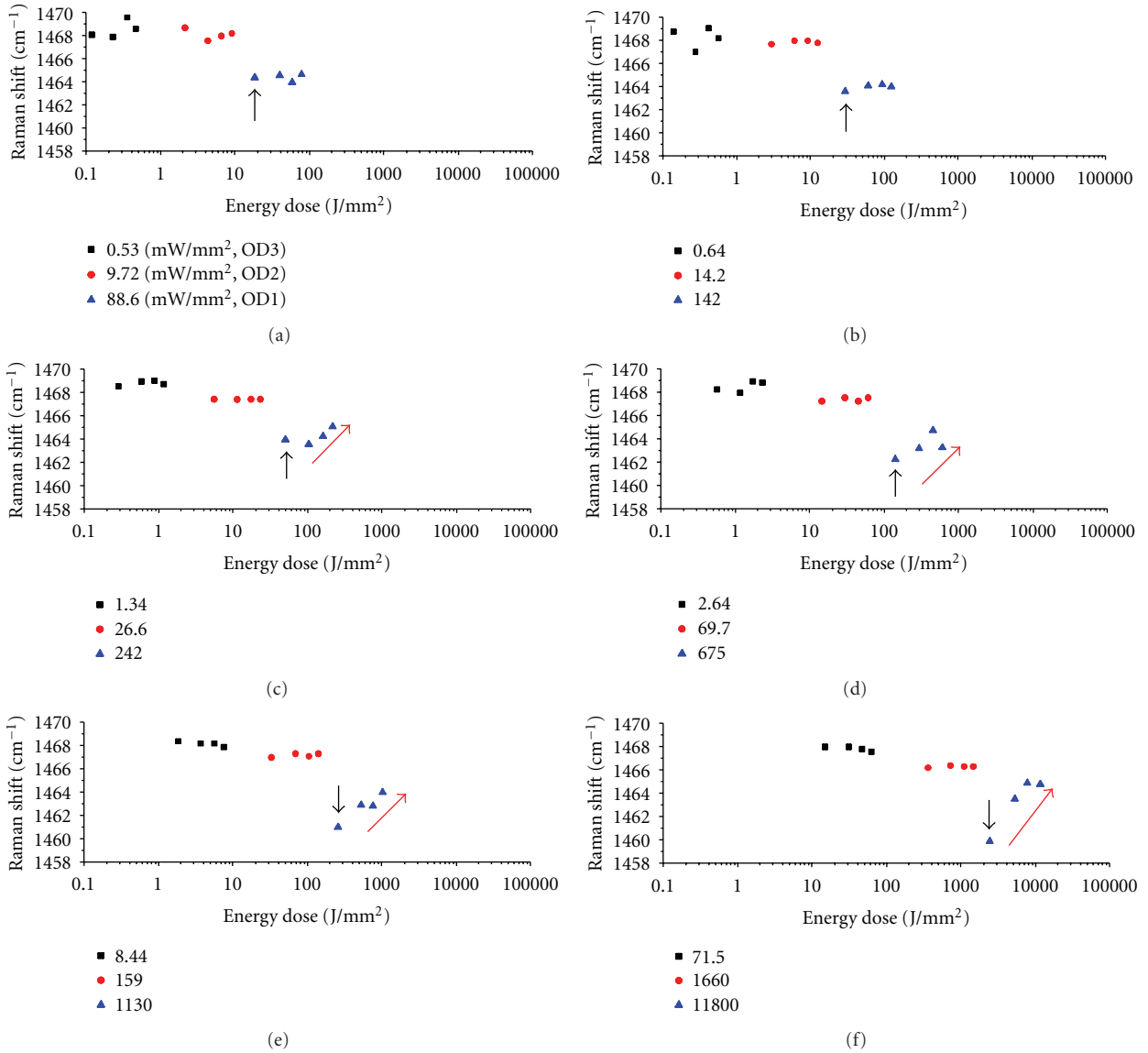


FIGURE 6: $A_g(2)$ peak positions of the Raman spectra of C_{60} NWs under various exposure conditions at the defocus values of (a) $100 \mu\text{m}$, (b) $80 \mu\text{m}$, (c) $60 \mu\text{m}$, (d) $40 \mu\text{m}$, (e) $20 \mu\text{m}$, and (f) $0 \mu\text{m}$ (just focus), corresponding to (a) ~ (f) of Figure 3.

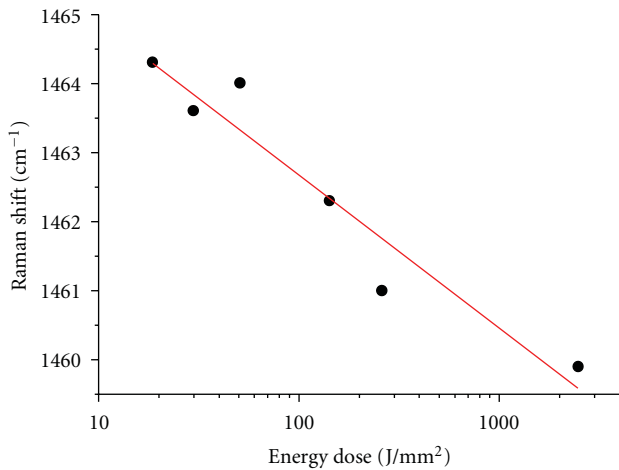


FIGURE 7: Relationship between the Raman shift of $A_g(2)$ peak and the energy dose of C_{60} NWs irradiated by the excitation laser beams.

C_{60} molecules are linearly polymerized by forming the four-membered rings along the growth axis of C_{60} NWs, as was shown in Figure 6 of [2].

In the gas chromatography-mass spectrometry (GC-MS) measurement of solvents contained in the C_{60} NWs that were prepared by use of toluene and IPA, the major residual solvent was toluene, and the content of IPA was very small compared with toluene [14]. Since the residual toluene of C_{60} NWs was measured to be about 0.2% after drying in an Ar atmosphere at 100°C for 30 min. [14], it is considered that the residual toluene of the vacuum-dried samples of C_{60} NWs in the present experiment is negligible and does not influence the Raman profiles.

4. Conclusions

The photopolymerization of C_{60} NWs was investigated by using the Raman laser beam of 532 nm wavelength at various

exposure conditions for the power density and the exposure time in air.

The $A_g(2)$ peak of C_{60} NWs shifted to the lower wavenumbers from that of the as-grown dried C_{60} NWs. However, the $A_g(2)$ peaks were found to move to the higher wavenumbers from the polymerized positions by the irradiation of laser beams for high energy doses at high-power densities, indicating the thermal dissociation of polymerized C_{60} molecules owing to the temperature rise.

An energy dose larger than about 1520 J/mm² was found to be necessary for the laser beam of 532 nm wavelength to obtain the photopolymerized C_{60} NWs.

Acknowledgment

Part of this research was supported by Health and Labour Sciences Research Grants (H21-Chemistry-Ippan-008) from the Ministry of Health, Labour, and Welfare of Japan.

References

- [1] K. Miyazawa, "Synthesis and properties of fullerene nanowhiskers and fullerene nanotubes," *Journal of Nanoscience and Nanotechnology*, vol. 9, no. 1, pp. 41–50, 2009.
- [2] K. Miyazawa, Y. Kuwasaki, A. Obayashi, and M. Kuwabara, " C_{60} nanowhiskers formed by the liquid-liquid interfacial precipitation method," *Journal of Materials Research*, vol. 17, no. 1, pp. 83–88, 2002.
- [3] K. Ogawa, T. Kato, A. Ikegami et al., "Electrical properties of field-effect transistors based on C_{60} nanowhiskers," *Applied Physics Letters*, vol. 88, no. 11, Article ID 112109, 3 pages, 2006.
- [4] P. R. Somani, S. P. Somani, and M. Umeno, "Toward organic thick film solar cells: three dimensional bulk heterojunction organic thick film solar cell using fullerene single crystal nanorods," *Applied Physics Letters*, vol. 91, no. 17, Article ID 173503, 3 pages, 2007.
- [5] X. Zhang, Y. Qu, G. Piao, J. Zhao, and K. Jiao, "Reduced working electrode based on fullerene C_{60} nanotubes@DNA: characterization and application," *Materials Science and Engineering B*, vol. 175, no. 2, pp. 159–163, 2010.
- [6] M. Nakaya, T. Nakayama, and M. Aono, "Fabrication and electron-beam-induced polymerization of C_{60} nanoribbon," *Thin Solid Films*, vol. 464–465, pp. 327–330, 2004.
- [7] M. Tachibana, K. Kobayashi, T. Uchida, K. Kojima, M. Tanimura, and K. Miyazawa, "Photo-assisted growth and polymerization of C_{60} "nano"whiskers," *Chemical Physics Letters*, vol. 374, no. 3–4, pp. 279–285, 2003.
- [8] K. Miyazawa, J. Minato, M. Fujino, and T. Suga, "Structural investigation of heat-treated fullerene nanotubes and nanowhiskers," *Diamond and Related Materials*, vol. 15, no. 4–8, pp. 1143–1146, 2006.
- [9] K. Asaka, R. Kato, K. Miyazawa, and T. Kizuka, "Buckling of C_{60} whiskers," *Applied Physics Letters*, vol. 89, no. 7, Article ID 071912, 3 pages, 2006.
- [10] D. Koide, S. Kato, E. Ikeda, N. Iwata, and H. Yamamoto, "Free electron laser-polymerization of C_{60} grown by liquid-liquid-interfacial precipitation method," *IEICE Transactions on Electronics*, vol. 94, no. 2, pp. 151–156, 2011.
- [11] A. M. Rao, P. Zhou, K. A. Wang et al., "Photoinduced polymerization of solid C_{60} films," *Science*, vol. 259, no. 5097, pp. 955–957, 1993.
- [12] E. Alvarez-Zauco, H. Sobral, E. V. Basiuk, J. M. Saniger-Blesa, and M. Villagrán-Muniz, "Polymerization of C_{60} fullerene thin films by UV pulsed laser irradiation," *Applied Surface Science*, vol. 248, no. 1–4, pp. 243–247, 2005.
- [13] Y. Wang, J. M. Holden, X. X. Bi, and P. C. Eklund, "Thermal decomposition of polymeric C_{60} ," *Chemical Physics Letters*, vol. 217, no. 4, pp. 413–417, 1994.
- [14] M. Watanabe, K. Hotta, K. Miyazawa, and M. Tachibana, "GC-MS analysis of the solvents contained in C_{60} nanowhiskers," *Journal of Physics: Conference Series*, vol. 159, no. 1, Article ID 012010, 2009.

Research Article

Solvation-Assisted Young's Modulus Control of Single-Crystal Fullerene C₇₀ Nanowhiskers

Tokushi Kizuka,¹ Kun'ichi Miyazawa,² and Takayuki Tokumine¹

¹Institute of Materials Science, Graduate School of Pure and Applied Sciences, University of Tsukuba, Tsukuba, Ibaraki 305-8753, Japan

²Fullerene Engineering Group, Materials Processing Unit, National Institute for Materials Science, Namiki, Tsukuba, Ibaraki 305-0044, Japan

Correspondence should be addressed to Tokushi Kizuka, kizuka@ims.tsukuba.ac.jp

Received 6 June 2011; Accepted 31 October 2011

Academic Editor: Zheng Hu

Copyright © 2012 Tokushi Kizuka et al. This is an open access article distributed under the Creative Commons Attribution License, which permits unrestricted use, distribution, and reproduction in any medium, provided the original work is properly cited.

Single-crystal nanowhiskers (NWs) composed of fullerene C₇₀ molecules were synthesized by the liquid-liquid interfacial precipitation method that used *m*-xylene as a saturated solution of C₇₀ molecules. Bending behavior of the individual NWs was observed by *in situ* transmission electron microscopy equipped with nanonewton force measurements using an optical deflection method. The Young's modulus of the NWs was estimated to be 0.3–1.9 GPa, which was 2–7% of the moduli of fullerene NWs with similar diameters synthesized using other solvents, that is, toluene and pyridine. The influence of the solvent used in the precipitation method on Young's modulus is discussed.

1. Introduction

Crystals composed of fullerene molecules have been synthesized by precipitation methods [1–13]. The crystals show various morphologies, that is, plates, films, and rods. In particular, Miyazawa et al. discovered the one-axis preferential growth of fullerene single crystals; a liquid-liquid interfacial precipitation (LLIP) method produces fullerene nanowhiskers (NWs) and nanotubes (NTs) with high length-to-diameter aspect ratios [14]. Because this structural feature is suitable for application in advanced nanodevices, the mechanical properties of these NWs and NTs have been the focus of a considerable amount of research. *In situ* transmission electron microscopy (TEM) equipped with piezomanipulation of individual NWs and NTs enables investigating the mechanical properties of such nanometer-sized materials [15–18].

The Young's moduli of fullerene NWs and NTs have been estimated by this method [19–22]. The structures of fullerene NWs and NTs synthesized by LLIP methods are influenced by solvation behaviors, suggesting that the mechanical properties depend on the solvents used.

Two solvents, that is, toluene and pyridine, have been intensively used for the synthesis of NWs and NTs owing to their high productivity rates. In this study, we synthesized C₇₀ NWs by the LLIP method using another solvent (*m*-xylene) and investigated their mechanical properties by *in situ* TEM.

2. Experimental

A saturated solution of C₇₀ molecules in *m*-xylene was poured into isopropyl alcohol, followed by precipitation of C₇₀ NWs. Then, the solution was added dropwise to an edge of a gold plate. The plate was mounted onto a specimen holder of the transmission electron microscope equipped with a piezomanipulation system at the University of Tsukuba [23–26]. A silicon microcantilever with a nanometer-sized tip that is used for contact-type atomic force microscopy was fixed onto a cantilever holder. Both the specimen and the cantilever holders were inserted in the microscope. The cantilever tip was brought into contact with individual NWs fixed on the plate edges by the piezomanipulation system of the microscope. The tip was then pressed

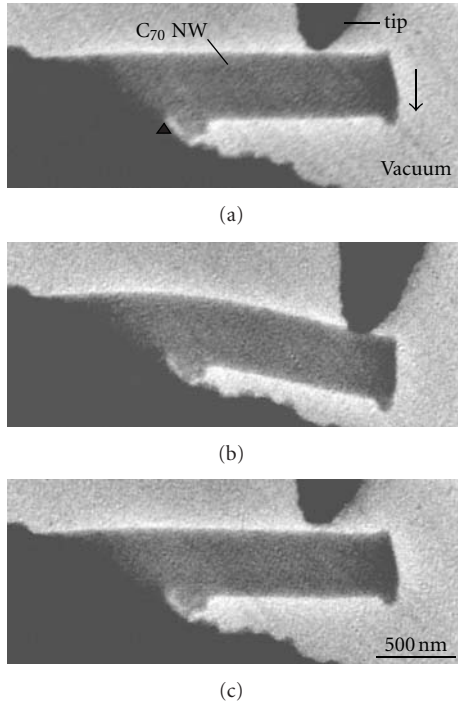


FIGURE 1: Time-sequence series of bright-field images of cantilever-beam-type loading, which causes bending of the C_{70} single-crystal nanowhisker with outer diameter of 410 nm. The left side of the nanowhisker is fixed onto a gold plate. The arrow indicates the loading direction of the cantilever tip for atomic force microscopy. The fulcrum is indicated by the triangle. This bending test was performed in the vacuum.

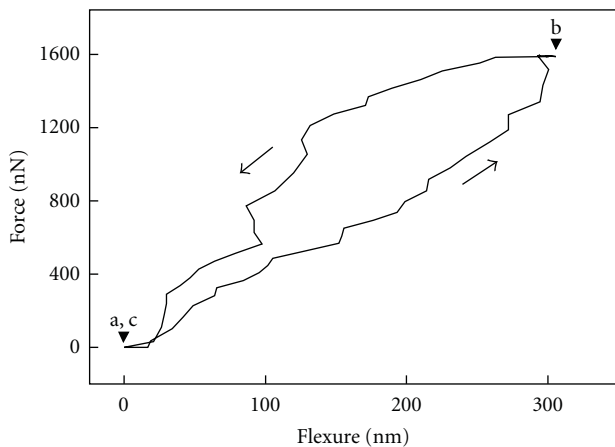


FIGURE 2: Force-flexure curve of C_{70} nanowhisker during bending shown in Figure 1. Points a–c correspond to the states shown in Figures 1(a)–1(c), respectively. The arrows indicate the time path of recording.

on the NWs for bending with cantilever beam-type loading. The cantilever tip was then pulled back to release the force. A series of such manipulations was performed several times for the same NW at room temperature in a vacuum of 1×10^{-5} Pa. The deformation process was observed *in situ* using a video capture system using a charge-coupled device camera

with a time resolution of 17 ms. Simultaneously, the force applied on the NWs was measured by an optical detection of the cantilever deflection used in atomic force microscopy. The spring constant of the cantilever was measured to be 4.7 N/m.

3. Results

Figures 1(a)–1(c) show a time-sequence series of the bright-field images of the bending process of a C_{70} NW protruding from an edge of the gold plate. The dark triangular region in the upper part of each frame is the cantilever tip. The brighter region around the NW is the vacuum. The outer diameter of the NW is 410 nm, and the length of the deformed portion is $1.2 \mu\text{m}$. The crystal structure of the NT was tetragonal. This crystal structure has been observed in dried C_{60} NWs and NTs synthesized by LLIP methods [17–19]. This structure arises from polymerization of fullerene molecules [27]. The longer growth axis of the NW is aligned parallel to [110]. The left side of the NT in Figure 1 was fixed on the gold plate. In the bending test, the cantilever tip was initially placed in contact with the NW (Figure 1(a)). Then, the NT was pressed along the direction indicated by the arrow in Figure 1(a) to cause bending (Figure 1(b)). Subsequently, the tip was released, and the NT recovered its initial straight shape as in Figure 1(c). Thus, this bending behavior corresponds to an elastic deformation.

Figure 2 shows the relationship between the force and flexure during the bending process shown in Figure 1. The points indicated by arrowheads a–c in Figure 2 correspond to the TEM images in Figures 1(a)–1(c). The maximum flexure and loading at the free end were 300 nm and 1590 nN, respectively. Hysteresis is observed in the curve in Figure 2 during the pressing and pulling process of the cantilever tip. It is attributed to the bonding of the cantilever tip with the NW surface [28]. The curve of the pressing process (a–b in Figure 2) can be approximated by one linear component. On the other hand, the curve of the pulling process (b–c in Figure 2) is a sequence of several linear slopes. The slope of the pulling process near point c is similar to that of the pressing process. Thus, we used this slope for the estimation of the Young's modulus of the NW. On the basis of the relationship among force, flexure, and Young's modulus for cantilever-beam loading in standard mechanics of materials, the Young's modulus of the NWs was estimated to be 1.9 ± 0.1 GPa. We performed bending tests with the same type of loading for other NWs with the outer diameters of 580 nm and 770 nm. Their Young's moduli were estimated to be 1.1 ± 0.3 GPa and 0.3 ± 0.3 GPa, respectively.

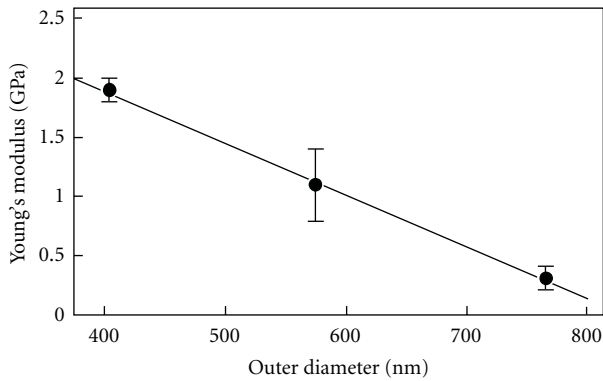
Figure 3 shows the relationship between the Young's modulus and the outer diameter of the C_{70} NWs. Note that the Young's modulus increases as the outer diameter decreases. The relationship is well fitted by a straight line.

4. Discussion

The Young's moduli of single-crystal C_{60} and C_{70} particles, films, NWs, and NTs previously reported are shown

TABLE 1: Young's modulus of fullerene crystals (NW: nanowhisker; NT: nanotube).

Shapes	Molecules	Young's modulus (GPa)	References
Particle	C_{60}	20 ± 5	Hoen et al. [34]
... (fcc [100])	...	8.3 ± 0.6	Kobelev et al. [35]
... (fcc [110])	...	13.2 ± 1	...
... (fcc [111])	...	16.3 ± 1.2	...
Film	...	9.99 ± 1.25	Fioretto et al. [36]
...	...	10	Kolomenskii et al. [32]
...	...	12 ± 1	Coufal et al. [37]
...	...	12.7	Murugavel et al. [33]
...	...	15.9	Shi et al. [7]
...	C_{70}	4 ± 1	Kolomenskii et al. [32]
...	...	8.7	Murugavel et al. [33]
NW (dia. 130 nm)	C_{60}	54 ± 3	Asaka et al. [15]
... (dia. 160 nm)	...	32 ± 6	...
... (dia. 420 nm)	...	28 ± 5	...
... (dia. 123 nm)	...	53–69	Saito et al. [18]
... (dia. 410 nm)	C_{70}	1.9 ± 0.1	The present study
... (dia. 580 nm)	...	1.1 ± 0.3	...
... (dia. 770 nm)	...	0.3 ± 0.3	...
NT (dia. 510 nm)	C_{60}	62–107	Kizuka et al. [17]
... (dia. 270 nm)	C_{70}	68–110	Kizuka et al. [38]
... (dia. 340 nm)	...	82 ± 5	...
... (dia. 470 nm)	...	61 ± 5	...

FIGURE 3: Young's modulus of C_{70} nanowhiskers plotted against the outer diameter. The solid line indicates linear approximation.

in Table 1. The NWs and NTs in previous studies were synthesized by the LLIP method using toluene and pyridine as solvents. The Young's modulus of the present C_{70} NWs synthesized by the LLIP method using *m*-xylene is 0.3–1.9 GPa. Because the Young's modulus of fullerene NWs depends on the outer diameter as shown in Figure 3 and in previous measurements [15, 17, 18], we compared the Young's modulus of the present C_{70} NWs with that of C_{60} NWs with similar outer diameters. The Young's modulus of the present C_{70} NW with an outer diameter of 410 nm is 7% of that of a C_{60} NW with an outer diameter of 420 nm. NTs have different structures from NWs, and the Young's

modulus of C_{60} NTs is ~220% higher than that of C_{60} NWs as shown in Table 1. The ratio of the modulus of C_{70} NWs to C_{60} NTs becomes further lower; the Young's modulus of the C_{70} NW with an outer diameter of 580 nm is 2% of that of a C_{60} NT with an outer diameter of 510 nm. On the other hand, the modulus of the films in Table 1 indicates that by changing the constituent molecules from C_{60} to C_{70} , the modulus decreases only by 30–50%. This implies that the considerable decrease in the Young's modulus of the present NWs cannot be attributed to only the difference in constituent molecules. Therefore, the decrease in the Young's modulus in the present NWs is caused by the difference in solvents used in the LLIP.

During incubation, the crystal structures of fullerene NWs and NTs synthesized by the LLIP method using toluene and pyridine were investigated by Minato and Miyazawa [22]. Pristine NWs show solvated hexagonal structures that transform into face-centered cubic structures by desiccation. Thus, the solvents affect the molecular bonding, configuration, and defect formation in pristine NWs synthesized by LLIP methods. Strain, hollow spaces, or vacancy-cluster type defects are introduced when the molecules are disconnected by insertion of the solvents. It was also reported that stacking faults were formed in the fullerene crystals precipitated in *o*-xylene [29]. As a result, these defects lead to the formation of pores in NWs after desiccation. In particular, the density of pores is higher in the interior region around the center axis [30]. Ringor and Miyazawa proposed that NTs are formed by elution of the interior regions with defects [31].

As Saito et al. discussed, the decrease in Young's modulus of NWs with the outer diameter, which is observed in the present study, suggests the presence of defects in the interior regions [18]. The Young's modulus of fullerene films decreases as density decreases [32, 33]. Therefore, it is deduced that the *m*-xylene molecules remaining in the pristine NWs cause defects in the interior regions after desiccation, leading to the considerable decrease in Young's modulus.

5. Conclusion

Using *in situ* TEM, we performed bending tests on individual single-crystal C_{70} NWs synthesized by the LLIP method using *m*-xylene as the solvent. The Young's modulus of the NWs was estimated to be 0.3–1.9 GPa, which is 2–7% of the moduli of fullerene NWs and NTs with similar diameters synthesized using toluene and pyridine as solvents. It was inferred that the considerable decrease in Young's modulus was caused by the higher number of defects in the interior regions introduced by solvation of *m*-xylene in the pristine NWs. This result reveals that the Young's modulus of NWs can be controlled to a double-digit magnitude by appropriate selection of solvents, leading to design of structural materials using NWs.

Acknowledgment

This study was partly supported by Grants-in-Aid from the Ministry of Education, Culture, Sport, Science and Technology, Japan (nos. 22310065 and 23651127).

References

- [1] W. Kratschmer, L. D. Lamb, K. Fostiropoulos, and D. R. Huffman, "Solid C_{60} : a new form of carbon," *Nature*, vol. 347, no. 6291, pp. 354–358, 1990.
- [2] W. I. F. David, R. M. Ibberson, J. C. Matthewman et al., "Crystal structure and bonding of ordered C_{60} ," *Nature*, vol. 353, no. 6340, pp. 147–149, 1991.
- [3] S. J. Duclos, K. Brister, R. C. Haddon, A. R. Kortan, and F. A. Thiel, "Effects of pressure and stress on C_{60} fullerite to 20 GPa," *Nature*, vol. 351, no. 6325, pp. 380–382, 1991.
- [4] P. A. Heiney, J. E. Fischer, A. R. McGhie et al., "Orientational ordering transition in solid C_{60} ," *Physical Review Letters*, vol. 66, no. 22, pp. 2911–2914, 1991.
- [5] R. L. Meng, D. Ramirez, X. Jiang et al., "Growth of large, defect-free pure C_{60} single crystals," *Applied Physics Letters*, vol. 59, no. 26, pp. 3402–3403, 1991.
- [6] W. Krakow, N. M. Rivera, R. A. Roy, R. S. Ruoff, and J. J. Cuomo, "Epitaxial growth of C_{60} thin films on mica," *Journal of Materials Research*, vol. 7, no. 4, pp. 784–787, 1992.
- [7] X. D. Shi, A. R. Kortan, J. M. Williams, A. M. Kini, B. M. Savall, and P. M. Chaikin, "Sound velocity and attenuation in single-crystal C_{60} ," *Physical Review Letters*, vol. 68, no. 6, pp. 827–830, 1992.
- [8] Y. Yosida, "Scanning electron microscope images of C_{60} whiskers," *Japanese Journal of Applied Physics*, vol. 31, no. 4 B, pp. L505–L507, 1992.
- [9] M. Haluška, H. Kuzmany, M. Vybornov, P. Rogl, and P. Fejdi, "A double-temperature-gradient technique for the growth of single-crystal fullerites from the vapor phase," *Applied Physics A*, vol. 56, no. 3, pp. 161–167, 1993.
- [10] J. Z. Liu, J. W. Dykes, M. D. Lan, P. Klavins, R. N. Shelton, and M. M. Olmstead, "Vapor transport growth of C_{60} crystals," *Applied Physics Letters*, vol. 62, no. 5, pp. 531–532, 1993.
- [11] J. L. de Boer, S. van Smaalen, V. Petricek, M. Dusek, M. A. Verheijen, and G. Meijer, "Hexagonal close-packed C_{60} ," *Chemical Physics Letters*, vol. 219, no. 5-6, pp. 469–472, 1994.
- [12] F. Michaud, M. Barrio, S. Toscani et al., "Solid-state studies on single and decagonal crystals of C_{60} grown from 1,2-dichloroethane," *Physical Review B*, vol. 57, no. 17, pp. 10351–10358, 1998.
- [13] S. Toscani, H. Allouchi, J. L. Tamarit et al., "Decagonal C_{60} crystals grown from n-hexane solutions: solid-state and aging studies," *Chemical Physics Letters*, vol. 330, no. 5-6, pp. 491–496, 2000.
- [14] K. Miyazawa, A. Obayashi, and M. Kuwabara, " C_{60} nanowhiskers in a mixture of lead zirconate titanate sol- C_{60} toluene solution," *Journal of the American Ceramic Society*, vol. 84, no. 3-12, pp. 3037–3039, 2001.
- [15] K. Asaka, R. Kato, K. Miyazawa, and T. Kizuka, "Buckling of C_{60} whiskers," *Applied Physics Letters*, vol. 89, no. 7, Article ID 071912, 2006.
- [16] R. Kato, K. Asaka, K. Miyazawa, and T. Kizuka, "In situ high-resolution transmission electron microscopy of elastic deformation and fracture of nanometer-sized fullerene C_{60} whiskers," *Japanese Journal of Applied Physics*, vol. 45, no. 10 A, pp. 8024–8026, 2006.
- [17] T. Kizuka, K. Saito, and K. Miyazawa, "Young's modulus of crystalline C_{60} nanotubes studied by in situ transmission electron microscopy," *Diamond and Related Materials*, vol. 17, no. 6, pp. 972–974, 2008.
- [18] K. Saito, K. Miyazawa, and T. Kizuka, "Bending process and Young's modulus of fullerene C_{60} nanowhiskers," *Japanese Journal of Applied Physics*, vol. 48, no. 1, Article ID 010217, 2009.
- [19] K. Miyazawa, " C_{70} nanowhiskers fabricated by forming liquid/liquid interfaces in the systems of toluene solution of C_{70} and isopropyl/alcohol," *Journal of the American Ceramic Society*, vol. 85, no. 5, pp. 1297–1299, 2002.
- [20] K. Miyazawa, K. Hamamoto, S. Nagata, and T. Suga, "Structural investigation of the C_{60}/C_{70} whiskers fabricated by forming liquid-liquid interfaces of toluene with dissolved C_{60}/C_{70} and isopropyl alcohol," *Journal of Materials Research*, vol. 18, no. 5, pp. 1096–1103, 2003.
- [21] K. Miyazawa, Y. Kuwasaki, K. Hamamoto, S. Nagata, A. Obayashi, and M. Kuwabara, "Structural characterization of C_{60} nanowhiskers formed by the liquid/liquid interfacial precipitation method," *Surface and Interface Analysis*, vol. 35, no. 1, pp. 117–120, 2003.
- [22] J. I. Minato and K. Miyazawa, "Structural characterization of C_{60} nanowhiskers and C_{60} nanotubes fabricated by the liquid-liquid interfacial precipitation method," *Diamond and Related Materials*, vol. 15, no. 4-8, pp. 1151–1154, 2006.
- [23] T. Kizuka, K. Yamada, S. Deguchi, M. Naruse, and N. Tanaka, "Cross-sectional time-resolved high-resolution transmission electron microscopy of atomic-scale contact and noncontact-type scanings on gold surfaces," *Physical Review B*, vol. 55, no. 12, pp. R7398–R7401, 1997.

- [24] T. Kizuka, "Atomic process of point contact in gold studied by time-resolved high-resolution transmission electron microscopy," *Physical Review Letters*, vol. 81, no. 20, pp. 4448–4451, 1998.
- [25] T. Kizuka, "Direct atomistic observation of deformation in multiwalled carbon nanotubes," *Physical Review B*, vol. 59, no. 7, pp. 4646–4649, 1999.
- [26] T. Kizuka, "Atomic configuration and mechanical and electrical properties of stable gold wires of single-atom width," *Physical Review B*, vol. 77, no. 15, Article ID 155401, 2008.
- [27] A. V. Soldatov, G. Roth, A. Dzyabchenko et al., "Topochemical polymerization of C_{70} controlled by monomer crystal packing," *Science*, vol. 293, no. 5530, pp. 680–683, 2001.
- [28] S. Fujisawa and T. Kizuka, "Effect of lateral displacement of atomic force microscope tip caused by contact scanning studied by in situ transmission electron microscopy," *Japanese Journal of Applied Physics*, vol. 42, no. 10 A, pp. L1182–L1184, 2003.
- [29] M. Gu and T. B. Tang, "Thermoanalytical studies on the order-disorder transition in C_{60} doped with C_{70} ," *Journal of Physics: Condensed Matter*, vol. 7, no. 38, pp. 7475–7479, 1995.
- [30] R. Kato and K. Miyazawa, "Cross-sectional structural analysis of C_{60} nanowhiskers by transmission electron microscopy," *Diamond and Related Materials*, vol. 20, no. 3, pp. 299–303, 2011.
- [31] C. L. Ringor and K. Miyazawa, "Fabrication of solution grown C_{60} fullerene nanotubes with tunable diameter," *Journal of Nanoscience and Nanotechnology*, vol. 9, no. 11, pp. 6560–6564, 2009.
- [32] A. A. Kolomenskii, M. Szabadi, and P. Hess, "Laser diagnostics of C_{60} and C_{70} films by broadband surface acoustic wave spectroscopy," *Applied Surface Science*, vol. 86, no. 1–4, pp. 591–596, 1995.
- [33] P. Murugavel, C. Narayana, A. Govindaraj, A. K. Sood, and C. N. R. Rao, "Brillouin scattering from C_{70} and C_{60} films: a comparative study of elastic properties," *Chemical Physics Letters*, vol. 331, no. 2–4, pp. 149–153, 2000.
- [34] S. Hoen, N. G. Chopra, X. D. Xiang et al., "Elastic properties of a van der Waals solid: C_{60} ," *Physical Review B*, vol. 46, no. 19, pp. 12737–12739, 1992.
- [35] N. P. Kobelev, R. K. Nikolaev, Y. M. Soifer, and S. S. Khasanov, "The elastic stiffness matrix of single-crystal C_{60} ," *Chemical Physics Letters*, vol. 276, no. 3–4, pp. 263–265, 1997.
- [36] D. Fioretto, G. Carlotti, G. Socino et al., "Brillouin-scattering determination of the elastic constants of epitaxial fcc C_{60} film," *Physical Review B*, vol. 52, no. 12, pp. R8707–R8710, 1995.
- [37] H. Coufal, K. Meyer, R. K. Grygier, M. de Vries, D. Jenrich, and P. Hess, "Measurement of the elastic properties of evaporated C_{60} films by surface acoustic waves," *Applied Physics A*, vol. 59, no. 1, pp. 83–86, 1994.
- [38] T. Kizuka, K. Miyazawa, and T. Tokumine, "Young's modulus of single-crystal fullerene C_{70} nanotubes," *Journal of Nanotechnology*, vol. 2012, Article ID 969357, 5 pages, 2012.

Research Article

Synthesis of Carbon Nanocapsules and Nanotubes Using Fe-Doped Fullerene Nanowhiskers

Tokushi Kizuka,¹ Kun'ichi Miyazawa,² and Daisuke Matsuura¹

¹*Institute of Materials Science, Graduate School of Pure and Applied Sciences, University of Tsukuba, Tsukuba, Ibaraki 305-8753, Japan*

²*Fullerene Engineering Group, Advanced Materials Processing Unit, National Institute for Materials Science, Namiki, Tsukuba, Ibaraki 305-0044, Japan*

Correspondence should be addressed to Tokushi Kizuka, kizuka@ims.tsukuba.ac.jp

Received 15 July 2011; Revised 14 October 2011; Accepted 16 October 2011

Academic Editor: Zheng Hu

Copyright © 2012 Tokushi Kizuka et al. This is an open access article distributed under the Creative Commons Attribution License, which permits unrestricted use, distribution, and reproduction in any medium, provided the original work is properly cited.

We synthesized iron-(Fe)-doped C₆₀ nanowhiskers (NWs) by applying the liquid-liquid interfacial precipitation method that employs a C₆₀-saturated toluene solution and a solution of 2-propanol containing ferric nitrate nonahydrate (Fe(NO₃)₃·9H₂O). Fe particles of 3–7 nm in diameter were precipitated in the NWs. By heating at 1173 K, the NWs were transformed into hollow and Fe₃C-encapsulated carbon nanocapsules and carbon nanotubes.

1. Introduction

Fullerene nanocages, such as carbon nanocapsules (CNCs) and carbon nanotubes (CNTs), can be used to encapsulate functional nanomaterials, leading to potential applications in catalysis and drug delivery [1–13]. Encapsulation of functional nanomaterials has been performed by simultaneous evaporation of metals and diamond by arc discharge [4, 5, 8–10]. Chemical vapor deposition, electron irradiation, and thermal decomposition have also been applied to produce CNCs and CNTs [1, 3, 12, 13]. An efficient synthesis method for hollow CNCs using single-crystal fullerene nanowhiskers (NWs) was found by Asaka et al. [14–18]. Fullerene NWs can be synthesized by a simple method, that is, the liquid-liquid interfacial precipitation (LLIP) method [19–23]. In addition, in the LLIP method, fullerene NWs can be doped with metallic particles using C₆₀ derivatives and additives such as metal nitrate nonahydrates in solution [24–26]. Such metallic particles act as catalysts in the syntheses of CNCs and CNTs. In this study, we demonstrate the synthesis of iron-(Fe)-doped C₆₀ NWs using the LLIP method and their application to produce CNCs and CNTs.

2. Method

C₆₀ powders were dissolved in toluene to prepare a C₆₀-saturated solution with a solubility of 2.8 g/L. In addition, ferric nitrate nonahydrate (Fe(NO₃)₃·9H₂O) was dissolved in 2-propanol to give a concentration of 0.1 M. Next, the C₆₀ toluene solution was transferred to a glass vial, and the solution of 2-propanol containing Fe(NO₃)₃·9H₂O was added to form a liquid-liquid interface. The vial was maintained at 278 K for one week, and the mixed solution was then filtered to extract precipitates. The precipitates were dried and heated under high vacuum at 1173 K for 1 h. The as-precipitated and heat-treated specimens were dispersed on microgrids and observed by scanning electron microscopy (SEM) and transmission electron microscopy (TEM).

3. Results

Figure 1 shows an SEM image of as-precipitated C₆₀ NWs. Figures 2(a) and 2(b) show a bright-field image and a high-resolution image of an as-precipitated C₆₀ NW, respectively. The diameters of the as-precipitated NWs ranged from 0.5 to 7.5 μm, as shown in Figure 3. Lattice fringes with a spacing of

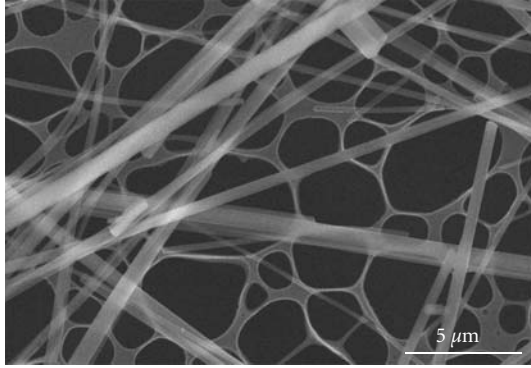


FIGURE 1: Scanning electron microscopy secondary-electron image of as-precipitated Fe-doped C_{60} nanowhiskers. The nanowhiskers are supported on microgrid.

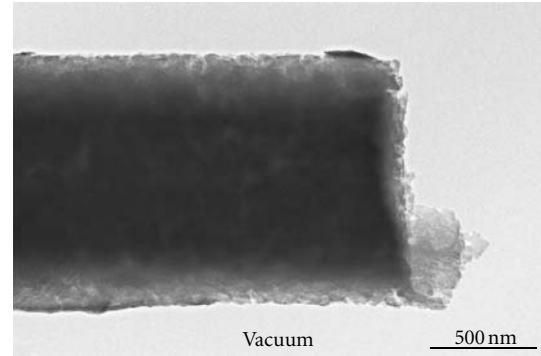
0.52 nm were observed in the NWs, as shown in Figure 2(b). Figure 2(c) shows a selected-area electron diffraction pattern of the NW depicted in Figure 2(a). The high-resolution images and diffraction patterns reveal that the NWs have a tetragonal lattice with lattice constants of $a = 0.99$ nm and $c = 2.1$ nm. The lattice fringes with a spacing of 0.52 nm depicted in Figure 2(b) correspond to the (004) plane. The long axis of the NW is parallel to the (110) direction. Figure 2(d) shows a high-resolution image of an NW surface, where Fe particles with diameters in the range 3–7 nm were observed. Thus, the LLIP method using a solution of $Fe(NO_3)_3 \cdot 9H_2O$ in 2-propanol resulted in the precipitation of Fe particles in the C_{60} NWs. Owing to the precipitation of Fe particles, the crystal growth of the NW was inhibited; as a result, the surfaces of the NWs had a rough topography. Therefore, the Fe-doped NWs presented here differ from pure C_{60} NWs, which are surrounded by plane surfaces [19–23].

Figure 4 shows a bright-field image of the heat-treated specimen. Hollow and encapsulating CNCs and CNTs were observed in the specimen, as were chains of CNCs.

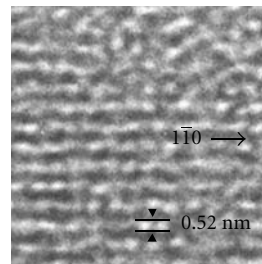
Figure 5 shows a bright-field image and a selected-area diffraction pattern of a CNC encapsulating a particle. The 220, 230, and 050 spots of Fe_3C (cementite) are observed; the particle was identified to be Fe_3C .

Figures 6(a) and 6(b) show high-resolution images of an Fe_3C -encapsulated CNC. The diameters of the CNCs and the Fe_3C particles ranged 25–175 nm and 5–100 nm, respectively, as shown in Figure 7. The Fe_3C particle does not completely fill the empty space at the core of the CNC. Figure 6(c) shows a high-resolution image of graphene layers in an Fe_3C -encapsulated CNC. The spacing of the graphene layers around the surface is 0.34 nm, whereas the spacing decreases to 0.31 nm around the graphene/ Fe_3C interface.

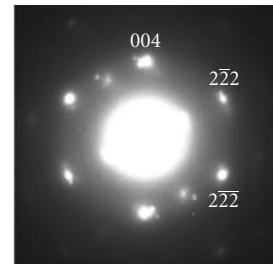
Figure 8(a) shows a high-resolution image of a CNT encapsulating Fe_3C particles (Figures 8(b) and 8(c)), similar to the case of the CNCs. The Fe_3C particles encapsulated by the CNTs showed rod shapes, as shown in Figure 8(a). This is different from the spherical Fe_3C particles observed in CNCs. The diameters of the CNTs and the Fe_3C particles ranged 10–70 nm and 5–50 nm, respectively, as shown in Figure 9.



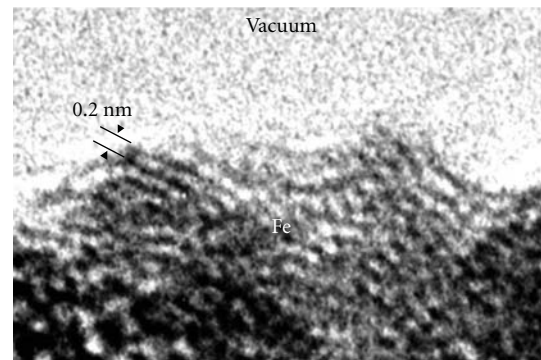
(a)



(b)



(c)



(d)

FIGURE 2: (a) Bright-field image, (b) high-resolution image, and (c) selected-area electron diffraction pattern of as-precipitated Fe-doped C_{60} nanowhisker. The diameter of the nanowhisker is 1.2 μm . (d) High-resolution image of Fe particles in the nanowhisker. The lattice fringes of (110) $_{Fe}$ with a spacing of 0.20 nm are observed.

The formation of CNCs and CNTs was not confirmed when the heating temperature was changed to 873 K, 973 K, 1073 K, and 1123 K. When the heating time was shortened to 0.5 h at 1173 K, the size distribution of CNCs and CNTs was similar.

4. Discussion

4.1. Formation of Fe_3C Particles. In the as-precipitated NWs, Fe particles 3–7 nm in diameter were observed. On the other hand, after heating at 1173 K, the diameter of the Fe_3C particles in the CNCs and CNTs was found to increase to 5–100 nm. This implies that the Fe particles had aggregated, and carbon was solved in them during heating. According to Ding et al., pure Fe particles that are several nanometers in

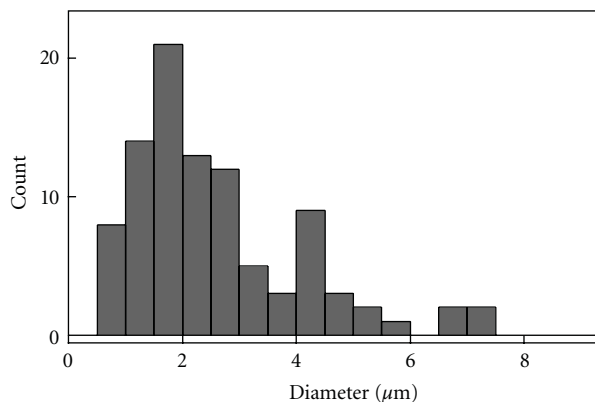


FIGURE 3: Histogram of diameters of as-precipitated Fe-doped C₆₀ nanowhiskers.

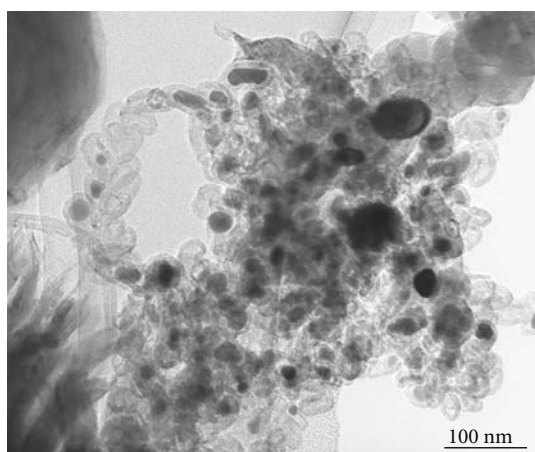
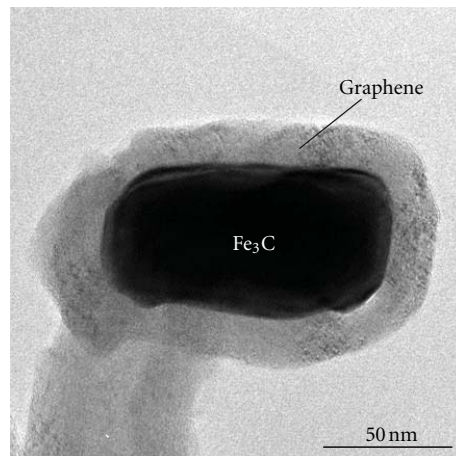


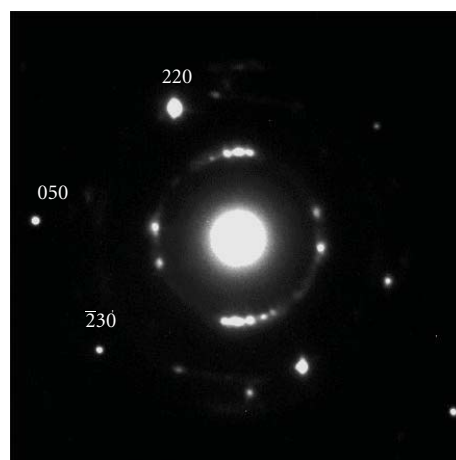
FIGURE 4: Bright-field image of carbon nanocapsules and carbon nanotubes in heat-treated specimen.

size melt at 1000 K [27]. The melting Fe particles are mobile and fuse together. Fe-carbides with a carbon concentration of more than 50 at% are formed when the melting Fe particles contact with carbon [28]. During cooling, the solubility limit of carbon in the particles decreases and is followed by the precipitation of graphene layers on the particle surfaces. In this experiment, the particles observed in CNCs and CNTs were Fe₃C. When the carbon concentration of the particles at coagulation exceeds 25 at%, Fe₃C particles can be formed in the CNCs and CNTs. Schaper et al. showed from *in situ* TEM that graphene layers precipitate from Fe₃C particles at 1143 K [28]. This temperature is 30 K lower than the heating temperature used in this study. The Fe₃C particles shrink owing to the precipitation, resulting in the formation of an empty space at the core of the CNCs [28]. Such empty spaces were observed in this study, as shown in Figure 6(a). Fe₃C is a quasistable phase and does not transform to other phases at room temperature.

4.2. Formation of CNCs and CNTs. According to Saito, CNCs are produced by the precipitation of carbon from catalysts, that is, metallic or carbide particles [10]. Thus, a CNC encapsulating a particle is initially formed. Jiao et al. showed



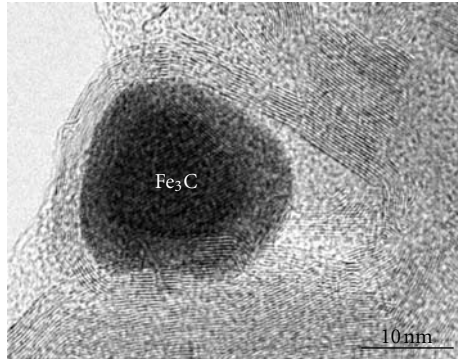
(a)



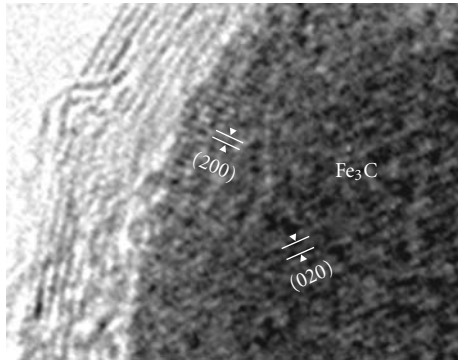
(b)

FIGURE 5: (a) Bright-field image and (b) selected-area diffraction pattern of Fe₃C-encapsulated carbon nanocapsule. The 220, 230, and 050 spots of Fe₃C are observed.

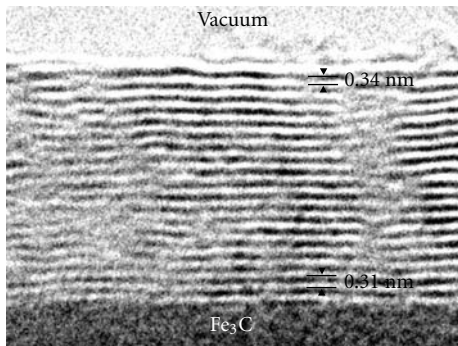
from *in situ* TEM that in, CNCs encapsulating Fe and Fe carbide particles, the particle is removed from the CNC at 1173–1373 K [29]. As Ding et al. discussed, the driving force of the particle removal relates to the temperature and concentration gradients in the particle, which are caused by the precipitation of graphene layers [27]. By removal of the particle, the CNC is broken and a hole is formed. This hole is closed by subsequent growth of the layers [30], and hence, a hollow CNC is formed. Subsequently, the next precipitation starts. Thus, the precipitation of graphene layers occurs intermittently. By repeating the processes of precipitation and the removal of the encapsulated particle, hollow CNCs proliferate and one CNC encapsulating the particle remains. The CNCs aggregate, resulting in the formation of a chain, as shown in Figure 4. In the case of the formation of CNTs, the encapsulated Fe₃C particles showed rod shapes. Tubular graphene layers, that is, CNTs, precipitate around such rod-shaped particles. Once a CNT is formed, the encapsulated rod-shaped particle shifts along the symmetric axis of the CNT. Carbon precipitates continuously on the same region of the particle, along one direction, leading to growth of



(a)



(b)

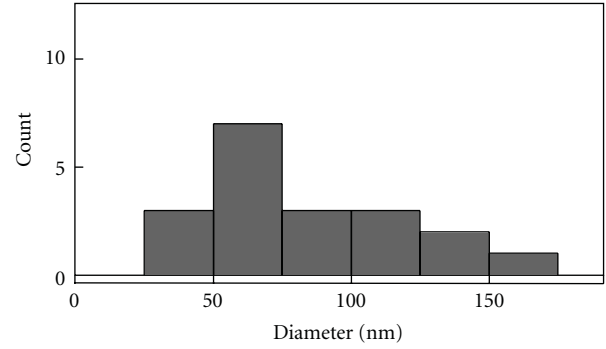


(c)

FIGURE 6: (a) High-resolution images of Fe_3C -encapsulated carbon nanocapsule and (b) enlargement of the (200) and (020) lattice fringes of the Fe_3C particle in (a). (c) Graphene layers of the carbon nanocapsule in (a).

the CNT [10]. According to Jourdain et al., a particle is encapsulated in a CNT owing to the strong interfacial tension between the inner wall of the CNT and the surface of the melting particle [31]. It is suggested that the interfacial tension of the rod-shaped particles encapsulated by CNTs is higher than that of the spherical particles in the CNCs. In this study, both CNCs and CNTs were formed in the same specimen. Whether CNCs or CNTs are formed depends on the shape of each encapsulated particle.

4.3. *Decrease in the Spacing of Graphene Layers of CNCs.* The spacing of the graphene layers decreases to 0.31 nm around



(a) Outer diameter of carbon nanocapsules

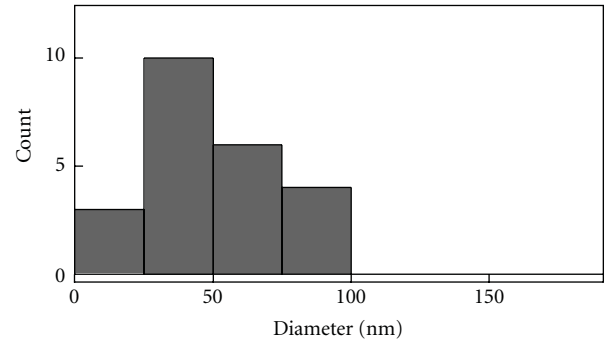
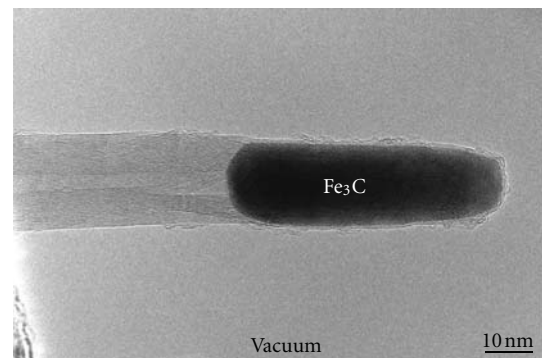
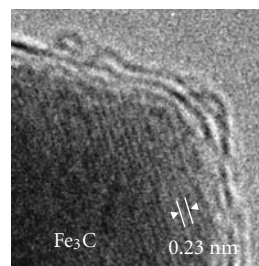
(b) Fe_3C particles encapsulated by carbon nanocapsules

FIGURE 7: Histograms of (a) outer diameter of carbon nanocapsules and (b) Fe_3C particles encapsulated by carbon nanocapsules.



(a)



(b)



(c)

FIGURE 8: (a) High-resolution image of Fe_3C -encapsulated carbon nanotube. (b) Enlargement of the nanotube tip in (a). (c) Selected-area electron diffraction pattern of the Fe_3C particle encapsulated by the nanotube in (a).

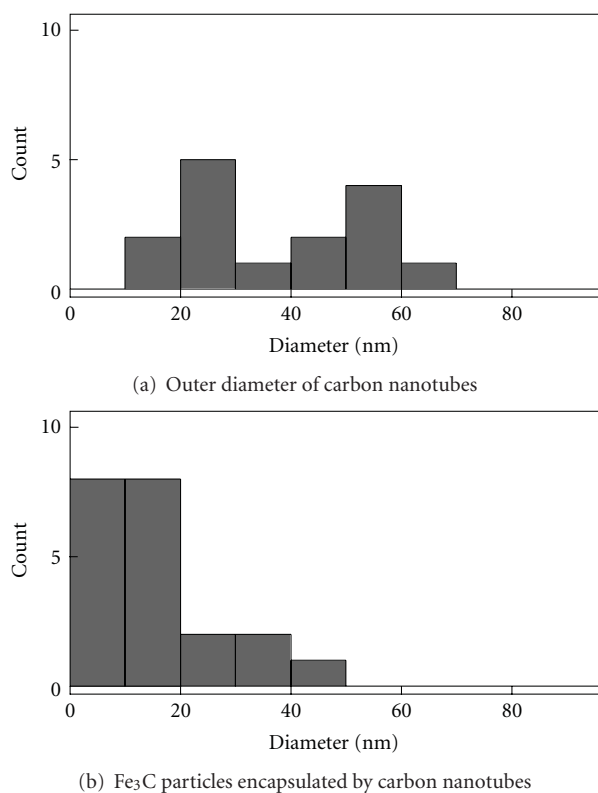


FIGURE 9: Histograms of outer diameter of carbon nanotubes (a) and Fe₃C particles encapsulated by carbon nanotubes (b).

the graphene/Fe₃C interfaces. This spacing is 10% smaller than that of graphite. Banhart et al. observed a similar reduction in the spacing of graphene layers in carbon onions and interpreted the reduction on the basis of compression and the transition of orbitals from sp^2 to sp^3 [12, 13]. In the Fe₃C-encapsulated CNCs produced in this study, the smaller spacing of the graphene layers is related to the Fe₃C particle. The bonding between the graphene layers and the Fe₃C particle may contribute to the transition of orbitals from sp^2 to sp^3 .

4.4. Characteristics of the Present Method. In this production method of Fe₃C-encapsulated CNCs and CNTs, Fe-doped FNWs were synthesized by the LLIP method and heating was applied. The LLIP method is performed by a simple process: the mixing of two kinds of liquid around room temperature. Thus, the control of the production is easier than other methods for production of CNCs and CNTs encapsulating particles, for example, arc discharges [4, 7–9]. In particular, when production quantity becomes larger, the simple control is advantageous although the LLIP process need longer time, for example, one week.

5. Conclusion

Fe-doped C₆₀ NWs were synthesized by the LLIP method using a C₆₀-saturated toluene solution and 2-propanol containing Fe(NO₃)₃·9H₂O. The additive of Fe(NO₃)₃·9H₂O resulted in the precipitation of Fe particles in the C₆₀ NWs.

Heat treatment of the NWs at 1173 K produced both hollow CNCs and CNTs. Fe₃C-encapsulated CNCs and CNTs were also produced. The present method can be applied to synthesize NWs including other metals, for example, cobalt and nickel. Thus, the present method is suitable for the production of CNCs and CNTs encapsulating various foreign nanomaterials.

Acknowledgment

This study was partly supported by Grants-in-Aid from the Ministry of Education, Culture, Sport, Science, and Technology, Japan (nos. 22310065 and 23651127).

References

- [1] R. D. Heidenreich, W. M. Hess, and L. L. Ban, "A test object and criteria for high resolution electron microscopy," *Journal of Applied Crystallography*, vol. 1, no. 1, pp. 1–19, 1968.
- [2] S. Iijima, "Helical microtubules of graphitic carbon," *Nature*, vol. 354, no. 6348, pp. 56–58, 1991.
- [3] D. Ugarte, "Curling and closure of graphitic networks under electron-beam irradiation," *Nature*, vol. 359, no. 6397, pp. 707–709, 1992.
- [4] R. S. Ruoff, D. C. Lorents, B. Chan, R. Malhotra, and S. Subramoney, "Single crystal metals encapsulated in carbon nanoparticles," *Science*, vol. 259, no. 5093, pp. 346–348, 1993.
- [5] Y. Saito, T. Yoshikawa, M. Inagaki, M. Tomita, and T. Hayashi, "Growth and structure of graphitic tubules and polyhedral particles in arc-discharge," *Chemical Physics Letters*, vol. 204, no. 3-4, pp. 277–282, 1993.
- [6] Y. Saito, T. Yoshikawa, M. Okuda et al., "Carbon nanocapsules encaging metals and carbides," *Journal of Physics and Chemistry of Solids*, vol. 54, no. 12, pp. 1849–1860, 1993.
- [7] Y. Saito, T. Yoshikawa, M. Okuda et al., "Carbon nanocapsules encaging metals and carbides," *Journal of Physics and Chemistry of Solids*, vol. 54, no. 12, pp. 1849–1860, 1993.
- [8] M. Tomita, Y. Saito, and T. Hayashi, "LaC₂ encapsulated in graphite nano-particle," *Japanese Journal of Applied Physics*, vol. 32, no. 2 B, pp. 280–282, 1993.
- [9] T. Hihara, H. Onodera, K. Sumiyama et al., "Magnetic properties of iron in nanocapsules," *Japanese Journal of Applied Physics*, vol. 33, no. 1 A, pp. L24–L25, 1994.
- [10] Y. Saito, "Nanoparticles and filled nanocapsules," *Carbon*, vol. 33, no. 7, pp. 979–988, 1995.
- [11] Y. Saito, K. Nishikubo, K. Kawabata, and T. Matsumoto, "Carbon nanocapsules and single-layered nanotubes produced with platinum-group metals (Ru, Rh, Pd, Os, Ir, Pt) by arc discharge," *Journal of Applied Physics*, vol. 80, no. 5, pp. 3062–3067, 1996.
- [12] F. Banhart, P. Redlich, and P. M. Ajayan, "Irradiation effects in carbon nanostructures," *Chemical Physics Letters*, vol. 292, no. 4–6, pp. 554–560, 1998.
- [13] F. Banhart, "Irradiation effects in carbon nanostructures," *Reports on Progress in Physics*, vol. 62, no. 8, pp. 1181–1221, 1999.
- [14] K. Asaka, R. Kato, Y. Maezono, R. Yoshizaki, K. Miyazawa, and T. Kizuka, "Light-emitting filaments composed of nanometer-sized carbon hollow capsules," *Applied Physics Letters*, vol. 88, no. 5, Article ID 051914, pp. 1–3, 2006.
- [15] K. Asaka, R. Kato, K. Miyazawa, and T. Kizuka, "Deformation of multiwalled nanometer-sized carbon capsules," *Applied Physics Letters*, vol. 89, no. 19, Article ID 191914, 2006.

- [16] K. Asaka, R. Kato, R. Yoshizaki, K. Miyazawa, and T. Kizuka, "Conductance of carbon nanocapsule junctions," *Physical Review B*, vol. 76, no. 11, Article ID 113404, 2007.
- [17] T. Kizuka, R. Kato, and K. Miyazawa, "Structure of hollow carbon nanocapsules synthesized by resistive heating," *Carbon*, vol. 47, no. 1, pp. 138–144, 2009.
- [18] T. Kizuka, R. Kato, and K. Miyazawa, "Surface breakdown dynamics of carbon nanocapsules," *Nanotechnology*, vol. 20, no. 10, Article ID 105205, 2009.
- [19] K. Miyazawa, A. Obayashi, and M. Kuwabara, " C_{60} nanowhiskers in a mixture of lead zirconate titanate Sol- C_{60} toluene solution," *Journal of the American Ceramic Society*, vol. 84, no. 3-12, pp. 3037–3039, 2001.
- [20] K. Miyazawa, " C_{70} nanowhiskers fabricated by forming liquid/liquid interfaces in the systems of toluene solution of C_{70} and isopropyl alcohol," *Journal of the American Ceramic Society*, vol. 85, no. 5, pp. 1297–1299, 2002.
- [21] K. Miyazawa, Y. Kuwasaki, A. Obayashi, and M. Kuwabara, " C_{60} nanowhiskers formed by the liquid-liquid interfacial precipitation method," *Journal of Materials Research*, vol. 17, no. 1, pp. 83–88, 2002.
- [22] K. Miyazawa, K. Hamamoto, S. Nagata, and T. Suga, "Structural investigation of the C_{60}/C_{70} whiskers fabricated by forming liquid-liquid interfaces of toluene with dissolved C_{60}/C_{70} and isopropyl alcohol," *Journal of Materials Research*, vol. 18, no. 5, pp. 1096–1103, 2003.
- [23] K. Miyazawa, Y. Kuwasaki, K. Hamamoto, S. Nagata, A. Obayashi, and M. Kuwabara, "Structural characterization of C_{60} nanowhiskers formed by the liquid/liquid interfacial precipitation method," *Surface and Interface Analysis*, vol. 35, no. 1, pp. 117–120, 2003.
- [24] K. Miyazawa, T. Mashino, and T. Suga, "Structural characterization of the $C_{60}[C(COOC_2H_5)_2]$ whiskers prepared by the liquid-liquid interfacial precipitation method," *Journal of Materials Research*, vol. 18, no. 11, pp. 2730–2735, 2003.
- [25] K. Miyazawa and T. Suga, "Transmission electron microscopy investigation of fullerene nanowhiskers and needle-like precipitates formed by using C_{60} and $(\eta^2-C_{60})Pt(PPh_3)_2$," *Journal of Materials Research*, vol. 19, no. 8, pp. 2410–2414, 2004.
- [26] K. Miyazawa and T. Suga, "Transmission electron microscopy investigation of tubular and capsular needlelike crystals of C_{60} produced by the liquid-liquid interfacial precipitation method," *Journal of Materials Research*, vol. 19, no. 11, pp. 3145–3148, 2004.
- [27] F. Ding, A. Rosén, and K. Bolton, "The role of the catalytic particle temperature gradient for SWNT growth from small particles," *Chemical Physics Letters*, vol. 393, no. 4–6, pp. 309–313, 2004.
- [28] A. K. Schaper, H. Hou, A. Greiner, and F. Phillipp, "The role of iron carbide in multiwalled carbon nanotube growth," *Journal of Catalysis*, vol. 222, no. 1, pp. 250–254, 2004.
- [29] J. Jiao, S. Seraphin, X. Wang, and J. C. Withers, "Preparation and properties of ferromagnetic carbon-coated Fe, Co, and Ni nanoparticles," *Journal of Applied Physics*, vol. 80, no. 1, pp. 103–108, 1996.
- [30] D. Ugarte, "How to fill or empty a graphitic onion," *Chemical Physics Letters*, vol. 209, no. 1-2, pp. 99–103, 1993.
- [31] V. Jourdain, H. Kanzow, M. Castignolles, A. Loiseau, and P. Bernier, "Sequential catalytic growth of carbon nanotubes," *Chemical Physics Letters*, vol. 364, no. 1-2, pp. 27–33, 2002.

Review Article

Study of Carbon Nanotube-Substrate Interaction

Jaqueline S. Soares and Ado Jorio

Departamento de Física, Universidade Federal de Minas Gerais, 31270-901 Belo Horizonte, MG, Brazil

Correspondence should be addressed to Jaqueline S. Soares, jsoares@fisica.ufmg.br

Received 13 July 2011; Accepted 27 September 2011

Academic Editor: Angel Berenguer

Copyright © 2012 J. S. Soares and A. Jorio. This is an open access article distributed under the Creative Commons Attribution License, which permits unrestricted use, distribution, and reproduction in any medium, provided the original work is properly cited.

Environmental effects are very important in nanoscience and nanotechnology. This work reviews the importance of the substrate in single-wall carbon nanotube properties. Contact with a substrate can modify the nanotube properties, and such interactions have been broadly studied as either a negative aspect or a solution for developing carbon nanotube-based nanotechnologies. This paper discusses both theoretical and experimental studies where the interaction between the carbon nanotubes and the substrate affects the structural, electronic, and vibrational properties of the tubes.

1. Introduction

Nanotechnology has attracted broad interest in the society. Nanomaterials are unusual because of size-related effects and strong dimensionality dependence, leading to fascinating novel effects in their physicochemical properties. Carbon nanotubes are highly stable nanosystems due to the strong covalent bonds between the carbon atoms on the nanotube structure, being considered a model system for nanoscience [1]. Together with the stability, their unique structural, chemical, mechanical, thermal, optical, optoelectronic, and electronic properties are responsible for the interest in the fundamental properties of carbon nanotubes, so that their potential to applications continues to increase [2–4].

When moving into real applications, it is very important to consider the effect of the environment surrounding the nanostructure [1]. This work is devoted to how carbon nanotube properties can be affected by the presence of the substrate where the tube is sitting. The interactions between carbon nanotubes and the substrate have been widely studied as a drawback or a solution for the development of nanotechnologies based on carbon nanotubes [5–30].

The challenge to use carbon nanotubes is the formation of organized arrangements that are technologically important. Recent advances have been achieved by controlling the shape and organization of nanotubes on surfaces [23, 26–29, 31, 32]. Such manipulation offers the possibility of designing and building a wide range of nanoelectronic devices. In

this case, the structural and electronic properties of carbon nanotubes, considering the interaction with substrates in which they are deposited, are crucial for applications. In fact, recent studies have shown that a strong interaction between carbon nanotubes and the substrate can lead to important changes in the nanotube properties. For example, single-wall carbon nanotubes (SWNTs) deposited on quartz gives rise to a superlattice of semiconductor and metal system, where the conduction behavior depends on the orientation between the tube and the substrate [30]. That is, the tube and the substrate are actually a new system that cannot be considered as only the sum of tube plus substrate.

This paper is organized as follows. Section 2 provides a summary of the effects related to substrate-induced tube flattening and distortion; Section 3 presents how environmental conditions change the optical transition energies (E_{ii}) and vibrational properties, focusing on the radial breathing mode (RBM) frequency (ω_{RBM}); Section 4 discusses tube-substrate bonding; Section 5 discusses the substrate-induced superlattice formation; Section 6 discusses the effects on bundled and multiwalled tubes; finally, in Section 7 the conclusions are presented.

2. Tube Flattening and Distortion

First-principle calculations show that the tube flattening (see Figure 1), which can appear when the tube is sitting

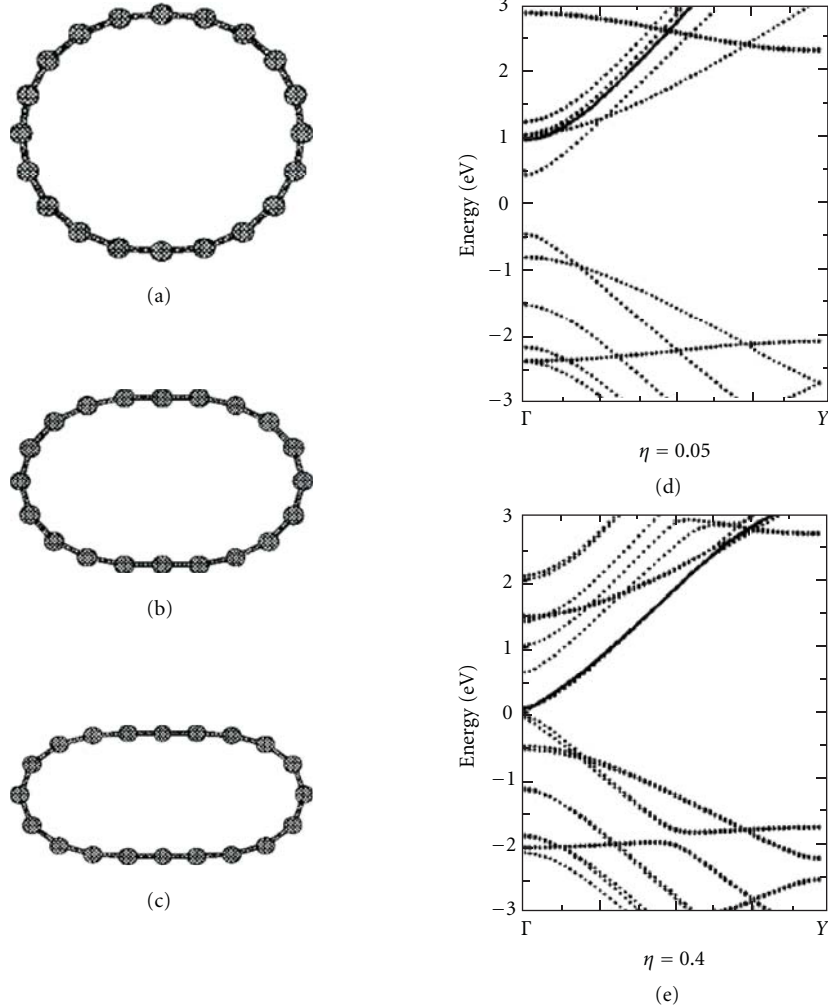


FIGURE 1: Relaxed cross-sections (a) of (10,0) carbon nanotubes with different degrees of flatness in (b) and (c). (d) and (e) plot the electronic band structures for a flattened (10,0) nanotube. The flatness is characterized by η which is defined as $\eta = (D_0 - d)/D_0$, where D_0 is the original diameter of the nanotube and d is the distance between two straight lines of the cross-section (adapted from [13]).

on a substrate, induces a semiconductor-metal transition. Such transition can be understood in terms of hybridization effects induced by the curvature [13], the flattening causing a progressive reduction of the band gap [13]. The tip of an atomic force microscope (AFM) can be used to control the shape and position of carbon nanotubes dispersed on a surface, and the interaction between nanotubes and the surface is crucial for such manipulations [31, 33]. The nanotubes tend to distort so as to conform to the topography of the substrate. Such distortions can have implications for the electronic structure and electrical transport properties of nanotubes [31]. Carbon nanotube is more strongly adhered to the substrate when the H atoms between the tube and the substrate are removed [22], thus making it difficult to disturb the tube with the AFM tip, for example. On the fully hydrogenated silicon surface, the electronic structure of a metallic carbon nanotube is almost unchanged. Removing partially the H atoms from the adsorption site, there is an enhancement in the metallicity of the system. However,

when all the H atoms are removed, the system becomes a semiconductor [19, 20]. Stronger interaction between the carbon and surface atoms might also occur, and this subject will be discussed in Section 4.

3. E_{ii} and ω_{RBM}

The Raman spectroscopy has been widely used for characterizing SWNTs [8, 34, 35]. The mapping technique based on the Raman spectroscopy makes it possible to study local environmental effects of the Raman features from one single SWNT. For example, effects introduced by the substrates can be studied through comparative Raman lineshape studies of SWNTs freely suspended crossing trenches versus sitting on substrates [7, 11, 36–38]. The Raman spectra variations observed in these works can be attributed to nanotube-substrate interactions.

The RBM can be used to study the nanotube diameter (d_t) through its frequency (ω_{RBM}), to probe the electronic

structure through its intensity (I_{RBM}) and to perform an (n, m) assignment of a single isolated SWNT from analysis of both d_t and I_{RBM} [8, 34, 35, 42]. The Kataura plot [39] shows the optical transition energies (E_{ii}) for each (n, m) SWNT as a function of ω_{RBM} . Figure 2 [39, 40, 43, 44] shows E_{ii} ranging from E_{11}^S up to E_{66}^S (S stands for semiconducting tube and M stands for metallic tubes). Figure 2(a) uses the standard relation $\omega_{\text{RBM}} = 227/d_t$ [40], and the E_{ii} values were obtained using the empirical equation [44]:

$$E_{ii}(p, d_t) = 1.074(p/d_t)[1 + 0.467 \log(0.812d_t/p)] + \beta_p \cos 3\theta/d_t^2, \quad (1)$$

where p is defined as 1, 2, 3, ..., 8 for $E_{11}^S, E_{22}^S, E_{11}^M, \dots, E_{66}^S$, respectively, and the values of β can be found in [44].

For SWNTs on top of crystalline miscut quartz, there is a strong environmental effect related to the tube-substrate interaction [41], although the RBM frequencies are homogeneous along the whole SWNTs. The (n, m) assignment for the observed RBMs (up triangles in Figure 2(a)) cannot be performed using the standard Kataura plot because several up triangles fall in regions where there are no corresponding E_{ii} values from any (n, m) SWNT (no matching between triangles and circles). For RBM-based (n, m) identification, it is important to find out how various environmental conditions change the optical transition energies (E_{ii}) and the ω_{RBM} values [40, 41, 43–45]. Figure 2(b) shows the matching between the Kataura plot and many RBM Raman data for the SWNTs on crystalline miscut quartz [41]. For this (n, m) assignments, two parameters (E_{ii} and C) can be changed to adjust in the Kataura plot: (i) the carbon nanotube-substrate interaction exhibits a $\omega_{\text{RBM}}(d_t)$ relation according to the following equation [40]:

$$\omega_{\text{RBM}} = (227/d_t)\sqrt{1 + C * d_t^2}, \quad (2)$$

with $C = 0.082 \pm 0.009 \text{ nm}^{-2}$ and (ii) a downshift of $\Delta E_{ii} = -100 \pm 30 \text{ meV}$ in E_{ii} with respect to the standard values [44, 45]. These results suggest a strong interaction between carbon nanotube and crystalline quartz substrate as compared to other types of samples, since ΔE_{ii} and C are the largest values among different tube-environment systems analyzed in the literature [40, 41, 44, 45].

It is important to remember that the experimental results in the literature have been fitted with the relation $\omega_{\text{RBM}} = \mathbf{A}/d_t + \mathbf{B}$, instead of (2), with the values for \mathbf{A} and \mathbf{B} varying from paper to paper [45]. However, Araujo et al. showed that all the results between ω_{RBM} and d_t found in the literature can be described by (2), with the advantage that C is the only adjustable constant, weighting the effect of the different medium surrounding the SWNT samples [40, 41, 44, 45].

4. Tube-Substrate Bonding

4.1. Semiconductor-Metal Transition. Stronger interactions between carbon nanotubes and the surface can occur. The most commonly used substrate is silicon substrate [14, 19–21]. The formation of Si–C bonds enhances the metallic

character of the nanotube by the contact with the Si surface [14]. The electronic properties of the adsorbed tubes are also sensitive to the carbon nanotube adsorption sites. The structure is semiconducting when the adsorbed carbon nanotube is perpendicular to the Si dimers, while it is metallic when the nanotube is parallel to the Si dimers [21].

Another substrate studied is a quartz substrate. Among the substrates used to study the interaction of carbon nanotubes with the substrate, the quartz was identified as a promising substrate for the growth of complex structures of SWNT [23, 26–29]. An interesting carbon nanotube structure was grown on quartz substrate, the so-called SWNT serpentine, which consists of a series of straight, parallel, and regularly spaced segments, connected by alternating U-turns [23]. The formation of these structures can be explained by the mechanism called “falling spaghetti” [23, 46]. This structure provides a great deal of information because the same SWNT exhibits different interactions due to the tube-substrate morphology [30]. The first-principles calculations shown in Figure 3 stand for SWNT serpentine placed on top of a crystalline quartz [30]. Upon relaxation, the silicon atoms in the contact region are found to experience an upward displacement and the bottom part of the nanotube becomes flat, resulting from a strong interaction between carbon bonding states and surface dangling bonds [30]. While Figure 3(a) shows the electronic structure of an original semiconductor (19,0) nanotube, Figure 3(b) shows the results of this same (19,0) tube, but now interacting with a SiO_2 slab having Si dangling bonds (see insets to Figure 3). The existence of a periodic array of interaction sites causes the appearance of dispersive bands crossing the Fermi level (red rectangle in Figure 3(b)), showing the semiconductor-metal transition [30]. The next sections present experimental evidence about these substrate effects.

The interaction of carbon nanotubes with other substrates has also been studied [7, 17, 23–29], for example, InAs substrate. First-principle calculations were used to study the binding mechanisms for zigzag carbon nanotubes on InAs substrate. Nanotubes preferentially bind to surface in atoms, while maintaining their own internal structural and electronic integrity [17].

4.2. Experimental Evidence for Metal-Semiconductor Transition for SWNTs on Quartz. The G band Raman frequency depends sensitively on strain [47–49] and doping [50–52]. When the tube becomes metallic, the Kohn anomaly appears for the longitudinal optical (LO) phonon, which decreases and broadens the peak [51, 53]. In addition, frequency shifts of the dominant second-order mode (G' band, at $2600\text{--}2700 \text{ cm}^{-1}$) can also be used to differentiate between electron donor (n) and acceptor (p) doping, even at the individual single-atom doping level [54]. These aspects of the Raman spectroscopy are exemplified in the two representative Raman spectra shown in Figure 4. The frequency behavior for both the G and G' bands is a method to characterize the strain [47–49] and doping [50–52] induced by the tube-substrate interaction and to understand the observation of a mixed metal-semiconductor behavior (see spectrum in Figure 4(b)).

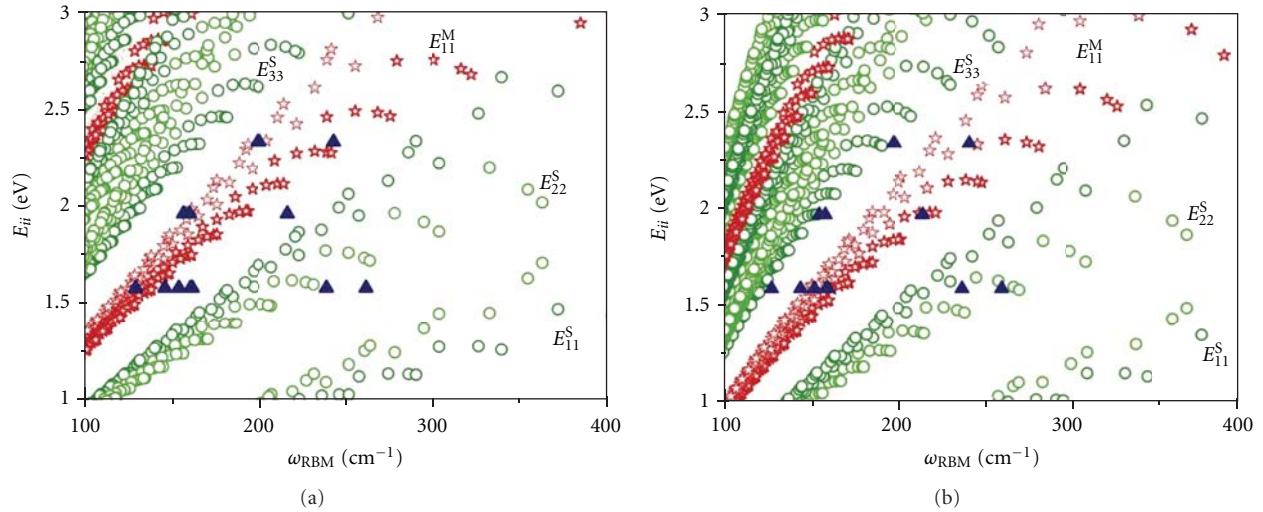


FIGURE 2: Optical transition energies (E_{ij}) of each (n, m) SWNT plotted versus the respective RBM frequencies (ω_{RBM}), known as the Kataura plot [39]. The optical transition energies of semiconducting (circles) and metallic (stars) SWNTs are shown. Up triangles represent RBM results obtained from resonance Raman spectroscopy, taken from crystalline miscut quartz [23]. The y -axis for these up triangles coordinates is chosen by considering resonance at $E_{ij} \approx E_{\text{laser}}$. The x -axis is chosen by considering a correspondence between ω_{RBM} and d_t : (a) the standard relation $\omega_{\text{RBM}} = 227/d_t$ [40], and E_{ij} from (1); (b) Equation (2) with $C = 0.082 \text{ nm}^{-2}$ and a 100 meV downshift in E_{ij} with respect to the values in (a) (adapted from [41]).

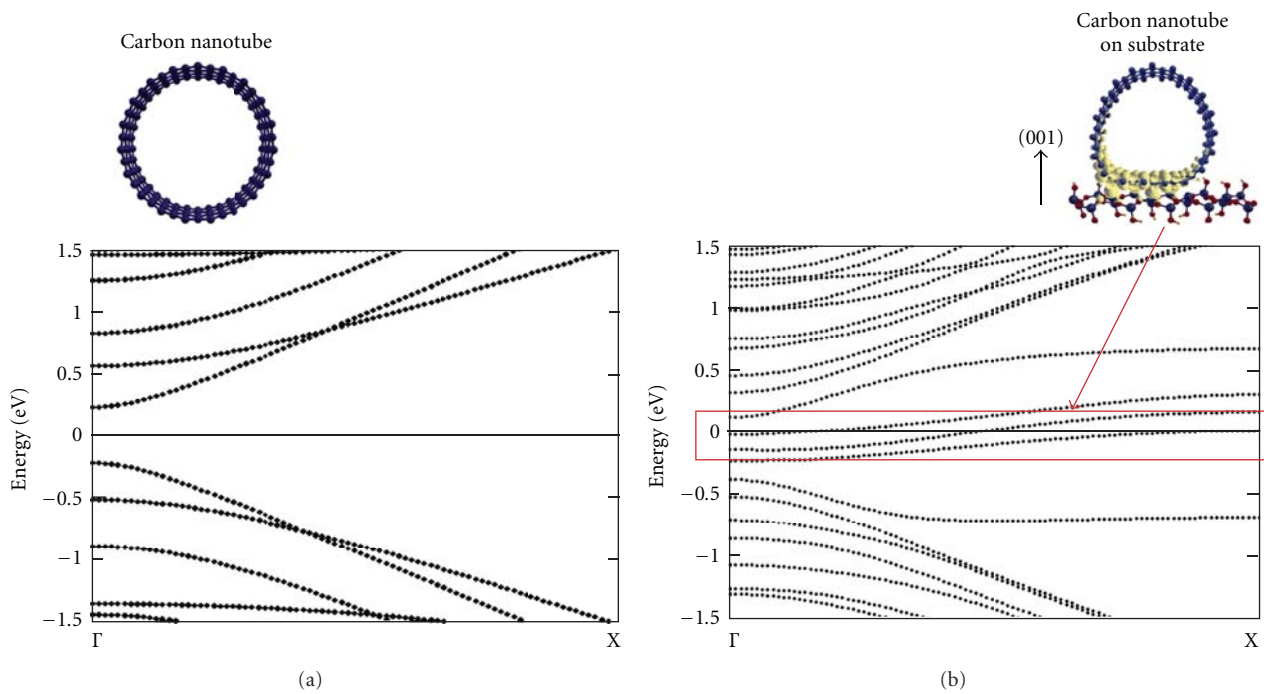


FIGURE 3: Band structure of the $(19,0)$ carbon nanotube: (a) pristine and (b) interacting with a (001) surface of a quartz substrate with tube axis along (100) . The Fermi level is set to zero. The insets show the respective atomic structures. The yellowish clouds in the inset (b) represent a plot of the electronic density for states within energies of up to 0.1 eV around the Fermi level (red rectangle in (b)). The bands responsible for the gap closure are localized spatially in the contact region along the flat surface of the nanotube (adapted from [30]).

Figures 4(a) and 4(b) show two G band Raman spectra from the same SWNT deposited on crystalline quartz. The difference is that (a) is located at a serpentine segment where the tube-substrate interaction is weak, while (b) is located at a serpentine segment where the tube-substrate

interaction is strong. The G band features in spectrum (a) are typical of a semiconducting SWNT [8], while the G band features in spectrum (b) show a sum of metal and semiconductor behavior. The change in the G band profile indicates a metallic versus semiconductor character, with

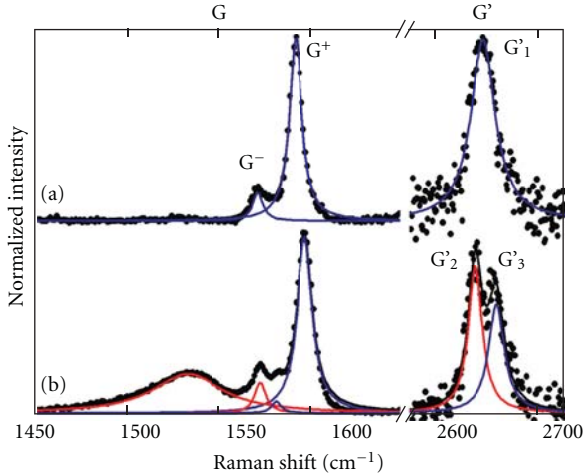


FIGURE 4: Raman spectroscopy analysis of one SWNT grown on quartz. Spectrum (a) exhibits a G band with a line shape typical of a semiconducting SWNT. Spectrum (b) exhibits a G band showing a mixture of lineshapes typical of semiconducting (blue Lorentzians) and a metallic (red Lorentzians) SWNT behavior. Note that the G' peak splits in (b) (adapted from [30]).

an additional broad peak at the G band in 1530 cm^{-1} due to the Kohn anomaly [53]. Spectrum (a) shows a G' band with a single peak, while spectrum (b) shows a splitting of the G' band. The shifts in the G' band features can be explained by doping, which can cause either an upshift or downshift due to doping, according to [54]. The G and G' bands spectra are different, clearly related to the morphology, that is, tube segments aligned and not aligned along the steps of the crystalline miscut quartz substrate. Points located at the portions of the SWNT crossing the quartz atomic steps exhibit only one G' peak and two G band peaks characteristic of semiconducting SWNTs (Figure 4(a)). Points where the nanotube lies along to the substrate atomic steps exhibit two G' peaks (see spectrum (b) in Figure 4), and the G band exhibits four peaks (two characteristic of a semiconducting SWNT—blue Lorentzians in spectrum (b) of Figure 4—and two characteristic of a metallic SWNT—red Lorentzians in spectrum (b) of Figure 4).

4.3. Nonhomogeneous SWNT-Substrate Interactions. As we have seen, the substrate changes the G band behavior. However, the substrate does not affect all nanotubes in the same way; that is, the SWNT may show different interactions with the substrate indicating nonhomogenous interaction. In the case discussed in Figure 4, the ω_{G^+} is observed to oscillate according with the tube-substrate morphology [30]. The frequency variation can be explained by the stronger strain [47–49] and doping [50–52] in the flat segments, corroborating the stronger versus weaker modulated tube-substrate interaction when the nanotube lies along versus across the substrate surface steps [30].

In general, the G^+ band behavior for SWNT serpentine grown on crystalline quartz can be separated in three groups: (i) frequency has its maximum value at the center

of straight segments along the steps and minimum at the center of the U-shaped segments—this is the case discussed in Figure 4 [30] and shown in Figure 5(a) for another SWNT serpentine [55]; (ii) frequency changes very little (Figure 5(b)), indicating very weak or no tube-substrate interaction [55]; (iii) frequency “jumps” at certain points in the SWNT serpentine (Figure 5(c)), indicating a very strong and localized perturbation [55]. These effects can be generally understood as a result of different types of interaction with the substrate, generated during the synthesis of SWNT serpentine [46] and local aspects, such as impurities and local charging [30, 55].

5. Superlattice Formation

5.1. The Raman Spectroscopy. As shown in Section 4.2, the G-band frequency (ω_G) can be used to distinguish between metallic and semiconducting SWNTs, through strong differences in their Raman lineshapes [35, 56]. Figure 6(a) shows a spectroscopic confocal image of a SWNT serpentine. Figure 6(b) gives a general view of the G band Raman spectra of the carbon nanotube at the 1–5 locations from the single-wall carbon nanotube shown in Figure 6(a), taken along the serpentine. Regions 1, 3, and 5 in Figure 6(a) were taken at the flat segments of the SWNT serpentine, which are strongly attached to the quartz substrate, thus exhibiting strong tube-substrate interaction. When the tube goes down the steps (regions 2 and 4 in Figure 6(a)), the interaction is weak. The appearance and disappearance of the lower frequency G^- feature ($\sim 1540\text{ cm}^{-1}$), related to the tube-substrate morphology and interaction, show that the periodic change on the tube-substrate interaction generates a set of alternate metal-semiconductor tube segments, that is, a superlattice formation [30].

5.2. Electric Force Microscopy (EFM). Electric force microscopy (EFM) has been shown to differentiate metal and semiconducting SWNTs [57], and it was used to corroborate the Raman results for the superlattice formation. Figure 7 provides a schematic for understanding the metal versus semiconductor EFM behavior. The EFM measures the dielectric response of the whole sample, that is, SWNT plus substrate. In general, when the tip approaches the dielectric material, there is a decrease in $\Delta\omega$. Then two effects happen in our measurement, as depicted in Figure 7: (1) $\Delta\omega$ decreases when the tip approaches the tube, reaches a minimum when at the top of the tube, and increases back when the tip departs from the tube (see column (a) in Figure 7); (2) $\Delta\omega$ shows a slight increase during the constant-height scan, because the EFM tip retracts when crossing the tube (see column (b) in Figure 7), and the change in surface-tip distance causes a lowering in the tip-substrate interaction. The overall result is a sum of these two effects (see column (c) in Figure 7). In the case of semiconducting SWNT (blue), when the EFM tip is going on top of the tube, the tip retraction due to change in surface height causes a lowering in the tip-substrate interaction, giving rise to the “W shaped” in the semiconducting SWNTs. This effect is indeed present in the metallic SWNT (red), but due to the stronger and

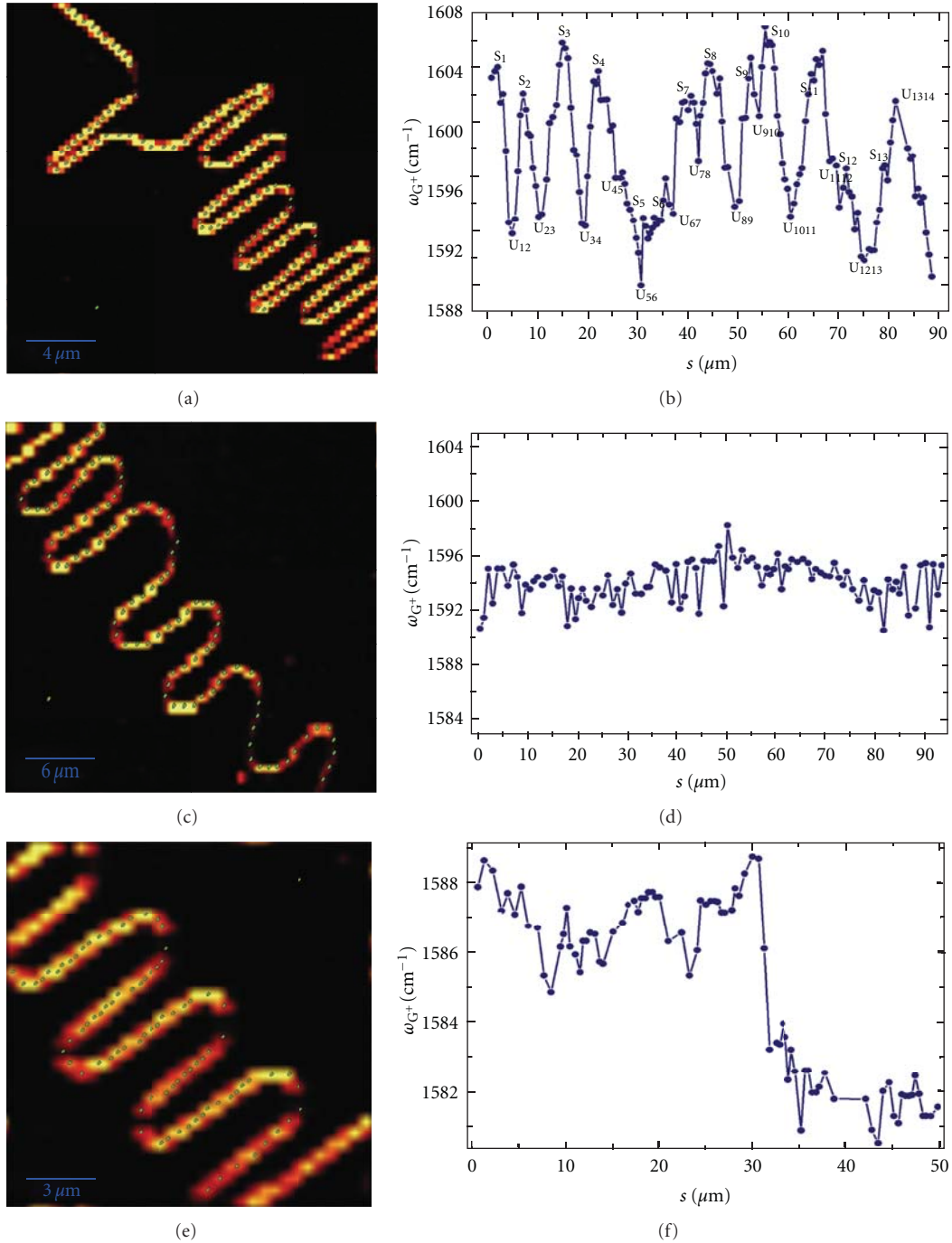


FIGURE 5: (a), (c), and (e) show spectroscopic images of G band of SWNT serpentine on quartz substrate, using the excitation laser wavelength of 532 nm ($E_{\text{laser}} = 2.33$ eV). (b), (d), and (f) show the G^+ frequency of these SWNTs, observed in all points indicated by green pointers in (a), (c), and (e), respectively, plotted as a function of the distance s , measured along the SWNT: (b) frequency has maximum and minimum following the tube-substrate morphology (a); (d) variation in frequency within experimental accuracy; (f) frequency “jumps” [55].

sharper dielectric response, it shows just a slight distorter “V-shaped” EFM profile [30].

Figure 8 shows the EFM analysis of the same SWNT discussed in Figure 6. The EFM measurements (Figure 8) for a SWNT serpentine placed on top of a crystalline quartz substrate support the superlattice formation (mixed metal-

semiconducting character) observed in the Raman spectroscopy [30]. Even though the EFM signal seems homogeneous in Figure 8(a), a more careful analysis reveals structure in this line shape, as shown in the line profiles across two different regions in the nanotube presented in Figure 8(b). The red and blue profiles correspond to the regions marked

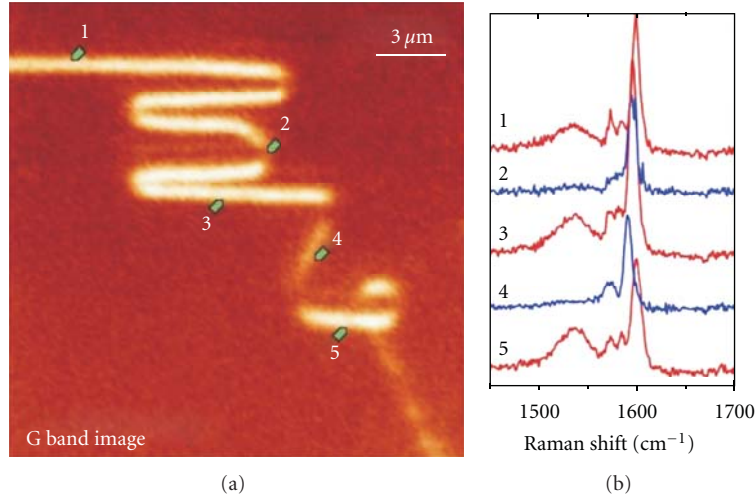


FIGURE 6: (a) Confocal image of the G band integrated intensity ($E_{\text{laser}} = 1.96 \text{ eV}$, spatial resolution $\sim 500 \text{ nm}$) for SWNT serpentine on $(1 \bar{1} 0 1)$ quartz. The spectral intensity is stronger in segments aligned along the steps because of the light polarization dependence for the Raman scattering [8]. (b) The G band at different points on the same serpentine shown in (a). An additional broad peak at the G band ($\sim 1540 \text{ cm}^{-1}$) has been observed on the flat sections (spectra 1, 3, and 5), indicating a metallic character. This additional peak disappears in spectra 2 and 4, indicating a semiconducting character (adapted from [30]).

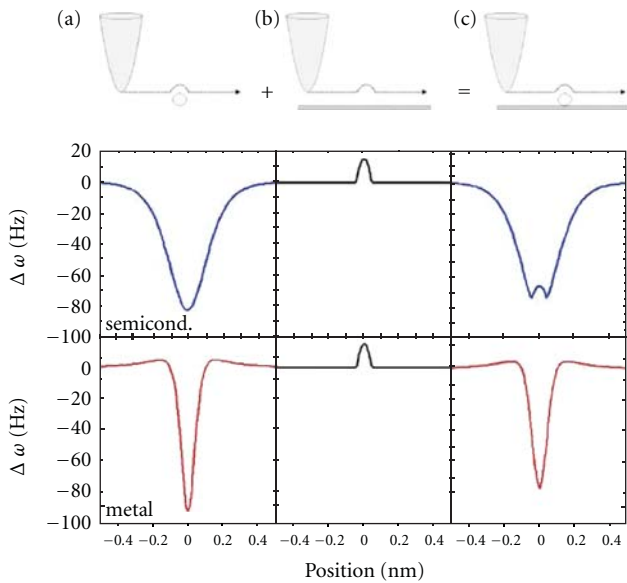


FIGURE 7: The EFM profiles for semiconducting and metallic SWNTs. In column (a), the effect of the EFM tip crossing a semiconductor (blue) and a metallic (red) SWNTs on $\Delta\omega$ is shown. The lineshapes are different due to the differences in dielectric response. In column (b) the effect of the EFM tip retracting from the substrate on $\Delta\omega$ is shown. Here the effect is the same for both semiconductors and metals. In column (c) the two effects are combined. The equations in [57] were used to build these plots [30].

by the red and blue lines in Figure 8(a), respectively. The “W-shaped” blue profile, typical for a region with weak substrate interaction, is the EFM signature for a semiconducting nanotube [57], whereas the “V-shaped” red profile, typical for a strong substrate interaction region, attests for a metallic

behavior at this region of the SWNT, and these profiles corroborate the metal-semiconducting alternating behavior of SWNT serpentine Raman spectra.

It is important to comment that we expect the strong interaction between tube and crystalline quartz substrate reported here to be related to the presence of dangling bonds in the substrate; at the temperature of nanotube growth, the surface contains exposed unpassivated Si atoms [30]. The same SWNT might behave differently if deposited on the same quartz substrate at room temperature, since the Si atoms are expected to be passivated in this case. More generally, nanotube-substrate interaction could change depending on how the system is made.

6. Substrate Interaction on Bundled and Multiwalled Tubes

Although the literature is poor on this subject, for completeness we now discuss the substrate effect on two more complex systems, which are single-wall carbon-nanotube bundles and carbon nanotubes with more than one wall.

The properties of SWNT bundles can also be affected when the bundles are deposited on a substrate, with the additional complication that the structural and electronic properties of the tubes themselves change due the tube-tube interaction [58–60]. Rao et al. [59] showed a parameterized calculation of isolated and bundled armchair nanotubes using the method of Kwon et al. [58]. They observed differences in the density of states in isolated and bundled tubes, an increase in the separation of the valence, and conduction-band singularities, which is in contrast with the results found by Reich et al. [60]. When bundled nanotubes are deposited on a substrate, the tube-tube interaction could affect the electronic changes due to the tube-substrate interplay.

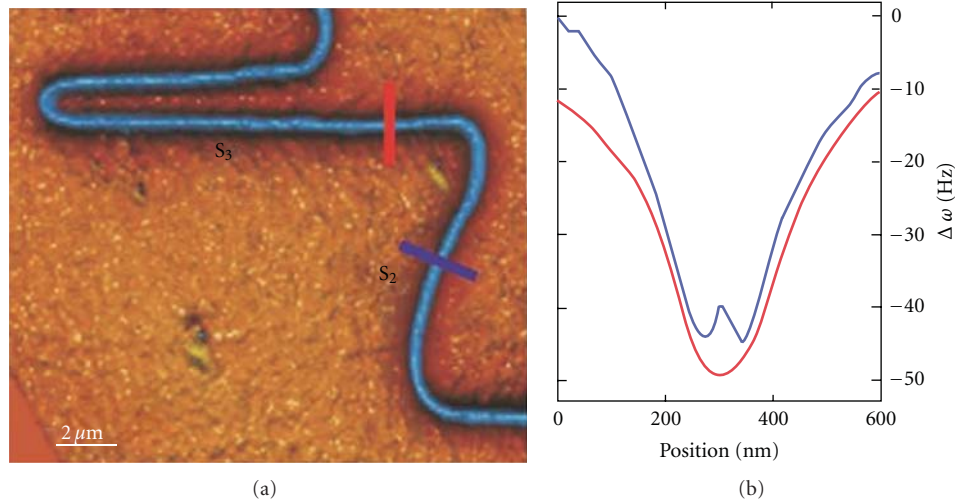


FIGURE 8: (a) Electric force microscopy (EFM) image of the same SWNT serpentine discussed in Figure 6. (b) Scanning across the SWNT, the cantilever frequency shift is different if a tube is semiconducting (“W shaped” blue line) or metallic (“V shaped” red line) [57]. The red and blue lines in (a) indicate the two regions where these profiles in (b) were acquired [30].

Considering now carbon nanotubes with more than one concentric wall (double-walled, triple-walled, or multiwalled carbon nanotubes), the higher complexity resides on the environmental effects affecting the inner and outer walls differently, summed with the tube-tube interactions. Villalpando-Paez et al. [61] showed that the (6,5) inner tubes in a double-wall carbon nanotube (DWNT) show different behavior when surrounded by different (n, m) outer tubes. The extra effect of a substrate in this case is a broad and open issue for future research.

7. Conclusions

In this paper, the importance of the substrate in carbon nanotube properties has been discussed. SWNTs are candidates for sensing applications, since interactions with the surface are the basis for sensing, while in SWNTs every carbon atom is on the surface [4]. Properties of SWNTs are affected in several ways when the local environment changes. The strong interaction between the SWNT and the substrate generates measurable modifications on the electronic and vibrational structure, providing information about nanotube properties. The strong and weak interactions between SWNT and substrate can be studied in detail using the resonance Raman process, which has been widely used for characterizing SWNTs. The crystalline substrate strongly affects the RBM frequency and resonance energies. For making the (n, m) assignments for the SWNTs on substrate, it is necessary to adjust two parameters, E_{ii} and C , in the Kataura plot. The Raman spectra G and G' bands can also be used to study nanotube-substrate interactions, including metal-semiconductor transition. The knowledge of these Raman signatures allows a detailed study of the environmental perturbations in SWNTs.

Finally, carbon nanoscience holds promise for a revolution in electronics at some point in the future [5]. New

applications for nanocarbons, such as nanotubes, appear to hold promise as we look to the future, and we expect these applications to increasingly drive applied research in SWNTs. In particular, nanotube-substrate interaction is an important issue for reaching real applications.

Acknowledgments

J. S. Soares and A. Jorio acknowledge E. Joselevich, N. Shadmi, T. S. Yarden, A. Ismach, N. Geblinger, B. R. A. Neves, A. P. M. Barboza, M. S. C. Mazzoni, N. M. Barbosa Neto, L. G. Cançado, D. Nakabayashi, P. T. Araujo, E. B. Barros, C. Vilani, M. S. Dresselhaus, G. Dresselhaus, and L. Novotny, who contributed to the development of this work. The authors also acknowledge financial support from the Rede Nacional SPM Brasil, Rede Nacional de Pesquisa em Nanotubos de Carbono, INCT em Nanoestruturas de Carbono, MCT-CNPq, and AFOSR/SOARD (Award no.FA9550-08-1-0236).

References

- [1] A. Jorio and M. S. Dresselhaus, “Nanometrology links state-of-the-art academic research and ultimate industry needs for technological innovation,” *Materials Research Society Bulletin*, vol. 32, no. 12, pp. 988–993, 2011.
- [2] A. Hirsch, *Fullerenes and Related Structures: Topics in Current Chemistry*, Springer, New York, NY, USA, 1998.
- [3] R. H. Baughman, A. A. Zakhidov, and W. A. De Heer, “Carbon nanotubes—The route toward applications,” *Science*, vol. 297, no. 5582, pp. 787–792, 2002.
- [4] A. Jorio, G. Dresselhaus, and M. S. Dresselhaus, *Carbon Nanotubes: Advanced Topics in the Synthesis, Structure, Properties and Applications*, Springer, Berlin, Germany, 2008.
- [5] P. Avouris, Z. Chen, and V. Perebeinos, “Carbon-based electronics,” *Nature Nanotechnology*, vol. 2, no. 10, pp. 605–615, 2007.

- [6] P. Avouris, M. Freitag, and V. Perebeinos, "Carbon-nanotube photonics and optoelectronics," *Nature Photonics*, vol. 2, no. 6, pp. 341–350, 2008.
- [7] M. Steiner, M. Freitag, J. C. Tsang et al., "How does the substrate affect the Raman and excited state spectra of a carbon nanotube?" *Applied Physics A*, vol. 96, no. 2, pp. 271–282, 2009.
- [8] M. S. Dresselhaus, G. Dresselhaus, R. Saito, and A. Jorio, "Raman spectroscopy of carbon nanotubes," *Physics Reports*, vol. 409, no. 2, pp. 47–99, 2005.
- [9] A. Hartschuh, H. N. Pedrosa, J. Peterson et al., "Single carbon nanotube optical spectroscopy," *ChemPhysChem*, vol. 6, no. 4, pp. 577–582, 2005.
- [10] T. Hertel, A. Hagen, V. Talalaev et al., "Spectroscopy of single- and double-wall carbon nanotubes in different environments," *Nano Letters*, vol. 5, no. 3, pp. 511–514, 2005.
- [11] Y. Zhang, J. Zhang, H. Son, J. Kong, and Z. Liu, "Substrate-induced Raman frequency variation for single-walled carbon nanotubes," *Journal of the American Chemical Society*, vol. 127, no. 49, pp. 17156–17157, 2005.
- [12] T. Hertel, R. E. Walkup, and P. Avouris, "Deformation of carbon nanotubes by surface van der Waals forces," *Physical Review B*, vol. 58, no. 20, pp. 13870–13873, 1998.
- [13] M. S. C. Mazzoni and H. Chacham, "Bandgap closure of a flattened semiconductor carbon nanotube: a first-principles study," *Applied Physics Letters*, vol. 76, no. 12, pp. 1561–1563, 2000.
- [14] W. Orellana, R. H. Miwa, and A. Fazzio, "First-principles calculations of carbon nanotubes adsorbed on Si(001)," *Physical Review Letters*, vol. 91, no. 16, pp. 1668021–1668024, 2003.
- [15] C. Jiang, J. Zhao, H. A. Therese, M. Friedrich, and A. Mews, "Raman imaging and spectroscopy of heterogeneous individual carbon nanotubes," *Journal of Physical Chemistry B*, vol. 107, no. 34, pp. 8742–8745, 2003.
- [16] V. V. Tsukruk, H. Ko, and S. Peleshanko, "Nanotube surface arrays: weaving, bending, and assembling on patterned silicon," *Physical Review Letters*, vol. 92, no. 6, pp. 655021–655024, 2004.
- [17] Y. H. Kim, M. J. Heben, and S. B. Zhang, "Nanotube wires on commensurate InAs surfaces: binding energies, band alignments, and bipolar doping by the surfaces," *Physical Review Letters*, vol. 92, no. 17, p. 176102, 2004.
- [18] A. Ismach, L. Segev, E. Wachtel, and E. Joselevich, "Carbon nanotube graphoepitaxy: highly oriented growth by faceted nanosteps," *Angewandte Chemie International Edition*, vol. 43, no. 33, pp. 11554–11555, 2004.
- [19] R. H. Miwa, W. Orellana, and A. Fazzio, "Substrate-dependent electronic properties of an armchair carbon nanotube adsorbed on H/Si(001)," *Applied Physics Letters*, vol. 86, no. 21, Article ID 213111, pp. 1–3, 2005.
- [20] S. Berber and A. Oshiyama, "Atomic and electronic structures of carbon nanotubes on Si(001) stepped surfaces," *Physical Review Letters*, vol. 96, no. 10, Article ID 105505, pp. 1–4, 2006.
- [21] G. W. Peng, A. C. H. Huan, L. Liu, and Y. P. Feng, "Structural and electronic properties of 4 Å carbon nanotubes on Si(001) surfaces," *Physical Review B*, vol. 74, no. 23, p. 235416, 2006.
- [22] P. M. Albrecht and J. W. Lyding, "Local stabilization of single-walled carbon nanotubes on Si(100)-2 × 1:H via nanoscale hydrogen desorption with an ultrahigh vacuum scanning tunnelling microscope," *Nanotechnology*, vol. 18, no. 12, Article ID 125302, 2007.
- [23] N. Geblinger, A. Ismach, and E. Joselevich, "Self-organized nanotube serpentines," *Nature Nanotechnology*, vol. 3, no. 4, pp. 195–200, 2008.
- [24] A. P. M. Barboza, A. P. Gomes, B. S. Archanjo et al., "Deformation induced semiconductor-metal transition in single wall carbon nanotubes probed by electric force microscopy," *Physical Review Letters*, vol. 100, no. 25, Article ID 256804, 2008.
- [25] Y. You, T. Yu, J. Kasim et al., "Visualization and investigation of Si-C covalent bonding of single carbon nanotube grown on silicon substrate," *Applied Physics Letters*, vol. 93, no. 10, Article ID 103111, 2008.
- [26] S. Jeon, C. Lee, J. Tang, J. Hone, and C. Nuckolis, "Growth of serpentine carbon nanotubes on quartz substrates and their electrical properties," *Nano Research*, vol. 1, pp. 427–433, 2008.
- [27] J. Huang and W. Choi, "Controlled growth and electrical characterization of bent single-walled carbon nanotubes," *Nanotechnology*, vol. 19, no. 50, Article ID 505601, 2008.
- [28] Y. Yao, X. Dai, C. Feng et al., "Crinkling ultralong carbon nanotubes into serpentines by a controlled landing process," *Advanced Materials*, vol. 21, no. 41, pp. 4158–4162, 2009.
- [29] J. Xiao, S. Dunham, P. Liu et al., "Alignment controlled growth of single-walled carbon nanotubes on quartz substrates," *Nano Letters*, vol. 9, no. 12, pp. 4311–4319, 2009.
- [30] J. S. Soares, A. P. M. Barboza, P. T. Araujo et al., "Modulating the electronic properties along carbon nanotubes via tube-substrate interaction," *Nano Letters*, vol. 10, no. 12, pp. 5043–5048, 2010.
- [31] T. Hertel, R. Martel, and P. Avouris, "Manipulation of individual carbon nanotubes and their interaction with surfaces," *Journal of Physical Chemistry B*, vol. 102, no. 6, pp. 910–915, 1998.
- [32] P. Avouris, T. Hertel, R. Martel, T. Schmidt, H. R. Shea, and R. E. Walkup, "Carbon nanotubes: nanomechanics, manipulation, and electronic devices," *Applied Surface Science*, vol. 141, no. 3–4, pp. 201–209, 1999.
- [33] M. R. Falvo, G. J. Clary, R. M. Taylor et al., "Bending and buckling of carbon nanotubes under large strain," *Nature*, vol. 389, no. 6651, pp. 582–584, 1997.
- [34] A. Jorio, M. S. Dresselhaus, R. Saito, and G. Dresselhaus, *Raman Spectroscopy in Graphene Related Systems*, Wiley-VCH, Weinheim, Germany, 2011.
- [35] A. Jorio, M. A. Pimenta, A. G. Souza Filho, R. Saito, G. Dresselhaus, and M. S. Dresselhaus, "Characterizing carbon nanotube samples with resonance Raman scattering," *New Journal of Physics*, vol. 5, pp. 139.1–139.17, 2003.
- [36] H. Son, Y. Hori, S. G. Chou et al., "Environment effects on the Raman spectra of individual single-wall carbon nanotubes: suspended and grown on polycrystalline silicon," *Applied Physics Letters*, vol. 85, no. 20, pp. 4744–4746, 2004.
- [37] Y. Zhang, H. Son, J. Zhang, M. S. Dresselhaus, J. Kong, and Z. Liu, "Raman spectra variation of partially suspended individual single-walled carbon nanotubes," *Journal of Physical Chemistry C*, vol. 111, no. 5, pp. 1983–1987, 2007.
- [38] J. C. Meyer, M. Paillet, T. Michel et al., "Raman modes of index-identified freestanding single-walled carbon nanotubes," *Physical Review Letters*, vol. 95, no. 21, Article ID 217401, pp. 1–4, 2005.
- [39] H. Kataura, Y. Kumazawa, Y. Maniwa et al., "Optical properties of single-wall carbon nanotubes," *Synthetic Metals*, vol. 103, no. 1–3, pp. 2555–2558, 1999.
- [40] P. T. Araujo, I. O. Maciel, P. B. C. Pesce et al., "Nature of the constant factor in the relation between radial breathing mode frequency and tube diameter for single-wall carbon

- nanotubes,” *Physical Review B*, vol. 77, no. 24, Article ID 241403, 2008.
- [41] J. S. Soares, L. G. Cançado, E. B. Barros, and A. Jorio, “The Kataura plot for single wall carbon nanotubes on top of crystalline quartz,” *Physica Status Solidi B*, vol. 247, no. 11-12, pp. 2835–2837, 2010.
- [42] M. S. Dresselhaus, G. Dresselhaus, and M. Hofmann, “The big picture of Raman scattering in carbon nanotubes,” *Vibrational Spectroscopy*, vol. 45, no. 2, pp. 71–81, 2007.
- [43] P. T. Araujo, S. K. Doorn, S. Kilina et al., “Third and fourth optical transitions in semiconducting carbon nanotubes,” *Physical Review Letters*, vol. 98, no. 6, Article ID 067401, 2007.
- [44] S. K. Doorn, P. T. Araujo, K. Hata, and A. Jorio, “Excitons and exciton-phonon coupling in metallic single-walled carbon nanotubes: resonance Raman spectroscopy,” *Physical Review B*, vol. 78, no. 16, Article ID 165408, 2008.
- [45] P. T. Araujo, P. B. C. Pesce, M. S. Dresselhaus, K. Sato, R. Saito, and A. Jorio, “Resonance Raman spectroscopy of the radial breathing modes in carbon nanotubes,” *Physica E*, vol. 42, no. 5, pp. 1251–1261, 2010.
- [46] L. D. Machado, S. B. Legoas, J. S. Soares et al., “On the formation of carbon nanotube serpentines: insights from multi-million atom molecular dynamics simulation,” *Materials Research Society Symposium Proceedings*, vol. 1284, pp. 79–84, 2011.
- [47] S. B. Cronin, A. K. Swan, M. S. Ünlü, B. B. Goldberg, M. S. Dresselhaus, and M. Tinkham, “Measuring the uniaxial strain of individual single-wall carbon nanotubes: resonance Raman spectra of atomic-force-microscope modified single-wall nanotubes,” *Physical Review Letters*, vol. 93, no. 16, p. 167401, 2004.
- [48] X. Duan, H. Son, B. Gao et al., “Resonant Raman spectroscopy of individual strained single-wall carbon nanotubes,” *Nano Letters*, vol. 7, no. 7, pp. 2116–2121, 2007.
- [49] B. Gao, L. Jiang, X. Ling, J. Zhang, and Z. Liu, “Chirality-dependent Raman frequency variation of single-walled carbon nanotubes under uniaxial strain,” *Journal of Physical Chemistry C*, vol. 112, no. 51, pp. 20123–20125, 2008.
- [50] A. Das, A. K. Sood, A. Govindaraj et al., “Doping in carbon nanotubes probed by Raman and transport measurements,” *Physical Review Letters*, vol. 99, no. 13, Article ID 136803, 2007.
- [51] O. Dubay, G. Kresse, and H. Kuzmany, “Phonon softening in metallic nanotubes by a Peierls-like mechanism,” *Physical Review Letters*, vol. 88, no. 23, pp. 2355061–2355064, 2002.
- [52] J. C. Tsang, M. Freitag, V. Perebeinos, J. Liu, and P. Avouris, “Doping and phonon renormalization in carbon nanotubes,” *Nature Nanotechnology*, vol. 2, no. 11, pp. 725–730, 2007.
- [53] S. Piscanec, M. Lazzeri, J. Robertson, A. C. Ferrari, and F. Mauri, “Optical phonons in carbon nanotubes: kohn anomalies, Peierls distortions, and dynamic effects,” *Physical Review B*, vol. 75, no. 3, Article ID 035427, 2007.
- [54] I. O. Maclel, N. Anderson, M. A. Pimenta et al., “Electron and phonon renormalization near charged defects in carbon nanotubes,” *Nature Materials*, vol. 7, no. 11, pp. 878–883, 2008.
- [55] J. S. Soares, E. B. Barros, N. Shadmi, E. Joselevich, and A. Jorio, “Raman study of nanotube-substrate interaction using single-wall carbon nanotubes grown on crystalline quartz,” *Physica Status Solidi B*, vol. 248, no. 11, pp. 2536–2539, 2011.
- [56] M. S. Dresselhaus, G. Dresselhaus, A. Jorio, A. G. Souza Filho, G. G. Samsonidze, and R. Saito, “Science and applications of single-nanotube Raman spectroscopy,” *Journal of Nanoscience and Nanotechnology*, vol. 3, no. 1-2, pp. 19–37, 2003.
- [57] A. P. M. Barboza, A. P. Gomes, H. Chacham, and B. R. A. Neves, “Probing electric characteristics and sorting out metallic from semiconducting carbon nanotubes,” *Carbon*, vol. 48, no. 11, pp. 3287–3292, 2010.
- [58] Y. K. Kwon, S. Saito, and D. Tománek, “Effect of intertube coupling on the electronic structure of carbon nanotube ropes,” *Physical Review B*, vol. 58, no. 20, pp. R13314–R13317, 1998.
- [59] A. M. Rao, J. Chen, E. Richter et al., “Effect of van der Waals interactions on the Raman modes in single walled carbon nanotubes,” *Physical Review Letters*, vol. 86, no. 17, pp. 3895–3898, 2001.
- [60] S. Reich, C. Thomsen, and P. Ordejón, “Electronic band structure of isolated and bundled carbon nanotubes,” *Physical Review B*, vol. 65, no. 15, p. 1554111, 2002.
- [61] F. Villalpando-Paez, H. Muramatsu, Y. A. Kim et al., “Wall-to-wall stress induced in (6,5) semiconducting nanotubes by encapsulation in metallic outer tubes of different diameters: a resonance Raman study of individual C60-derived double-wall carbon nanotubes,” *Nanoscale*, vol. 2, no. 3, pp. 406–411, 2010.

Research Article

Synthesis of Nickel-Encapsulated Carbon Nanocapsules and Cup-Stacked-Type Carbon Nanotubes via Nickel-Doped Fullerene Nanowhiskers

Tokushi Kizuka,¹ Kun'ichi Miyazawa,² and Akira Akagawa¹

¹ Institute of Materials Science, Graduate School of Pure and Applied Sciences, University of Tsukuba, Tsukuba, Ibaraki 305-8753, Japan

² Fullerene Engineering Group, Materials Processing Unit, National Institute for Materials Science, Namiki, Tsukuba, Ibaraki 305-0044, Japan

Correspondence should be addressed to Tokushi Kizuka, kizuka@ims.tsukuba.ac.jp

Received 12 July 2011; Revised 25 September 2011; Accepted 26 September 2011

Academic Editor: Zheng Hu

Copyright © 2012 Tokushi Kizuka et al. This is an open access article distributed under the Creative Commons Attribution License, which permits unrestricted use, distribution, and reproduction in any medium, provided the original work is properly cited.

Nickel- (Ni) doped C₆₀ nanowhiskers (NWs) were synthesized by a liquid-liquid interfacial precipitation method using a C₆₀-saturated toluene solution and isopropanol with Ni nitrate hexahydrate Ni(NO₃)₂·6H₂O. By varying the heating temperature of Ni-doped C₆₀ NWs, two types of one-dimensional carbon nanostructures were produced. By heating the NWs at 973 and 1173 K, carbon nanocapsules (CNCs) that encapsulated Ni nanoparticles were produced. The Ni-encapsulated CNCs joined one dimensionally to form chain structures. Upon heating the NWs to 1373 K, cup-stacked-type carbon nanotubes were synthesized.

1. Introduction

Crystals of fullerene molecules have been synthesized by precipitation methods [1–13]. Such fullerene crystals show various morphologies, that is, plates, films, and rods, and the morphology can be controlled by varying the precipitation conditions. By using a liquid-liquid interfacial precipitation (LLIP) method, Miyazawa et al. have produced fullerene nanowhiskers (NWs) and nanotubes with high length-to-diameter aspect ratios [14–17]. By heating fullerene NWs, carbon nanocapsules (CNCs) are produced [18–22]. Using the LLIP method, Miyazawa et al. also found that fullerene NWs incorporate metal nanoparticles using C₆₀ derivatives or metal nitrate hydrates in solutions [23–26]. It is expected that the alloying of metals and CNCs can be performed using metal-doped fullerene NWs. In this study, metal-CNC structures were produced by the heating nickel- (Ni) doped C₆₀ NWs which were synthesized by the LLIP method.

2. Method

C₆₀ powders were dissolved in toluene to prepare a C₆₀-saturated solution with a solubility of 2.8 g/L. Ni nitrate

hexahydrate [Ni(NO₃)₂·6H₂O] was dissolved in 2-propanol with concentrations of 0.01 M and 0.68 M (hereafter labeled as specimens A and B, resp.). The C₆₀ toluene solution was poured into a glass vial, and the 2-propanol was then added to form a liquid-liquid interface. After the vial was maintained at 278 K for one week, the solution was filtered to extract precipitates. The precipitates were dried and heated in high vacuum at 973, 1173, and 1323 K for 1 h. Next, the specimens were dispersed on microgrids and observed by transmission electron microscopy (TEM). Thermogravimetric analyses (TGA) and differential thermal analyses (DTA) of the specimens were performed in a nitrogen flow.

3. Results and Discussion

Figure 1(a) shows a bright-field image of an as-precipitated Ni-doped C₆₀ NW in specimen A. The diameter of this NW is 740 nm. The surfaces of the Ni-doped NWs were porous, as shown in Figure 1(b). Figure 2(a) shows a bright-field image of an as-precipitated Ni-doped C₆₀ NW in specimen B. The diameter of this NW is 240 nm. The NWs showed undulating surfaces. Ni particles with a face-centered

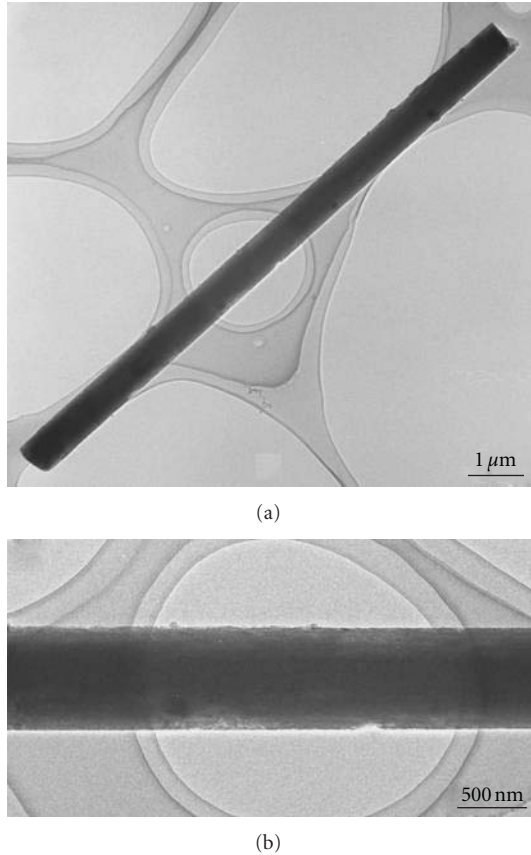


FIGURE 1: (a) Bright-field image of Ni-doped C_{60} nanowhiskers synthesized using isopropyl alcohol with concentration of 0.01 M $Ni(NO_3)_2 \cdot 6H_2O$. (b) Enlarged image of (a).

cubic structure were observed in the NWs, as shown in Figure 2(b).

The surfaces of the Ni-doped NWs in both specimens A and B were rough. The roughness increases with the $Ni(NO_3)_2 \cdot 6H_2O$ concentration. Pure C_{60} NWs are surrounded by planar surfaces [14–17]. Thus, we attribute the rough surfaces of the as-precipitated Ni-doped NWs to the addition of $Ni(NO_3)_2 \cdot 6H_2O$ in 2-propanol. In particular, Ni particles were observed in the dents of Ni-doped NWs, implying that the crystal growth of the NWs was inhibited by the Ni particles. This is similar to the crystal growth of C_{60} -derivative NWs [23–25].

Figure 3 shows TGA and DTA curves of the Ni-doped NWs in specimen A and C_{60} bulk crystals. For C_{60} bulk crystals, the DTA curve starts to decrease around 773 K. On the other hand, no change is observed in the TGA curve around this temperature. This shows that the mass of the specimen remained unchanged, whereas the structure changed. The transformation from a crystalline to an amorphous configuration of C_{60} molecules starts at this temperature [27]. Around 1173 K, the TGA curve decreases, and a downward peak is observed in the DTA curve, which shows that an endothermic reaction occurred. Furthermore, it has been reported that sublimation of C_{60} molecules takes place at this temperature [27]. On the other hand,

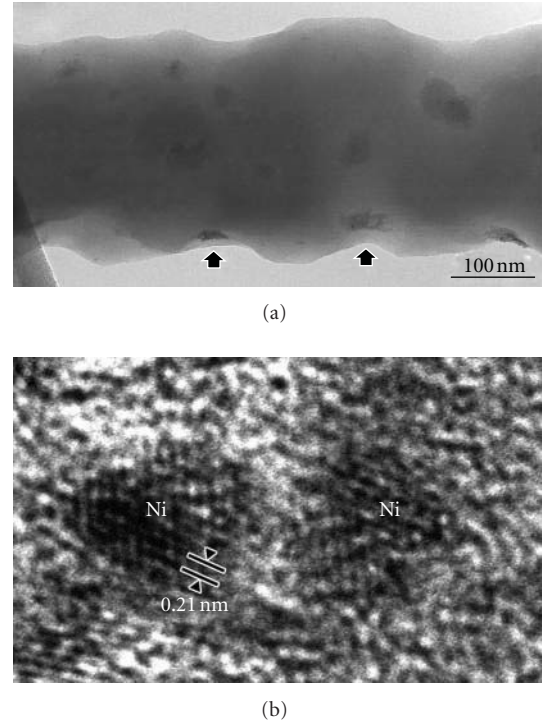


FIGURE 2: (a) Bright-field images of Ni-doped C_{60} nanowhiskers synthesized using isopropyl alcohol with concentration of 0.68 M $Ni(NO_3)_2 \cdot 6H_2O$. The arrows indicate Ni particles in dents. (b) High-resolution image of Ni particles in the NW in (a).

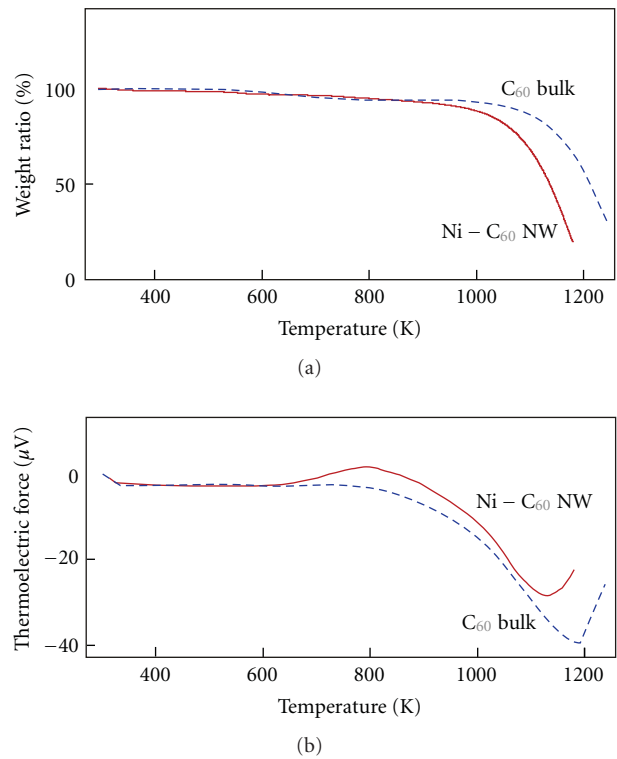
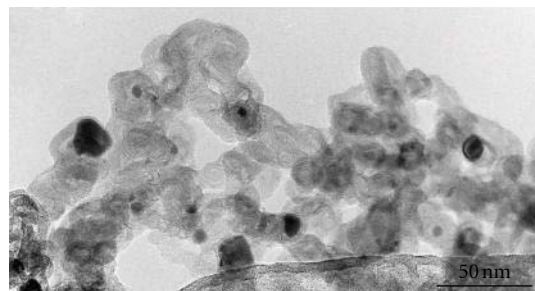
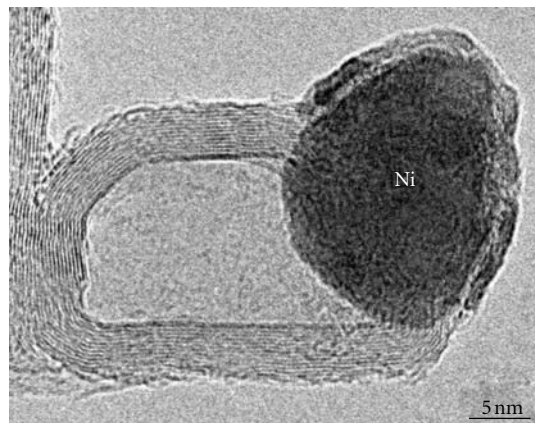


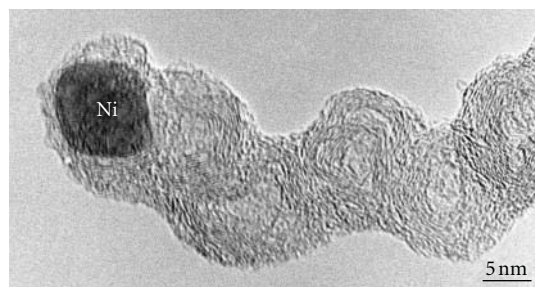
FIGURE 3: (a) Thermogravimetric analysis curves and (b) differential thermal analysis curves of Ni-doped nanowhiskers (specimen A, solid lines) and pure C_{60} bulk (broken lines) in nitrogen flow.



(a)



(b)

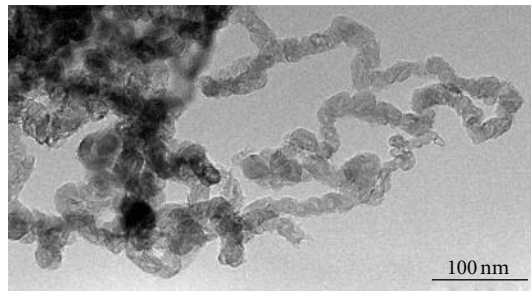


(c)

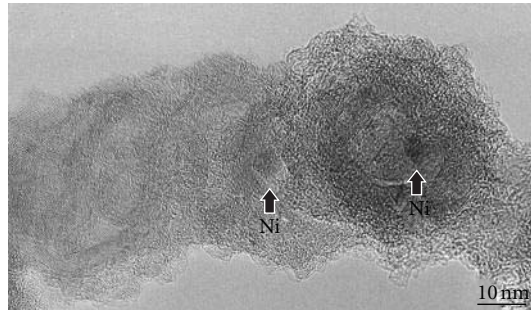
FIGURE 4: (a) Bright-field images of Ni-encapsulated carbon nanocapsules prepared by heating Ni-doped C_{60} nanowhiskers (specimen A) at 973 K. (b) High-resolution image of Ni-encapsulated carbon nanocapsule. (c) High-resolution image of chain of Ni-encapsulated carbon nanocapsules.

for the Ni-doped NWs, an upward peak was observed in the DTA curve around 773 K, which corresponds to an exothermic reaction. No change is observed in the TGA curve around this temperature. TEM observations showed that grain coarsening of Ni particles started near this temperature. This TEM result suggests that the upward peak around 773 K was caused by the grain coarsening of Ni particles.

Around 1123 K, the TGA curve decreases and the DTA curve shows a downward peak. This implies that the sublimation of C_{60} molecules occurred, as similarly observed in C_{60} bulk crystals. Note that the sublimation temperature of C_{60} molecules in the Ni-doped NWs is approximately 50 K lower than that in the C_{60} bulk crystals. From this result, we



(a)



(b)

FIGURE 5: (a) Bright-field images of Ni-encapsulated carbon nanocapsules prepared by heating Ni-doped C_{60} nanowhiskers (specimen B) at 1173 K. The nanocapsules form chain structures. (b) High-resolution image of the chain of Ni-encapsulated carbon nanocapsules.

infer that Ni particles act as catalysts for the weakening of intermolecular C_{60} molecular bonds.

On the basis of the results of TGA and DTA, we heated the specimens to temperatures higher than 973 K and observed them by TEM. Figures 4(a) and 4(b) show bright-field and high-resolution images of specimen A after heating at 973 K, respectively. Ni-encapsulated CNCs are formed by this heat treatment. The diameter of the CNCs ranged from 12 to 51 nm. The diameter of the encapsulated Ni particles ranged from 8 to 33 nm. A portion of the CNCs aligned one dimensionally to form chain structures, as shown in Figure 4(c). Such chain structures have also been produced by arc discharge [28, 29]. As shown in Figure 4(b), Ni particles were attached on the tips of the chains, indicating that the chain structures were produced by the cycles of the precipitation of graphene shells around Ni particles and the movement of the Ni particles. Note that in Figure 4(b), the Ni particle protrudes from the center of the hollow region of the CNC. This state corresponds to the movement of the Ni particle from the precipitated graphene shell.

Figures 5(a) and 5(b) show bright-field and high-resolution images of specimen B after heating it at 1173 K. Ni-encapsulated CNCs and their chain structures were formed. The formation rate of CNC chains in this specimen was higher than that in specimen A owing to a higher concentration of Ni particles.

By heating Ni-doped C_{60} NWs in specimen B to 1323 K, cup-stacked-type carbon nanotubes (CNTs) were produced, as shown in Figure 6. Ni particles were attached to the tip

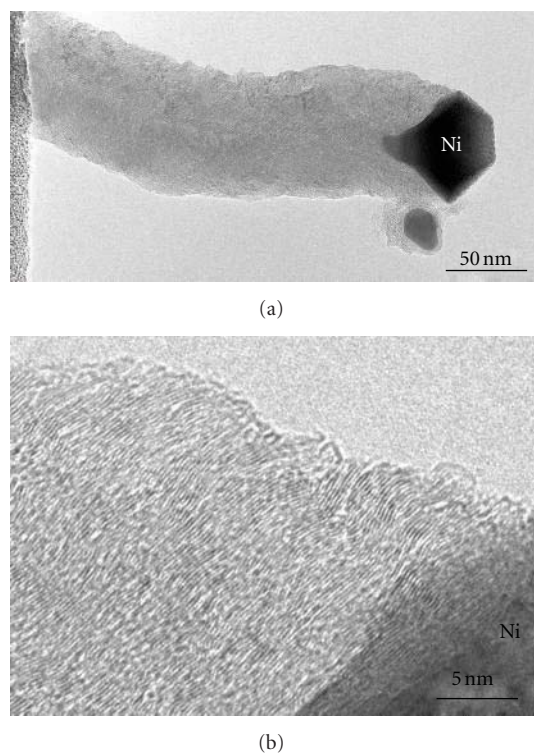


FIGURE 6: (a) Cup-stacked-type carbon nanotube synthesized by heating Ni-doped C_{60} nanowhiskers (specimen B) at 1323 K. (b) High-resolution image of the cup-stacked-type carbon nanotube depicted in (a).

of CNTs, and the graphene layers were aligned parallel to the surfaces of Ni particles. Thus, CNTs were produced by the continuous precipitation of graphene cones and the continuous movement of Ni particles. However, for CNC formation, the movement of Ni particles and the precipitation of graphene shells are intermittent.

In this experiment, cup-stacked-type CNTs were produced at the highest temperature (1373 K). As observed in Figures 4(b) and 5(a), the Ni particles in the specimens heated at temperatures lower than 1173 K formed spherical shapes, whereas Ni particles in the specimens heated to 1373 K formed clear crystal habits. At higher temperatures, the metal particles show more stable shapes surrounded by crystal planes with lower surface energies. Cup-stacked-type CNTs are formed by one-directional continuous precipitation of graphitic cones from metal particles having such clear crystal habits [30–39]. The solubility limit of carbon atoms in metals also increases at higher temperatures, and the precipitation speed increases. We infer that both the formation of crystal habits and the increase in precipitation speed promote the production of cup-stacked-type CNTs.

4. Conclusion

Ni-doped C_{60} NWs synthesized by the liquid-liquid interfacial precipitation method allow us to produce Ni-encapsulated CNCs and cup-stacked-type CNTs. In particular, the CNCs form chain structures. The two types of

one-dimensional carbon nanostructures were produced using Ni-doped C_{60} NWs by varying heating temperature.

Other transition metals such as iron and cobalt can be doped into fullerene NWs using similar synthetic methods, and CNCs encapsulating nanoparticles of various metal elements can be produced using NWs.

Acknowledgment

This study was partly supported by Grants-in-Aid from the Ministry of Education, Culture, Sport, Science, and Technology, Japan (nos. 22310065 and 23651127).

References

- [1] W. Krätschmer, L. D. Lamb, K. Fostiropoulos, and D. R. Huffman, "Solid C_{60} : a new form of carbon," *Nature*, vol. 347, no. 6291, pp. 354–358, 1990.
- [2] W. I. F. David, R. M. Ibberson, J. C. Matthewman et al., "Crystal structure and bonding of ordered C_{60} ," *Nature*, vol. 353, no. 6340, pp. 147–149, 1991.
- [3] S. J. Duclos, K. Brister, R. C. Haddon, A. R. Kortan, and F. A. Thiel, "Effects of pressure and stress on C_{60} fullerite to 20 GPa," *Nature*, vol. 351, no. 6325, pp. 380–382, 1991.
- [4] P. A. Heiney, J. E. Fischer, A. R. McGhie et al., "Orientational ordering transition in solid C_{60} ," *Physical Review Letters*, vol. 66, no. 22, pp. 2911–2914, 1991.
- [5] R. L. Meng, D. Ramirez, X. Jiang et al., "Growth of large, defect-free pure C_{60} single crystals," *Applied Physics Letters*, vol. 59, no. 26, pp. 3402–3403, 1991.
- [6] W. Krakow, N. M. Rivera, R. A. Roy, R. S. Ruoff, and J. J. Cuomo, "Epitaxial growth of C_{60} thin films on mica," *Journal of Materials Research*, vol. 7, no. 4, pp. 784–787, 1992.
- [7] X. D. Shi, A. R. Kortan, J. M. Williams, A. M. Kini, B. M. Savall, and P. M. Chaikin, "Sound velocity and attenuation in single-crystal C_{60} ," *Physical Review Letters*, vol. 68, no. 6, pp. 827–830, 1992.
- [8] Y. Yosida, "Scanning electron microscope images of C_{60} whiskers," *Japanese Journal of Applied Physics, Part 2*, vol. 31, no. 4, pp. L505–L507, 1992.
- [9] M. Haluška, H. Kuzmany, M. Vybornov, P. Rogl, and P. Fejdi, "A double-temperature-gradient technique for the growth of single-crystal fullerites from the vapor phase," *Applied Physics A*, vol. 56, no. 3, pp. 161–167, 1993.
- [10] J. Z. Liu, J. W. Dykes, M. D. Lan, P. Klavins, R. N. Shelton, and M. M. Olmstead, "Vapor transport growth of C_{60} crystals," *Applied Physics Letters*, vol. 62, no. 5, pp. 531–532, 1993.
- [11] J. L. de Boer, S. van Smaalen, V. Petricek, M. Dusek, P. M. A. Verheijen, and G. Meijer, "Hexagonal close-packed C_{60} ," *Chemical Physics Letters*, vol. 219, no. 5-6, pp. 469–472, 1994.
- [12] F. Michaud, M. Barrio, S. Toscani et al., "Solid-state studies on single and decagonal crystals of C_{60} grown from 1,2-dichloroethane," *Physical Review B*, vol. 57, no. 17, pp. 10351–10358, 1998.
- [13] S. Toscani, H. Allouchi, J. L. Tamarit et al., "Decagonal C_{60} crystals grown from n-hexane solutions: solid-state and aging studies," *Chemical Physics Letters*, vol. 330, no. 5-6, pp. 491–496, 2000.
- [14] K. Miyazawa, A. Obayashi, and M. Kuwabara, " C_{60} nanowhiskers in a mixture of lead zirconate titanate sol- C_{60} toluene solution," *Journal of the American Ceramic Society*, vol. 84, no. 3–12, pp. 3037–3039, 2001.
- [15] K. Miyazawa, " C_{70} nanowhiskers fabricated by forming liquid/liquid interfaces in the systems of toluene solution of

- C_{70} and isopropyl/alcohol," *Journal of the American Ceramic Society*, vol. 85, no. 5, pp. 1297–1299, 2002.
- [16] K. Miyazawa, Y. Kuwasaki, A. Obayashi, and M. Kuwabara, "C₆₀ nanowhiskers formed by the liquid-liquid interfacial precipitation method," *Journal of Materials Research*, vol. 17, no. 1, pp. 83–88, 2002.
- [17] K. Miyazawa, K. Hamamoto, S. Nagata, and T. Suga, "Structural investigation of the C₆₀/C₇₀ whiskers fabricated by forming liquid-liquid interfaces of toluene with dissolved C₆₀/C₇₀ and isopropyl alcohol," *Journal of Materials Research*, vol. 18, no. 5, pp. 1096–1103, 2003.
- [18] K. Asaka, R. Kato, Y. Maezono, R. Yoshizaki, K. Miyazawa, and T. Kizuka, "Light-emitting filaments composed of nanometer-sized carbon hollow capsules," *Applied Physics Letters*, vol. 88, no. 5, Article ID 051914, pp. 1–3, 2006.
- [19] K. Asaka, R. Kato, K. Miyazawa, and T. Kizuka, "Deformation of multiwalled nanometer-sized carbon capsules," *Applied Physics Letters*, vol. 89, no. 19, Article ID 191914, 2006.
- [20] K. Asaka, R. Kato, R. Yoshizaki, K. Miyazawa, and T. Kizuka, "Conductance of carbon nanocapsule junctions," *Physical Review B*, vol. 76, no. 11, Article ID 113404, 2007.
- [21] T. Kizuka, R. Kato, and K. Miyazawa, "Structure of hollow carbon nanocapsules synthesized by resistive heating," *Carbon*, vol. 47, no. 1, pp. 138–144, 2009.
- [22] T. Kizuka, R. Kato, and K. Miyazawa, "Surface breakdown dynamics of carbon nanocapsules," *Nanotechnology*, vol. 20, no. 10, Article ID 105205, 2009.
- [23] K. Miyazawa, T. Mashino, and T. Suga, "Structural characterization of the C₆₀[C(COOC₂H₅)₂] whiskers prepared by the liquid-liquid interfacial precipitation method," *Journal of Materials Research*, vol. 18, no. 11, pp. 2730–2735, 2003.
- [24] K. Miyazawa and T. Suga, "Transmission electron microscopy investigation of fullerene nanowhiskers and needle-like precipitates formed by using C₆₀ and (η^2 -C₆₀)/Pt(PPh₃)₂," *Journal of Materials Research*, vol. 19, no. 8, pp. 2410–2414, 2004.
- [25] K. Miyazawa and T. Suga, "Transmission electron microscopy investigation of tubular and capsular needlelike crystals of C₆₀ produced by the liquid-liquid interfacial precipitation method," *Journal of Materials Research*, vol. 19, no. 11, pp. 3145–3148, 2004.
- [26] M. Sathish, K. Miyazawa, and T. Sasaki, "Preparation and characterization of Ni incorporated fullerene nanowhiskers," *Diamond and Related Materials*, vol. 17, no. 4-5, pp. 571–575, 2008.
- [27] V. Z. Mordkovich, A. G. Umnov, T. Inoshita, and M. Endo, "Observation of multiwall fullerenes in thermally treated laser pyrolysis carbon blacks," *Carbon*, vol. 37, no. 11, pp. 1855–1858, 1999.
- [28] Y. Saito, T. Yoshikawa, M. Okuda et al., "Carbon nanocapsules encasing metals and carbides," *Journal of Physics and Chemistry of Solids*, vol. 54, no. 12, pp. 1849–1860, 1993.
- [29] Y. Saito, "Nanoparticles and filled nanocapsules," *Carbon*, vol. 33, no. 7, pp. 979–988, 1995.
- [30] A. T. Balaban, D. J. Klein, and X. Liu, "Graphitic cones," *Carbon*, vol. 32, no. 2, pp. 357–359, 1994.
- [31] H. Terrones, "Curved graphite and its mathematical transformations," *Journal of Mathematical Chemistry*, vol. 15, no. 1, pp. 143–156, 1994.
- [32] H. Terrones, T. Hayashi, M. Muñoz-Navia et al., "Graphitic cones in palladium catalysed carbon nanofibres," *Chemical Physics Letters*, vol. 343, no. 3-4, pp. 241–250, 2001.
- [33] B. O. Boskovic, V. Stolojan, R. U. A. Khan, S. Haq, and S. R. P. Silva, "Large-area synthesis of carbon nanofibres at room temperature," *Nature Materials*, vol. 1, no. 3, pp. 165–168, 2002.
- [34] M. Endo, Y. A. Kim, T. Hayashi et al., "Structural characterization of cup-stacked-type nanofibers with an entirely hollow core," *Applied Physics Letters*, vol. 80, no. 7, pp. 1267–1269, 2002.
- [35] Y. A. Kim, T. Hayashi, Y. Fukai, M. Endo, T. Yanagisawa, and M. S. Dresselhaus, "Effect of ball milling on morphology of cup-stacked carbon nanotubes," *Chemical Physics Letters*, vol. 355, no. 3-4, pp. 279–284, 2002.
- [36] M. Endo, Y. A. Kim, M. Ezaka et al., "Selective and efficient impregnation of metal nanoparticles on cup-stacked-type carbon nanofibers," *Nano Letters*, vol. 3, no. 6, pp. 723–726, 2003.
- [37] C. Kim, Y. J. Kim, Y. A. Kim et al., "High performance of cup-stacked-type carbon nanotubes as a Pt-Ru catalyst support for fuel cell applications," *Journal of Applied Physics*, vol. 96, no. 10, pp. 5903–5905, 2004.
- [38] K. Saito, M. Ohtani, and S. Fukuzumi, "Electron-transfer reduction of cup-stacked carbon nanotubes affording cup-shaped carbons with controlled diameter and size," *Journal of the American Chemical Society*, vol. 128, no. 44, pp. 14216–14217, 2006.
- [39] Q. Liu, W. Ren, Z. G. Chen et al., "Semiconducting properties of cup-stacked carbon nanotubes," *Carbon*, vol. 47, no. 3, pp. 731–736, 2009.

Research Article

Thickness Effect on F8T2/C₆₀ Bilayer Photovoltaic Devices

Natasha A. D. Yamamoto, Andreia G. Macedo, and Lucimara S. Roman

Grupo de Dispositivos Nanoestruturados, Departamento de Física, Universidade Federal do Paraná, 8153-990 Curitiba, PR, Brazil

Correspondence should be addressed to Lucimara S. Roman, lsroman@fisica.ufpr.br

Received 15 July 2011; Accepted 3 September 2011

Academic Editor: Kun'ichi Miyazawa

Copyright © 2012 Natasha A. D. Yamamoto et al. This is an open access article distributed under the Creative Commons Attribution License, which permits unrestricted use, distribution, and reproduction in any medium, provided the original work is properly cited.

Copolymers based on fluorene-thiophene units have presented promising efficiencies in photovoltaic devices applications. They present good transport properties mainly after thermal treatment of the polymer films. Here, we investigate the properties of bilayer devices formed by the heterojunction of the polymer F8T2 with variable thickness and the fullerene. The series resistance of the equivalent circuit associated with the device increases as the polymer film gets thicker. The current-voltage characteristics of the bilayer devices follow the Mott-Gurney law of SCLC. For the best performing device we measured 2.1% of power conversion efficiency.

1. Introduction

Fluorene-thiophene-conjugated copolymers have been extensively investigated and used in the field of organic electronics [1, 2]. The main applications are organic photovoltaic cells (PVs) [3–10], organic light-emitting diodes (OLEDs) [11], and field effect transistors (FETs) [12]. These copolymers have high absorption coefficient in the visible wavelength range; high quantum yields values and high charge mobility. Additionally, the incorporation of carbon-based materials, such as carbon nanotubes [9], fullerenes or its derivatives [13–15] brought interesting effects in organic PV cells built in bulk heterojunction (BHJ) or layered geometry. These carbon compounds have high electron affinity relatively to the conjugated polymers; in this way, they act as electron acceptor materials favoring the exciton dissociation prior the radiative/nonradiative recombinations, thus the charge collection through the electrodes.

This combination has resulted in high power conversion efficiencies (η). For instance, BHJ cell based on poly(9,9'-dihexylfluorene-alt-thiophene) polymer (PFT1) and PCBM displayed open circuit voltage (V_{oc}) of 0.77 V and η of 0.62% [3], while using poly(9,9'-dihexylfluorene-alt-bithiophene) (F6T2) or poly[9,9'-dioctyl-fluorene-cobithiophene] (F8T2) displayed V_{oc} around 1 V, η of 2.7% [4] or

2.13% [5, 6], respectively. These results were both attributed to the high hole mobility and absorption coefficient in these polymers with efficient photocurrent generation. A bilayer solar cell prepared with F8T2 but different fullerene C₇₀ displayed the highest η of 3.4%, after thermal annealing at 200°C [7]. The increase in η in this device was attributed to a better chain organization and higher roughness of the film, achieving higher donor-acceptor heterojunction area for exciton dissociation. Recently, we reported a bilayer PV cell prepared with poly[9,9'-hexyl-fluorene-alt-bithiophene] and fullerene (C₆₀) displaying an increase of η from 0.4 to 2.8% after annealing at 200°C. Comparing these results and the behavior of the current versus voltage characteristics, we concluded that the π - π stacking in solid state is enhanced after thermal annealing with a reduction of traps and thus reflecting higher hole mobility in this polymer after annealing [8].

Herein, we report the studies of bilayer devices formed by the heterojunction of the polymer F8T2 with variable thickness (18 up to 60 nm) and the fullerene C₆₀ sandwiched between two electrodes: FTO/PEDOT:PSS as the anode and aluminium as the cathode. The transport properties of the devices follow the Mott-Gurney law of space charge law current (SCLC).

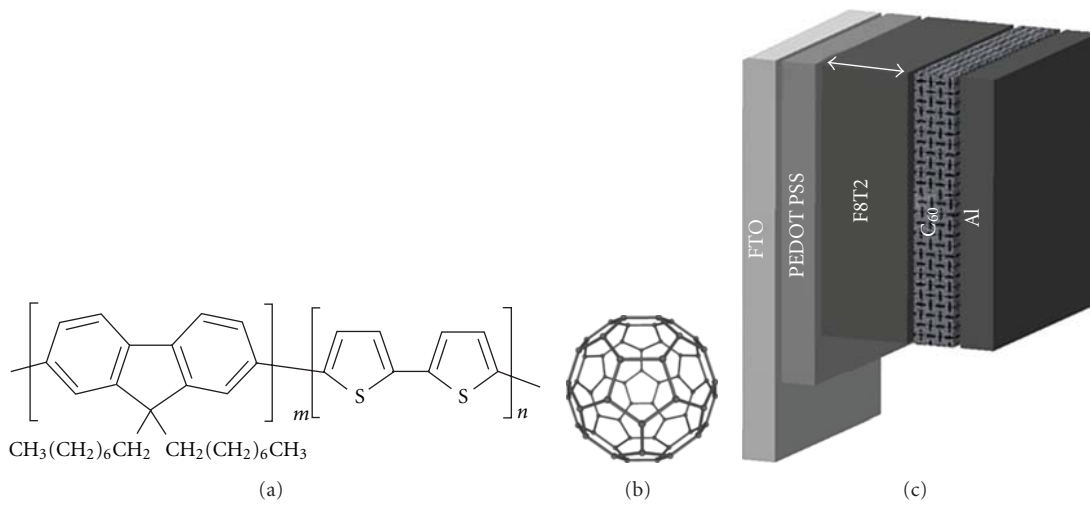


FIGURE 1: Molecular structures of the active materials: (a) structure of F8T2 polymer, (b) fullerene C_{60} , and (c) bilayer device structure: FTO/PEDOT : PSS/F8T2/ C_{60} /Al with variable thickness of the F8T2 layer.

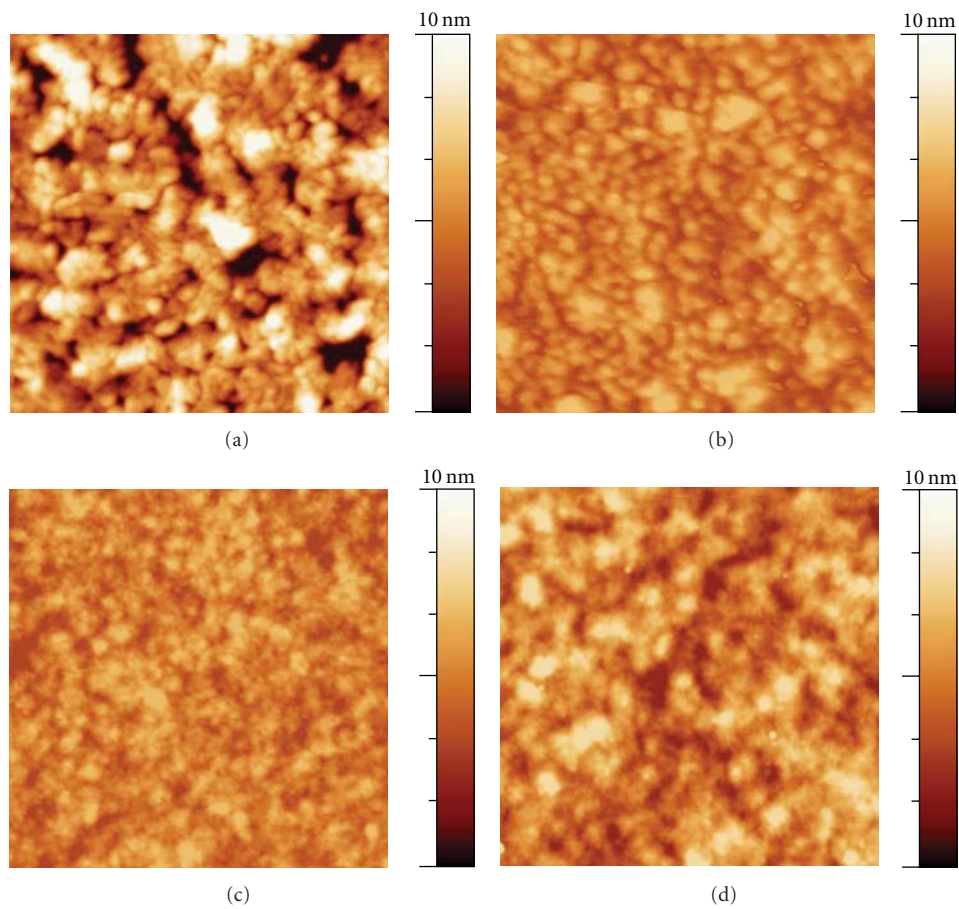


FIGURE 2: AFM height images of F8T2 polymer films coated on glass substrates for each thickness: (a) 18 nm, (b) 30 nm, (c) 40 nm, and (d) 60 nm. The scan size is $1.5 \mu\text{m} \times 1.5 \mu\text{m}$.

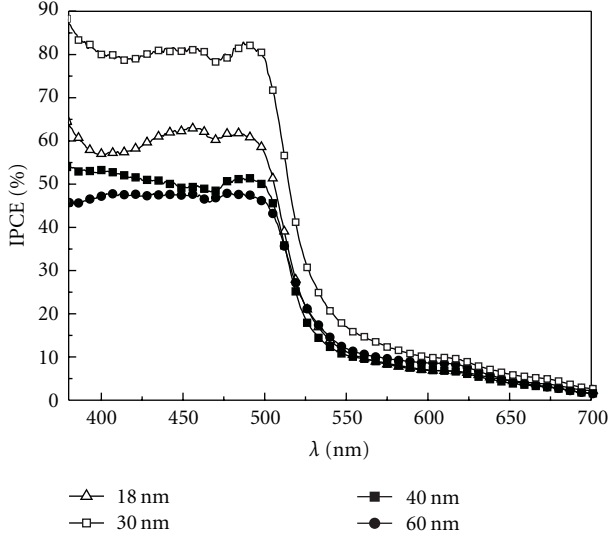


FIGURE 3: External quantum efficiency for the FTO/PEDOT:PSS/F8T2/C₆₀/Al devices with different thickness of the F8T2 layer.

2. Experimental

Poly(9,9-dioctylfluorene-*alt*-bithiophene) (F8T2) polymer with number average molecular weight (M_n) $>20,000 \text{ gmol}^{-1}$ was purchased from Aldrich. The devices were fabricated as follows: poly(3,4-ethylenedioxythiophene)-polystyrene sulfonic acid (PEDOT:PSS) was filtered in a $0.45 \mu\text{m}$ filter, then a film with thickness of 40 nm was spin coated at 6000 rpm onto the cleaned fluorine-tin-oxide (FTO-, $5\text{--}10 \Omega$) [16] patterned glass substrate and annealed at 100°C by 15 min in air. F8T2 polymer film was spin coated from chlorobenzene solutions with concentrations of $3\text{--}7.5 \text{ mgmL}^{-1}$ and treated at 100°C by 15 min (in vacuum). These parameters were set in order to obtain active layer thickness ranging from 18 to 60 nm. Then, 30 nm of C₆₀ and 100 nm of Al were thermally evaporated through a shadow mask at vacuum pressure of 6×10^{-6} mbar, respectively. Subsequently, the FTO/PEDOT:PSS/F8T2/C₆₀/Al were encapsulated upon nitrogen atmosphere. The F8T2 and C₆₀ molecular structures as well as the device structure are depicted in Figure 1.

The polymer films thickness was determined in a Dektak 3 profilometer. Topography images were acquired by using an atomic force microscope (AFM, Shimadzu SPM 9500J3) in dynamic mode. The photovoltaic characterization was performed with a Keithley picoammeter with power supply, model 6487 and a monochromator/spectrometer (1/4 m Ori-el). The solar simulation was made using air mass (AM1.5) filter with a power illumination of 100 mWcm^{-2} from a 150 W Oriel Xenon lamp.

3. Results and Discussion

F8T2 films were analyzed by AFM as illustrated in Figures 2(a)–2(d). Similar morphology is observed by varying the thickness from 18 up to 60 nm, however the film with 18 nm has root-mean-square (rms) roughness equal to 1.2 nm, and this value is slightly higher in comparison with thicker films

TABLE 1: Device characteristics of the bilayer solar cells.

Active layer thickness (nm)	J_{sc} (mA cm^{-2})	V_{oc} (V)	FF (%)	η (%)
18	3.84	0.75	54	1.60
30	4.79	0.91	50	2.10
40	3.65	0.85	50	1.55
60	1.97	0.65	34	0.43

that display roughness below 1 nm. This may arise due to the roughness related with the FTO substrate; PEDOT:PSS and thicker polymer films cover more efficiently the valleys and hills observed in polycrystalline FTO films.

The photovoltaic devices were characterized by their spectral response and their current density versus voltage curves under AM 1.5 illumination of 100 mW cm^{-2} . The spectral response is expressed by the external quantum efficiency (IPCE) which is the ratio of the photocurrent to incoming photons flux: $\text{IPCE} = 1240 J_{ph}/\lambda I_0$, where J_{ph} is the photocurrent density (Acm^{-2}), I_0 is the light intensity (Wm^{-2}), and λ is the wavelength (nm) [17]. Figure 3 shows the spectral response of FTO/PEDOT:PSS/F8T2/C₆₀/Al devices for different active layer thickness: 18, 30, 40, and 60 nm. The external quantum efficiency spectra of the devices follow the absorption coefficient ($\alpha = 4\pi k/\lambda$) dependence on wavelength of F8T2 [5, 18] and C₆₀, reflecting the contribution of the polymer and the molecule to the photocurrent [19]. The light harvesting contribution of F8T2 can be observed in the wavelength range from 400 to 500 nm. The comparison of the action spectra for each thickness shows that the photoconversion efficiency is higher for the device with active layer of 30 nm: the maximum IPCE value is around 80% under monochromatic illumination of $\lambda = 450 \text{ nm}$. Devices with thicker F8T2 layer presented maximum IPCE around 50%. It is well known that although thicker layers can absorb more light, the light intensity at the interface is smaller, thus the exciton dissociation in the F8T2/C₆₀ device [20, 21].

The electrical characteristics under illumination of AM1.5 radiation of 100 mWcm^{-2} are shown in Figure 4, and the photovoltaic parameters obtained from these curves are summarized in Table 1. The device performance dependence on F8T2 thickness corroborates with the external quantum efficiency results. The 30 nm F8T2 layer exhibits a short-circuit current (J_{sc}) of 4.79 mAcm^{-2} , V_{oc} of 0.91 V, a fill factor of 50% and of 2.1%. Bilayer devices based on F8T2/C₇₀ which were prepared by using trichlorobenzene as solvent and annealed at 100°C , displayed $\eta = 1.2\%$ as it was previously reported by Kekuda et al. [7]. Devices with F8T2 thickness of 60 nm presented poor photovoltaic performance. It is well known that devices based on thick active layers have the efficiency compromised by the transport due to higher resistance of the layer, as it can be clearly seen in Figure 4. In Figure 4 is also presented an equivalent circuit for photovoltaic device under illumination considered as a current source with a diode in parallel. We calculate the series resistance R_s of equivalent circuit associated with the solar cells by using the modified method for IEC 60891 following Kunz and

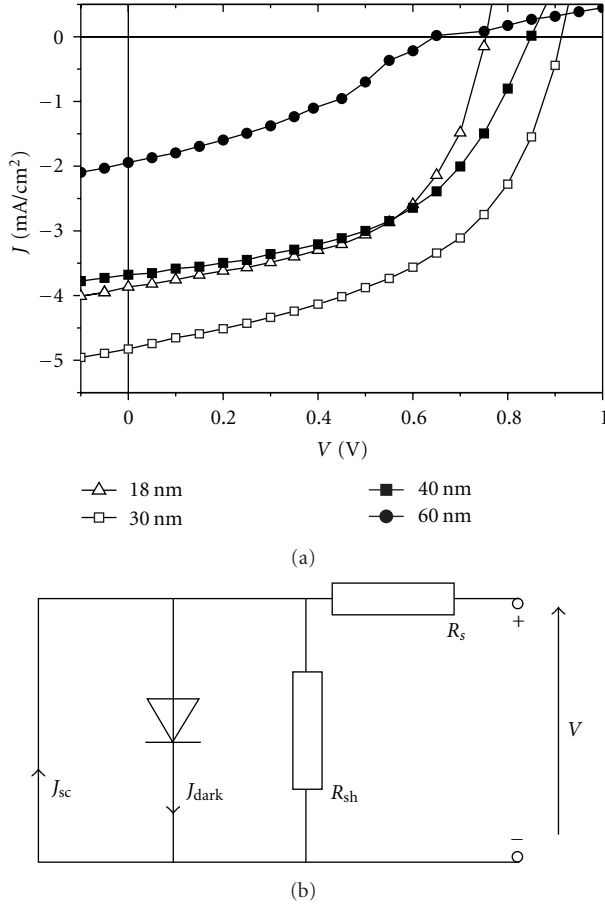


FIGURE 4: (J - V) curves under AM 1.5 illumination of 100 mWcm^{-2} for the FTO/PEDOT : PSS/F8T2/ C_{60} /Al devices with different thickness of the F8T2 layer. An equivalent circuit simplified for a photovoltaic device, where R_s and R_{sh} are the series and shunt resistance, respectively.

Wagner [22]. Generally, the loss mechanisms in photovoltaic devices are divided in series resistance (R_s), which is related with the loss by charge carrier trapping or recombination of free charges, and shunt resistance (in parallel with the current source) (R_{sh}), which is related with leakage phenomena. R_s increases with the active layer thickness due to the increasing of the probability of a charge carrier to be trapped. In our devices, the series resistance increased with the F8T2 thickness for 30 nm the R_s was 77Ω , for 40 nm the R_s was 198Ω , and for 60 nm the R_s was 445Ω . In the case of 18 nm the R_s was 150Ω . This value did not follow the general behavior of resistance versus polymer thickness suggesting that the film formation indeed modifies the charge transport.

The electrical properties of these bilayer devices were also investigated by measuring the current versus voltage characteristics in dark. The study of forward current of bi-layer diodes is not so straight forward to do. F8T2 and C_{60} have different electron affinities values in order to promote the exciton dissociation. The interface barrier of F8T2/ C_{60} is high enough to prevent the passage of charges through it, forming high charge density in each layer with a maximal recombination zone near the interface, resulting in a monop-

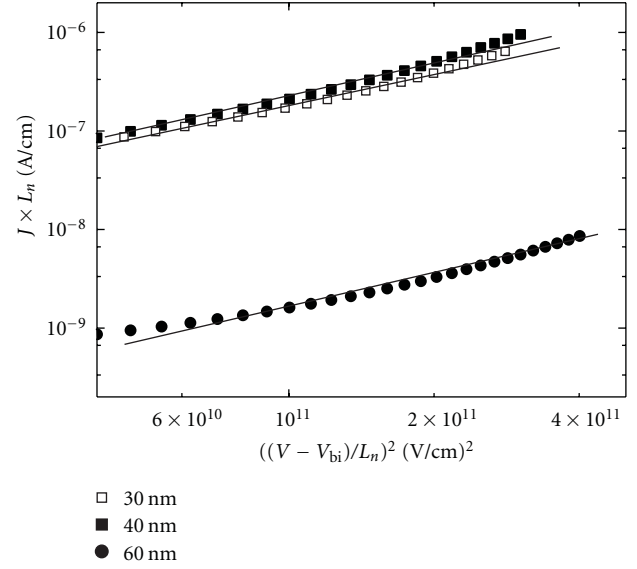


FIGURE 5: A log-log plot of the current density in dark times the C_{60} thickness by the square of the voltage across the whole device divided by the C_{60} thickness for three different values of the F8T2 thickness. All the linear fittings have angular coefficients equal to one, which characterize the Mott-Gurney law.

olar current density of hole inside the polymer layer and electrons inside the molecule layer [23]. Also, as the devices were fabricated with two different work functions electrodes ($\Phi_{\text{PEDOT}} \approx 5.2 \text{ eV}$ and $\Phi_{\text{Al}} \approx 4.2 \text{ eV}$), a built-in potential (V_{bi}) is established in the organic layers at zero bias. Before attempting to model current versus field data [24], this inherent potential V_{bi} must be subtracted from the applied voltage. Based on earlier reports in literature, it was found that the built-in potential is equal to the open-circuit photovoltage (V_{oc}) of the device at low temperature [25]. In this work, the V_{oc} for each F8T2 thickness from Figure 2(b) is considered as the built-in potential value. Considering that, plotting the data from the current versus voltage curve in dark as a log-log plot of the $J \times L(C_{60})$ versus $((V - V_{bi})/L(C_{60}))^2$ (Figure 5), it is possible to notice that all the linear fittings have angular coefficient equal to one, which characterize the Mott-Gurney law of space charge limited current (SCLC) described by the expression [26]:

$$J = \frac{9}{8} \epsilon_0 \epsilon_r \mu \frac{(V - V_{bi})^2}{L^3}, \quad (1)$$

where $\epsilon_0 \epsilon_r$ is the permittivity of the polymer, μ the electron mobility, and L the thickness of the C_{60} layer. The space charge limited current flowing in the device is induced by effective thickness-dependent mobilities of the charges in the respective layer of the device, spatial charge of holes in the polymer, and electrons in the molecule layers. The linear fittings of SCLC scaling plots for the fixed C_{60} thickness show that in each material layer we have a simple Mott-Gurney law. Thus, the charge transport in these devices is a property of the interface polymer/ C_{60} . From the different curves for different polymer thickness, it follows that the effective mobility of holes and electrons are dependent on the ratio

between the polymer and C₆₀ layers' thickness. Despite the fact that a power conversion efficiency of 2.1% was achieved for one combination of thickness in these bi-layer devices, the analysis of the electrical properties in dark indicates that the mobility of charges in these devices still limits the efficiency.

4. Conclusion

We have investigated the effect of altering the F8T2 film thickness on the photovoltaic performance of devices based on the bilayer heterojunction with C₆₀ molecules. It has been demonstrated that a power conversion efficiency of 2.1% can be achieved for F8T2 films with thickness equal to 30 nm and submitted to annealing at 100°C. From experimental and theoretical analyses, we have results that for such kind of systems the forward current is limited by spatial charge of holes in the polymer layer and electrons in the molecule layer. The series resistance calculated for an equivalent circuit of solar cells applied to our diodes plays an important part, depending not only on the layer thickness but also film morphology.

References

- [1] I. Olle, Z. Fengling, and M. R. Andersson, "Alternating polyfluorenes collect solar light in polymer photovoltaics," *Accounts of Chemical Research*, vol. 42, no. 11, pp. 1731–1739, 2009.
- [2] L. Akcelrud, "Electroluminescent polymers," *Progress in Polymer Science*, vol. 28, no. 6, pp. 875–962, 2003.
- [3] B. Zhao, D. Liu, L. Peng et al., "Effect of oxadiazole side chains based on alternating fluorene-thiophene copolymers for photovoltaic cells," *European Polymer Journal*, vol. 45, no. 7, pp. 2079–2086, 2009.
- [4] G. L. Schulz, X. Chen, and S. Holdcroft, "High band gap poly(9,9-dihexylfluorene-alt-bithiophene) blended with [6,6]-phenyl C₆₁ butyric acid methyl ester for use in efficient photovoltaic devices," *Applied Physics Letters*, vol. 94, no. 2, Article ID 023302, 2009.
- [5] J. H. Huang, C. Y. Yang, Z. Y. Ho et al., "Annealing effect of polymer bulk heterojunction solar cells based on polyfluorene and fullerene blend," *Organic Electronics: Physics, Materials, Applications*, vol. 10, no. 1, pp. 27–33, 2009.
- [6] J. H. Huang, K. C. Li, D. Kekuda et al., "Efficient bilayer polymer solar cells possessing planar mixed-heterojunction structures," *Journal of Materials Chemistry*, vol. 20, no. 16, pp. 3295–3300, 2010.
- [7] D. Kekuda, J. H. Huang, K. C. Ho, and C. W. Chu, "Modulation of donor-acceptor interface through thermal treatment for efficient bilayer organic solar cells," *Journal of Physical Chemistry C*, vol. 114, no. 6, pp. 2764–2768, 2010.
- [8] A. G. Macedo, C. F. N. Marchiori, I. R. Grova, L. Akcelrud, M. Koehler, and L. S. Roman, "Hole mobility effect in the efficiency of bilayer heterojunction polymer/C₆₀ photovoltaic cells," *Applied Physics Letters*, vol. 98, p. 253501, 2011.
- [9] C. D. Canestraro, M. C. Schnitzler, A. J. G. Zarbin, M. G. E. da Luz, and L. S. Roman, "Carbon nanotubes based nanocomposites for photocurrent improvement," *Applied Surface Science*, vol. 252, no. 15, pp. 5575–5578, 2006.
- [10] R. Valaski, C. D. Canestraro, L. Micaroni, R. M. Q. Mello, and L. S. Roman, "Organic photovoltaic devices based on polythiophene films electrodeposited on FTO substrates," *Solar Energy Materials and Solar Cells*, vol. 91, no. 8, pp. 684–688, 2007.
- [11] A. C. Arias, L. S. Roman, T. Kugler, R. Toniolo, M. S. Meruvia, and I. A. Hümmelgen, "Use of tin oxide thin films as a transparent electrode in PPV based light-emitting diodes," *Thin Solid Films*, vol. 371, no. 1, pp. 201–206, 2000.
- [12] H. Sirringhaus, M. Bird, T. Richards, and N. Zhao, "Charge transport physics of conjugated polymer field-effect transistors," *Advanced Materials*, vol. 22, no. 34, pp. 3893–3898, 2010.
- [13] J. C. Hummelen, B. W. Knight, F. Lepeq, F. Wudl, J. Yao, and C. L. Wilkins, "Preparation and characterization of fulleroid and methanofullerene derivatives," *Journal of Organic Chemistry*, vol. 60, no. 3, pp. 532–538, 1995.
- [14] S. A. Backer, K. Sivula, D. F. Kavulak, and J. M. J. Fréchet, "High efficiency organic photovoltaics incorporating a new family of soluble fullerene derivatives," *Chemistry of Materials*, vol. 19, no. 12, pp. 2927–2929, 2007.
- [15] G. Zhao, Y. He, Z. Xu et al., "Effect of carbon chain length in the substituent of PCBM-like molecules on their photovoltaic properties," *Advanced Functional Materials*, vol. 20, no. 9, pp. 1480–1487, 2010.
- [16] L. S. Roman, R. Valaski, C. D. Canestraro et al., "Optical band-edge absorption of oxide compound SnO₂," *Applied Surface Science*, vol. 252, no. 15, pp. 5361–5364, 2006.
- [17] P. R. F. Barnes, A. Y. Anderson, S. E. Koops, J. R. Durrant, and B. C. O'Regan, "Electron injection efficiency and diffusion length in dye-sensitized solar cells derived from incident photon conversion efficiency measurements," *Journal of Physical Chemistry C*, vol. 113, no. 3, pp. 1126–1136, 2009.
- [18] J. H. Huang, C. P. Lee, Z. Y. Ho, D. Kekuda, C. W. Chu, and K. C. Ho, "Enhanced spectral response in polymer bulk heterojunction solar cells by using active materials with complementary spectra," *Solar Energy Materials and Solar Cells*, vol. 94, no. 1, pp. 22–28, 2010.
- [19] M. Koehler, L. S. Roman, O. Inganäs, and M. G. E. Da Luz, "Modeling bilayer polymer/fullerene photovoltaic devices," *Journal of Applied Physics*, vol. 96, no. 1, pp. 40–43, 2004.
- [20] L. S. Roman, W. Mammo, L. A. A. Pettersson, M. R. Andersson, and O. Inganäs, "High quantum efficiency polythiophene/C₆₀ photodiodes," *Advanced Materials*, vol. 10, no. 10, pp. 774–777, 1998.
- [21] L. A. A. Pettersson, L. S. Roman, and O. Inganäs, "Modeling photocurrent action spectra of photovoltaic devices based on organic thin films," *Journal of Applied Physics*, vol. 86, no. 1, pp. 487–496, 1999.
- [22] G. Kunz and A. Wagner, "Internal series resistance determined of only one I-V curve under illumination," in *Proceedings of the 19th European Photovoltaic Solar Energy Conference*, p. 5BV.2.70, 2004.
- [23] M. Koehler, L. S. Roman, O. Inganäs, and M. G. E. Da Luz, "Space-charge-limited bipolar currents in polymer/C₆₀ diodes," *Journal of Applied Physics*, vol. 92, no. 9, pp. 5575–5577, 2002.
- [24] G. G. Malliaras, J. R. Salem, P. J. Brock, and C. Scott, "Electrical characteristics and efficiency of single-layer organic light-emitting diodes," *Physical Review B*, vol. 58, no. 20, pp. R13411–R13414, 1998.
- [25] G. G. Malliaras, J. R. Salem, P. J. Brock, and J. C. Scott, "Photovoltaic measurement of the built-in potential in organic light emitting diodes and photodiodes," *Journal of Applied Physics*, vol. 84, no. 3, pp. 1583–1587, 1998.
- [26] P. N. Murgatroyd, "Theory of space-charge-limited current enhanced by Frenkel effect," *Journal of Physics D*, vol. 3, no. 2, article 308, pp. 151–156, 1970.

Research Article

Young's Modulus of Single-Crystal Fullerene C₇₀ Nanotubes

Tokushi Kizuka,¹ Kun'ichi Miyazawa,² and Takayuki Tokumine¹

¹Institute of Materials Science, Graduate School of Pure and Applied Sciences, University of Tsukuba, Tsukuba 305-8753, Japan

²Fullerene Engineering Group, Materials Processing Unit, National Institute for Materials Science, Namiki, Tsukuba 305-0044, Japan

Correspondence should be addressed to Tokushi Kizuka, kizuka@ims.tsukuba.ac.jp

Received 1 June 2011; Accepted 22 July 2011

Academic Editor: Ilia A. Solov'yov

Copyright © 2012 Tokushi Kizuka et al. This is an open access article distributed under the Creative Commons Attribution License, which permits unrestricted use, distribution, and reproduction in any medium, provided the original work is properly cited.

We performed bending tests on single-crystal nanotubes composed of fullerene C₇₀ molecules by *in situ* transmission electron microscopy with measurements of loading forces by an optical deflection method. The nanotubes with the outer diameters of 270–470 nm were bent using simple-beam and cantilever-beam loading by the piezomanipulation of silicon nanotips. Young's modulus of the nanotubes increased from 61 GPa to 110 GPa as the outer diameter decreased from 470 nm to 270 nm. Young's modulus was estimated to be 66% of that of single-crystal C₆₀ nanotubes of the same outer diameter.

1. Introduction

There have been many investigations of crystal morphologies and structures of fullerene C₆₀ molecules since the first report on the crystallization of fullerene C₆₀ molecules. C₆₀ crystals have been shown in the forms of plates, films, and rods [1–13]. In particular, single-crystal fullerene nanowhiskers (NWs) with high length-to-diameter aspect ratios have been synthesized by a liquid–liquid interfacial precipitation (LLIP) method [14, 15]. In addition, tubular fullerene NWs, that is, single-crystal fullerene nanotubes (NTs) have been synthesized by the same method [16]. The mechanical properties of NWs and NTs have been investigated for application to structural materials and functional devices. Buckling tests of C₆₀ NWs and NTs have been performed by *in situ* transmission electron microscopy (TEM), and their Young's moduli were estimated to be 53–69 GPa and 62–107 GPa, respectively [17–19]. Fullerene NWs and NTs can be synthesized using another well-known fullerene molecule, that is, C₇₀ [15, 20]. The mechanical nature of fullerene NWs and NTs can be controlled by selecting their constituent molecules, as demonstrated in fullerene films [21, 22]. In this study, we performed bending tests on C₇₀ NTs by *in situ* TEM.

2. Experimental

We synthesized C₇₀ NTs by the LLIP method using a saturated solution of C₇₀ molecules in pyridine and 2-propanol [16]. The solution, including precipitated C₇₀ NTs, was added dropwise to the edge of a gold plate. The plate was mounted on a specimen holder of the transmission electron microscope equipped with a piezomanipulation system at the University of Tsukuba [23–26]. A silicon microcantilever with a nanometer-sized tip used for contact-type atomic force microscopy (AFM) was fixed onto a cantilever holder. Both the specimen and the cantilever holders were inserted into the microscope. The cantilever tip was brought into contact with individual NTs fixed on the plate edges by piezomanipulation inside the microscope. The tip was then pressed on the NTs for bending with simple-beam- and cantilever-beam-type loading. The cantilever tip was then pulled back to release the force. A series of these manipulations were performed several times at room temperature in a vacuum of 1×10^{-5} Pa using the same NT. The deformation process was observed *in situ* using a television and video capture system with a time resolution of 17 ms. At the same time, the force applied to the NTs was measured by optical detection of the cantilever deflection used in AFM.

The spring constant of the cantilever was measured to be 4.7 N/m.

3. Results

Figure 1 shows a time-sequence series of the bright-field images of the bending process of a C_{70} NT protruding from an edge of the gold plate. The dark triangular region in the upper part of each frame of Figure 1 is the cantilever tip. The brighter region around the NT is the vacuum. The outer and inner diameters of the NT in Figure 1 are 270 nm and 100 nm, respectively. The length of the deformed part is 2.5 μm . The crystal structure of the NT was tetragonal. This crystal structure has been observed in dried C_{70} NWs, C_{60} NWs, and NTs synthesized by LLIP methods [18–20]. Polymerized C_{70} crystals under hydrostatic compression have an orthorhombic structure with similar lattice constants a and c , which is comparable to the tetragonal structure [27]. The longer growth axis of the NT is aligned parallel to the [110] direction. The left side of the NT was fixed on the gold plate, as shown in Figure 1. In this bending test, the cantilever tip was initially placed in contact with the NT (Figure 1(a)). Then, force was exerted on the NT in the direction indicated by the arrow in Figure 1(a) and was bent (Figure 1(b)). Thus, bending of the NT was performed using cantilever-beam-type loading. Subsequently, the tip was released, and the NT recovered its initial straight shape (Figure 1(c)). This observation shows that the bending is an elastic deformation. This bending and recovery cycle was repeated several times using the same NT. Figure 2 shows the relationship between the force and the flexure during the bending process depicted in Figure 1. The points indicated by arrowheads a–c in Figure 2 correspond to the TEM images in Figures 1(a)–1(c). The maximum flexure and loading at the free end of the NT were 467 nm and 431 nN, respectively. A hysteresis is observed in Figure 2 during the pressing and pulling of the cantilever tip. This is attributed to the bonding of the cantilever tip with the NT surface [28]. Sawtooth-like variations are observed in both the pressing and pulling processes. The decrease in force during the pressing process and the increase in force during the pulling process are caused by the rotation of the cantilever tip due to slip of the contact region between the cantilever tip and the NT surface [28]. The increase in force during the pulling process arises from the recovery of deflection of the AFM cantilever beam by increase in the recovery shift of the NT due to slip. The other changes in the exerted force, that is, the increase during the pressing process and the decrease during the pulling process, are not significantly influenced by slip events. On the basis of the relationships among force, flexure, and Young's modulus in cantilever-beam loading, we estimated that Young's modulus of the NTs is 68–110 GPa from the slope of the force curve in these regions. We performed a bending test with the same type loading for another NT with an outer diameter of 470 nm and an inner diameter of 230 nm. Its Young's modulus was estimated to be 61 ± 5 GPa.

Figure 3 shows a time-sequence series of the bright-field images of the bending process of a C_{70} NT, both ends of

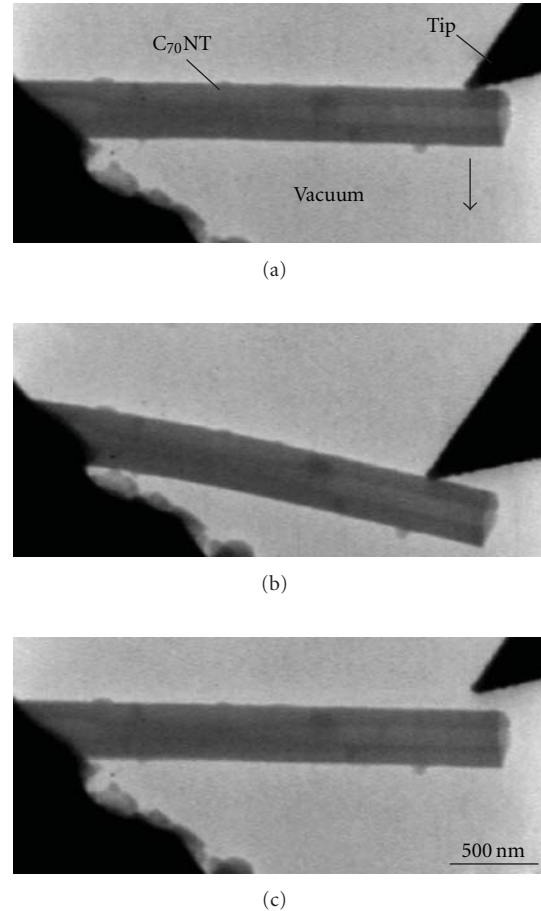


FIGURE 1: A time-sequence series image and the separation like galley is forbidden. Time-sequence series of bright-field images of cantilever-beam-type loading bending of single-crystal C_{70} nanotube with outer diameter of 270 nm and inner diameter of 100 nm. One end of the nanotube is fixed on a gold plate. The arrow indicates the direction of loading imparted by the tip of AFM cantilever. This bending test was performed in the vacuum.

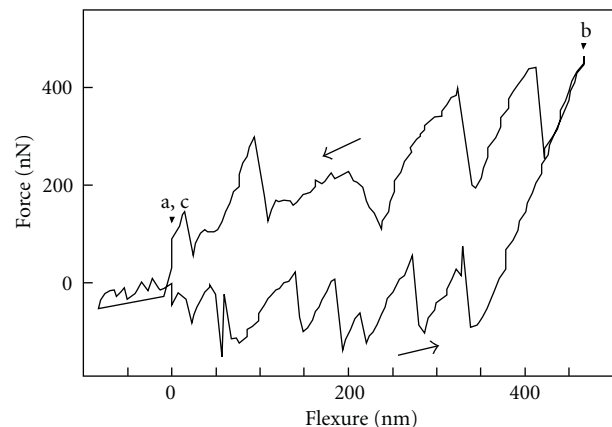


FIGURE 2: Force-flexure curve of C_{70} nanotube during bending shown in Figure 1. Points a–c correspond to the states shown in Figures 1(a)–1(c). The arrows indicate the time path of recording.

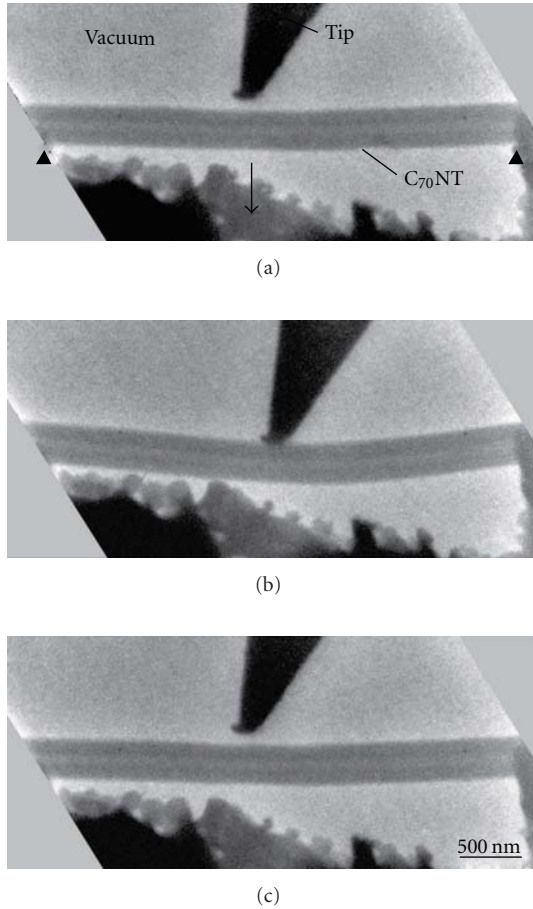


FIGURE 3: Time-sequence series of bright-field images of loading of simple-beam-type bending of single-crystal C_{70} nanotube with outer diameter of 340 nm and inner diameter of 80 nm. The nanotube is supported on a gold plate with two fulcra indicated by the triangles. The arrow indicates the loading direction by the tip of the AFM cantilever. This bending test was performed in the vacuum.

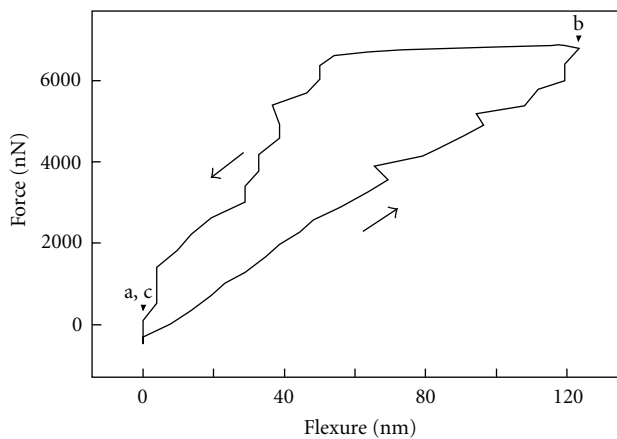


FIGURE 4: Force-flexure curve of C_{70} nanotube during bending shown in Figure 3. Points a–c correspond to the states shown in Figures 3(a)–3(c), respectively. The arrows indicate the time path of recording.

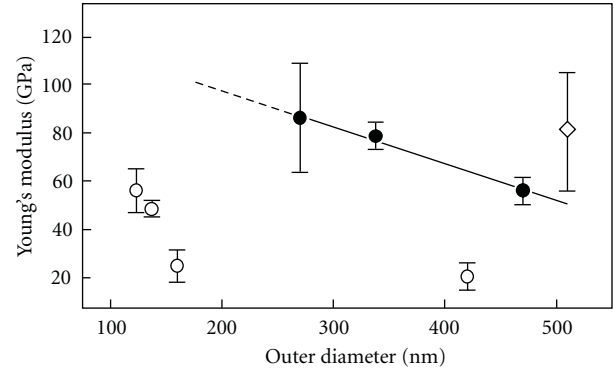


FIGURE 5: Young's modulus of single-crystal C_{70} nanotubes plotted against outer diameter. The values observed in the present study are indicated by the filled circles. The solid line indicates a linear approximation. For reference, Young's moduli of single-crystal C_{60} nanotubes and nanowhiskers are represented with rhombus and open circles, respectively [18, 19, 29].

which were fixed on the gold plate. The outer and inner diameters of the NT are 340 nm and 80 nm, respectively. The length of the region of deformation was $3.5 \mu\text{m}$. The loading was performed at the center of the deformation region by the cantilever tip. Thus, this loading was simple-beam-type loading. Figure 4 shows the relationship between the force and the flexure during the bending process presented in Figure 2. The maximum flexure and loading at the free end were 123 nm and $6.8 \mu\text{N}$, respectively. Similar to the cantilever-beam-type bending in Figure 1, a hysteresis is observed. The pressing process from state (a) to (b) in Figure 4 is approximated by one slope. In contrast, the pulling process from state (b) to (c) in Figure 4 is composed of two slopes. The lower slope from state (b) in the pulling process is attributed to the friction between the cantilever tip and the NT surface. This is because the rotation of the cantilever tip, that is, the change in cantilever-beam deflection, is suppressed by the friction [28]. From the slope during the pressing process from state (a) to (b) in Figure 4, we estimated Young's modulus of the NTs to be $82 \pm 5 \text{ GPa}$ on the basis of the relationships among force, flexure, and Young's modulus in simple-beam loading.

In Figure 5, we plotted Young's modulus of these C_{70} NTs against their outer diameters. Young's modulus increases as the outer diameter decreases. The relationship between Young's modulus E (GPa) of C_{70} NTs and the outer diameters d (nm) is approximated by a straight line, $E = -0.143d + 129$, as shown in Figure 5. As the thickness of the NTs used in this study is 85–130 nm, the tubular structure does not occur when the minimum outer diameter decreases less than 170–260 nm. From this minimum diameter, the maximum Young's modulus of C_{70} NTs is estimated to be 92–105 GPa. Kizuka et al. reported that Young's modulus of a C_{60} NT with an outer diameter of 510 nm is 84.5 GPa [18]. From the linear approximation in Figure 5, Young's modulus of a C_{70} NT with the same outer diameter, that is, 510 nm, is calculated to be 56 GPa. Thus, Young's modulus of the C_{70} NT is 66% of that of a C_{60} NT of the same outer diameter.

4. Discussion

4.1. Young's Modulus of C_{70} NTs and Films. Young's moduli of C_{70} NTs estimated in this study are 7–28 times larger than those of crystalline C_{70} films (4–9 GPa) [21, 22]. The crystal lattice of the C_{70} NTs studied here is tetragonal, whereas crystal structure of C_{70} crystalline films is the face-centered-cubic structure [21, 22]. The averaged center-to-center distance between adjoining C_{70} molecules in the NTs along the growth direction is 3% smaller than that of C_{70} NTs with a face-centered-cubic structure [15]. According to Miyazawa et al., this difference can be attributed to the polymerization of the molecules [14]. Thus, it is deduced that the increase in Young's modulus observed in this study originates from the effect of the polymerization of the constituent C_{70} molecules, as previously discussed for the bending tests of C_{60} NTs [18].

4.2. Young's Modulus of C_{70} NTs and C_{60} NTs. The estimated Young's moduli of C_{70} NTs are larger than those of the crystalline C_{70} films, whereas the modulus obtained for the C_{70} NT with an outer diameter of 510 nm is 66% of that of a C_{60} NT with the same diameter. Kolomenskii et al. and Murugavel et al. reported a similar quantitative relationship of Young's moduli in crystalline C_{70} and C_{60} films [21, 22]. They attribute this relationship to the difference in molecular densities of crystalline C_{70} and C_{60} films.

4.3. Dependency of Young's Modulus on the Outer Diameter. As shown in Figure 5, Young's modulus increases as the outer diameter decreases. Saito et al. observed a similar relationship between Young's modulus and the outer diameter of C_{60} NWs [19]. They discussed the relationship on the basis of a core-shell structure model of C_{60} NWs. Ringor and Miyazawa investigated the incubation process of C_{60} NWs in solution and revealed that C_{60} NTs were formed owing to the elution of the interior regions [30]. Kato and Miyazawa pointed out from the cross-sectional TEM that the density of pores in the interior region of C_{60} NWs is higher than that in the region near the surfaces [31]. Their result also supports the core-shell structure of NWs. The dependency of the Young's modulus on the outer diameter, as shown in Figure 5, infers that the core component remained in the C_{70} NTs and the larger Young's modulus of thinner NTs is attributed to a smaller amount of the core component, which leads to a lower density of the NT.

5. Conclusion

We performed bending tests on individual C_{70} NTs by *in situ* TEM. From the measurements of the force-flexure relationships of C_{70} NTs, Young's modulus was estimated to be 61–110 GPa. Young's modulus increased as the outer diameter decreased. From this relationship, the Young's modulus of a C_{70} NT was estimated to be 66% of that of a C_{60} NT of the same outer diameter, that is, 510 nm. The maximum Young's modulus of C_{70} NTs was estimated to be 92–105 GPa from the limit of the thickness of the tubular structure.

Acknowledgment

This study was partly supported by Grants-in-Aid from the Ministry of Education, Culture, Sport, Science, and Technology, Japan (nos. 22310065 and 23651127).

References

- [1] W. Krätschmer, L. D. Lamb, K. Fostiropoulos, and D. R. Huffman, "Solid C_{60} : a new form of carbon," *Nature*, vol. 347, no. 6291, pp. 354–358, 1990.
- [2] W. I. F. David, R. M. Ibberson, J. C. Matthewman et al., "Crystal structure and bonding of ordered C_{60} ," *Nature*, vol. 353, no. 6340, pp. 147–149, 1991.
- [3] S. J. Duclos, K. Brister, R. C. Haddon, A. R. Kortan, and F. A. Thiel, "Effects of pressure and stress on C_{60} fullerite to 20 GPa," *Nature*, vol. 351, no. 6325, pp. 380–382, 1991.
- [4] P. A. Heiney, J. E. Fischer, A. R. McGhie et al., "Orientational ordering transition in solid C_{60} ," *Physical Review Letters*, vol. 66, no. 22, pp. 2911–2914, 1991.
- [5] R. L. Meng, D. Ramirez, X. Jiang et al., "Growth of large, defect-free pure C_{60} single crystals," *Applied Physics Letters*, vol. 59, no. 26, pp. 3402–3403, 1991.
- [6] W. Krakow, N. M. Rivera, R. A. Roy, R. S. Ruoff, and J. J. Cuomo, "Epitaxial growth of C_{60} thin films on mica," *Journal of Materials Research*, vol. 7, no. 4, pp. 784–787, 1992.
- [7] X. D. Shi, A. R. Kortan, J. M. Williams, A. M. Kini, B. M. Savall, and P. M. Chaikin, "Sound velocity and attenuation in single-crystal C_{60} ," *Physical Review Letters*, vol. 68, no. 6, pp. 827–830, 1992.
- [8] Y. Yosida, "Scanning electron microscope images of C_{60} whiskers," *Japanese Journal of Applied Physics*, vol. 31, no. 4B, pp. L505–L507, 1992.
- [9] M. Haluška, H. Kuzmany, M. Vybornov, P. Rogl, and P. Fejdi, "A double-temperature-gradient technique for the growth of single-crystal fullerenes from the vapor phase," *Applied Physics A*, vol. 56, no. 3, pp. 161–167, 1993.
- [10] J. Z. Liu, J. W. Dykes, M. D. Lan, P. Klavins, R. N. Shelton, and M. M. Olmstead, "Vapor transport growth of C_{60} crystals," *Applied Physics Letters*, vol. 62, no. 5, pp. 531–532, 1993.
- [11] J. L. D. Boer, S. V. Smaalen, V. Petricek, M. Dusek, M. A. Verheijen, and G. Meijer, "Hexagonal close-packed C_{60} ," *Chemical Physics Letters*, vol. 219, no. 5–6, pp. 469–472, 1994.
- [12] F. Michaud, M. Barrio, S. Toscani et al., "Solid-state studies on single and decagonal crystals of C_{60} grown from 1,2-dichloroethane," *Physical Review B*, vol. 57, no. 17, pp. 10351–10358, 1998.
- [13] S. Toscani, H. Allouchi, J. L. Tamarit et al., "Decagonal C_{60} crystals grown from n-hexane solutions: solid-state and aging studies," *Chemical Physics Letters*, vol. 330, no. 5–6, pp. 491–496, 2000.
- [14] K. Miyazawa, Y. Kuwasaki, A. Obayashi, and M. Kuwabara, " C_{60} nanowhiskers formed by the liquid-liquid interfacial precipitation method," *Journal of Materials Research*, vol. 17, no. 1, pp. 83–88, 2002.
- [15] K. Miyazawa, K. Hamamoto, S. Nagata, and T. Suga, "Structural investigation of the C_{60}/C_{70} whiskers fabricated by forming liquid-liquid interfaces of toluene with dissolved C_{60}/C_{70} and isopropyl alcohol," *Journal of Materials Research*, vol. 18, no. 5, pp. 1096–1103, 2003.

- [16] J. Minato and K. Miyazawa, "Solvated structure of C_{60} nanowhiskers," *Carbon*, vol. 43, no. 14, pp. 2837–2841, 2005.
- [17] K. Asaka, R. Kato, K. Miyazawa, and T. Kizuka, "Buckling of C_{60} whiskers," *Applied Physics Letters*, vol. 89, no. 7, Article ID 071912, 3 pages, 2006.
- [18] T. Kizuka, K. Saito, and K. Miyazawa, "Young's modulus of crystalline C_{60} nanotubes studied by in situ transmission electron microscopy," *Diamond and Related Materials*, vol. 17, no. 6, pp. 972–974, 2008.
- [19] K. Saito, K. Miyazawa, and T. Kizuka, "Bending process and Young's modulus of fullerene C_{60} nanowhiskers," *Japanese Journal of Applied Physics*, vol. 48, no. 1, Article ID 010217, 3 pages, 2009.
- [20] K. Miyazawa, " C_{70} nanowhiskers fabricated by forming liquid/liquid interfaces in the systems of toluene solution of C_{70} and isopropyl/alcohol," *Journal of the American Ceramic Society*, vol. 85, no. 5, pp. 1297–1299, 2002.
- [21] A. A. Kolomenskii, M. Szabadi, and P. Hess, "Laser diagnostics of C_{60} and C_{70} films by broadband surface acoustic wave spectroscopy," *Applied Surface Science*, vol. 86, no. 1–4, pp. 591–596, 1995.
- [22] P. Murugavel, C. Narayana, A. Govindaraj, A. K. Sood, and C. N. R. Rao, "Brillouin scattering from C_{70} and C_{60} films: a comparative study of elastic properties," *Chemical Physics Letters*, vol. 331, no. 2–4, pp. 149–153, 2000.
- [23] T. Kizuka, K. Yamada, S. Deguchi, M. Naruse, and N. Tanaka, "Cross-sectional time-resolved high-resolution transmission electron microscopy of atomic-scale contact and noncontact-type scanings on gold surfaces," *Physical Review B*, vol. 55, no. 12, pp. R7398–R7401, 1997.
- [24] T. Kizuka, "Atomic process of point contact in gold studied by time-resolved high-resolution transmission electron microscopy," *Physical Review Letters*, vol. 81, no. 20, pp. 4448–4451, 1998.
- [25] T. Kizuka, "Direct atomistic observation of deformation in multiwalled carbon nanotubes," *Physical Review B*, vol. 59, no. 7, pp. 4646–4649, 1999.
- [26] T. Kizuka, "Atomic configuration and mechanical and electrical properties of stable gold wires of single-atom width," *Physical Review B*, vol. 77, no. 15, Article ID 155401, 11 pages, 2008.
- [27] A. V. Soldatov, G. Roth, A. Dzyabchenko et al., "Topochemical polymerization of C_{70} controlled by monomer crystal packing," *Science*, vol. 293, no. 5530, pp. 680–683, 2001.
- [28] S. Fujisawa and T. Kizuka, "Effect of lateral displacement of atomic force microscope tip caused by contact scanning studied by in situ transmission electron microscopy," *Japanese Journal of Applied Physics*, vol. 42, no. 3, pp. L1182–L1184, 2003.
- [29] K. Asaka and T. Kizuka, "Atomistic dynamics of deformation, fracture, and joining of individual single-walled carbon nanotubes," *Physical Review B*, vol. 72, no. 11, Article ID 115431, 5 pages, 2005.
- [30] C. L. Ringor and K. Miyazawa, "Fabrication of solution grown C_{60} fullerene nanotubes with tunable diameter," *Journal of Nanoscience and Nanotechnology*, vol. 9, no. 11, pp. 6560–6564, 2009.
- [31] R. Kato and K. Miyazawa, "Cross-sectional structural analysis of C_{60} nanowhiskers by transmission electron microscopy," *Diamond and Related Materials*, vol. 20, no. 3, pp. 299–303, 2011.